

# Important Notice

This copy may be used only for the purposes of research and private study, and any use of the copy for a purpose other than research or private study may require the authorization of the copyright owner of the work in question. Responsibility regarding questions of copyright that may arise in the use of this copy is assumed by the recipient.

UNIVERSITY OF CALGARY

Development and Characterization of a Geostatic Model for Monitoring  
Shallow CO<sub>2</sub> Injection

by

Jessica Maria Dongas

A THESIS

SUBMITTED TO THE FACULTY OF GRADUATE STUDIES  
IN PARTIAL FULFILMENT OF THE REQUIREMENTS FOR THE  
DEGREE OF MASTER OF SCIENCE

GRADUATE PROGRAM IN GEOLOGY AND GEOPHYSICS

CALGARY, ALBERTA

JANUARY, 2016

© Jessica Maria Dongas 2016

## **Abstract**

A 25 sq. km static geomodel was constructed for shallow injection into the 7 m thick Basal Belly River Sandstone at 300 m depth in Newell County, Alberta. Effective porosity and intrinsic permeability were calibrated to six core laboratory analyses. The regression shoreline sandstone has effective porosity of 11% and intrinsic permeability of 0.57 mD. Dynamic simulation was completed on the P10-50-90 static cases for multiple injection scenarios, totalling approximately 3250 t/CO<sub>2</sub> over a five-year period. The evolution of the CO<sub>2</sub> plume was observed at one-year during injection and five-years during injection, as well as the one-year and ten-year mark for the post-injection period. The final ten-year post-injection result simulated a laterally extensive plume, expanding to 350 m in diameter and 20 m of vertical migration into the caprock interval. The target interval proves to be an ideal reservoir, and the seal interval predicts containment over a ten-year post-injection period.

## **Acknowledgements**

I would like to express my sincerest gratitude to my supervisor Dr. Don C. Lawton for his leadership, guidance, and engaging support throughout the duration of completing my degree. His wisdom, knowledge, and positivity have made this opportunity an unforgettable one.

Thank you to CREWES staff and students, my experience has been enriched with the support and community the research group brings to the University of Calgary. I would like to thank Laura Baird, for her unconditional support and eclectic conversations that made the days fly by. A special thanks to Roy Lindseth for his time and efforts in editing this thesis, but most of all – evoking critical discussion topics which have aided in my understanding of seismic well ties.

Special thanks to CREWES sponsors, CMC Research Institutes, Inc., and the Natural Science and Engineering Research Council of Canada for providing the financial support of my academic pursuits. Thanks to Cenovus Energy for providing land access and datasets for the study area. Thanks to IHS Energy and Schlumberger Inc. for providing the licenses of software used in this thesis.

Special thanks to Lee Swager, Si-Yong Lee, and Wade Zaluski - this extreme-team trio has contributed throughout the duration of the project by providing extensive expertise, conceptual discussions, and a breadth of knowledge in petrophysics, dynamic modeling, and static geomodeling, respectively. Thank you to Wade Zaluski for providing an invaluable mentorship throughout the duration of my degree. His patience, knowledge, and continuous support provided a positive learning experience. I have taken away so much from working with Wade, the organizational skills, professionalism, quality assurance and control techniques, as well as time management for maintaining a life balance during my graduate career.

Finally, I would like to thank my family for their unconditional support in every decision I have made in order to achieve my dreams – even if it means being 3000 km away.

## **Dedication**

*To my beloved family and friends, without whom none of my success would be possible.*

## Table of Contents

Abstract .....	ii
Acknowledgements .....	iii
Dedication .....	iv
Table of Contents .....	v
List of Tables .....	vii
List of Figures and Illustrations .....	ix
List of Symbols, Abbreviations, and Nomenclature .....	xv
CHAPTER ONE: CARBON MANAGEMENT .....	1
1.1 CO <sub>2</sub> Capture and storage: A step forward .....	1
1.2 CO <sub>2</sub> Properties .....	3
1.3 Trapping mechanisms .....	5
1.3.1 Stratigraphic trapping .....	5
1.3.2 Residual trapping .....	5
1.3.3 Solubility trapping .....	6
1.3.4 Mineral trapping .....	6
1.4 Reservoirs for sequestration.....	7
1.5 Monitoring, measurement, and verification plans: An overview .....	7
1.6 From bench to field: What is the Field Research Station? .....	9
1.7 Thesis objectives .....	12
1.8 Thesis contributions .....	13
1.9 Study area .....	15
1.10 Data and software used .....	17
1.11 Thesis structure .....	20
CHAPTER TWO: GEOLOGICAL BACKGROUND .....	21
2.1 Summary of target and seal zones A and B .....	22
2.1.1 Medicine Hat Member .....	22
2.1.2 First White Specks Member .....	24
2.1.3 Basal Belly River Sandstone Unit .....	25
2.1.4 Foremost Formation .....	27
2.2 Hydrogeological background of Newell County, Alberta .....	29
CHAPTER THREE: DEVELOPMENT OF THE FRS MODEL.....	31
3.1 Baseline characterization – geophysical .....	31
3.1.1 Geophysical interpretation.....	31
3.1.2 Seismic well tie process.....	38
3.1.3 Depth conversion via velocity modeling .....	48
3.1.4 Seismic attributes.....	51
3.2 Baseline characterization – geological .....	59
3.2.1 Structural interpretation.....	59
3.2.2 Petrophysical methods.....	65
3.2.2.1 Porosity – total and effective .....	65
3.2.2.2 Permeability .....	73
3.2.2.3 Log-to-core calibration .....	80

3.2.3 Data analyses: Data transformation and variogram models .....	84
3.3 Model geometry definition – gridding and layering .....	91
3.3.1 Upscaling and property generation .....	93
3.3.2 Model population: Gaussian random function simulation algorithm .....	95
3.4 Discussion .....	99
3.4.1 Sources of uncertainty in static geological models .....	99
3.4.2 P10-50-90 Statistical analyses .....	101
CHAPTER FOUR: DYNAMIC FLUID-FLOW SIMULATION .....	104
4.1 Simulation input parameters .....	104
4.2 Simulation results .....	109
CHAPTER FIVE: DISCUSSION AND CONCLUSIONS .....	122
5.1 Discussion of uncertainties .....	122
5.2 Conclusions .....	124
5.3 Recommendations for future work .....	128
REFERENCES .....	129

## List of Tables

Table 1-1. Stratigraphic column outlining past and present nomenclature used for the FRS model study area modified from Nielsen et al. (2003). .....	16
Table 1-2. Acquisition parameters of the two stacked and migrated 3-D seismic volumes. ....	18
Table 1-3. A summary of the software used in the completed work for this project.....	19
Table 2-1. The major hydrogeological units in the stratigraphic column for the Newell County region, modified from Worley Parsons Komex (2008). ....	22
Table 2-2. Extrapolated directional groundwater flow based on a static groundwater map (Worley Parsons Komex, 2008).....	30
Table 3-1. Subsurface horizons correlated to the interpreted seismic reflector type and the expected approximate TWT occurrence.....	32
Table 3-2. Mistie pairs on the 2014 and 1997 3-D seismic volumes with the associated vertical and phase correction. ....	36
Table 3-3. Comparison chart of the velocities computed from the 10-22, 7-22, 7-21 TDR trendline equations and the averaged output interval velocities from the well tie process.....	47
Table 3-4. The velocity model produced from the three well TDR for the CMCRI 2014 3-D/3-C seismic volume. ....	49
Table 3-5. The velocity model produced from the three well TDR for the 1997 Cenovus 3-D/1-C seismic volume. ....	50
Table 3-6. Core lab measurement results from the RCA and TRA methods in the Foremost Formation and BBRS unit provided by Schlumberger Reservoir Laboratories Canada (2015).....	70
Table 3-7. Core measurement results from the RCA and TRA methods in the Foremost Formation and BBRS unit provided by Schlumberger Reservoir Laboratories Canada (2015).....	76
Table 3-8. Search cone parameters to bin and prepare the well log PHIE and K_INT data for the variogram experimental model fit.....	88
Table 3-9. The variogram model fitting parameters used for the PHIE and K_INT data for all 88 wells in the FRS study. ....	89
Table 3-10. Layered zones with the assigned cell thickness size for the FRS geomodel.....	92

Table 4-1. Number and size of cells used for upscaling the FRS geomodel with a tartan grid configuration. ....	104
Table 4-2. Reservoir simulation parameters used on the dynamic model for CO <sub>2</sub> injection. Modified from Lee (2015). ....	107
Table 4-3. The modified five-year injection plan used for the three dynamic model simulation scenarios. ....	109

## List of Figures and Illustrations

Figure 1-1. Global GHG equivalent emissions in megatons from 1990 to 2011 for selected developed and developing countries (Environment Canada, 2015).....	2
Figure 1-2. The simplified CCS process illustrating the steps from capture through to storage (modified from Li et al., 2011).....	3
Figure 1-3. The CO <sub>2</sub> pressure-temperature physical phase diagram modified from IPCC (2005). Note 1 bar = 0.1 MPa. ....	4
Figure 1-5. Preliminary FRS site layout by Lawton et al. (2014). Locations of wells and MMV instrumentation are outlined.....	11
Figure 1-6. Cropped map of Alberta outlining the location of the FRS study area (Google Maps, 2016). ....	15
Figure 2-1. Photo of the slabbed core interval identifying the sandstone beds within the Medicine Hat Member interval at a depth of 504 to 506 m. ....	23
Figure 2-2. Photo of the slabbed core interval identifying the caprock seal interval of the 1WS Member at a depth of 480 to 482 m. ....	25
Figure 2-3. Photo of the slabbed core interval identifying the sandstone reservoir of the BBRS unit at a depth of 298 to 300 m. ....	27
Figure 2-4. Photo of the slabbed core interval identifying the mixture of lithology within the Foremost Formation over the depth interval of 288 to 290 m. ....	28
Figure 3-1. A manual overlay of (A) previously interpreted 2-D seismic line (N – S) by Cenovus Energy, (B) a shortened 1985 2-D seismic line (N-S) , and (C) the initial P-P synthetic seismogram completed on the 7-22 well. ....	32
Figure 3-2. Top of the Mannville Gp depth-converted surface displaying the linear artefacts from the difference in TWT (ms) as interpreted on both the 1997 and the 2014 3-D seismic volumes. The outlined 1 km by 1 km area is the 2014 3-D seismic volume, occurring at an earlier TWT. The contoured intervals are every 2.5 m, where every bold line occurs every 5 <sup>th</sup> line. ....	34
Figure 3-3. Before and after horizon interpretation as a result of the mistie process on both the (A) CMCRI 3-D and (B) Cenovus 3-D seismic volumes. ....	37
Figure 3-4. BBRS unit isochron map displaying the interpreted TWT in both the Cenovus and CMCRI 3-D seismic volumes. The contoured intervals are every 1 ms, where every bold line occurs every 5 <sup>th</sup> line.....	38
Figure 3-5. Statistical zero-phase wavelet extracted at the 7-22-17-16W4 well from the P-P Cenovus 3-D seismic volume.....	41

Figure 3-6. Statistical zero-phase wavelet extracted at the 10-22-17-16W4 well from the P-P CMCRI 3-D seismic volume.....	41
Figure 3-7. Statistical zero-phase extracted wavelet at the 7-21-17-16W4 well from the P-P Cenovus 3-D seismic volume.....	42
Figure 3-8. Seismic horizon interpretation completed on the 1997 3-D seismic volume, inline 28 with the three wells (7-22, 7-21, 10-22 from left) tied in depth. The white squares on each horizon represent the well tops that have been depth converted. ....	43
Figure 3-9. Output interval velocity at the 7-22, 10-22, and 7-21 well with depth as a product of the well tie process. The seismic horizons displayed vertically are displayed at their respective interpreted depth as completed as the formation top interpretation on the wireline data at the 10-22 well location. ....	45
Figure 3-10. Time-Depth Relationship output as a result of the well tie process for the 7-22, 10-22, and 7-21 wells. The line of best fit for each TDR is plotted with the respective expression. ....	46
Figure 3-11. A display of the two 3-D seismic reflection volumes (A) Cenovus 1997 and (B) CMCRI 2014, with the three wells and well tops coinciding with their respective depth-converted subsurface horizons.....	51
Figure 3-12. Structural smoothing z-slice in the Cenovus 1997 3-D seismic volume at 242 ms, intersection the BBRS unit interpretation. The three wells 7-21 (green), 10-22 (red), and the 7-22 (orange) are displayed in the SW corner. ....	53
Figure 3-13. Semblance attribute map at z-slice 242 ms taken with a 3 ms x 3 ms x 15 ms filter window. The three wells 7-21 (green), 10-22 (red), and the 7-22 (orange) are displayed in the SW corner.....	54
Figure 3-14. Aggressive ant tracking attribute z-slice at 242 ms. The three wells shown are 7-21 (green), 10-22 (red), and 7-22 (orange).....	56
Figure 3-15. Spectral decomposition map at 50 Hz at a z-slice of 242 ms. The three wells 7-21 (green), 10-22 (red), and 7-22 (orange) are displayed in the SW corner. ....	57
Figure 3-16. Spectral decomposition map at 60 Hz at a z-slice of 242 ms. The three wells 7-21 (green), 10-22 (red), and 7-22 (orange) are displayed in the SW corner. ....	57
Figure 3-17. Spectral decomposition map at 70 Hz at a z-slice of 242 ms. The three wells 7-21 (green), 10-22 (red), and 7-22 (orange) are displayed in the SW corner. ....	58

Figure 3-18. Spectral decomposition map of 50 Hz at a z-slice of 694 ms, displaying various sinusoidal structures in the NW. The three wells 7-21 (green), 10-22 (red), and 7-22 (orange) are displayed in the SW corner.....	59
Figure 3-19. Sample well top interpretation on the 10-22 well, where the BBRS unit (pink), Pakowki Fm (green), and the Milk River Fm (orange) are shown. The last two columns show the PHIE and PHIT logs, where the core lab data is shown in purple (helium porosity) and in pink (PHIT).....	60
Figure 3-20. Subsurface structural map (above mean sea level) of the BBRS unit including interpretation from wireline and seismic data. The polygon represents the geomodel outline. The contours are every 3 m, every bold line occurs every 5 <sup>th</sup> line.....	63
Figure 3-21. The isopach map of the Foremost Formation. The polygon outlines the 25 sq. km model region. The contours are every 3 m, every bold line occurs every 5 <sup>th</sup> line.....	64
Figure 3-22. The isopach map of the BBRS unit. The polygon outlines the 25 sq. km model region. The contours are every 3 m, every bold line occurs every 5 <sup>th</sup> line. ....	64
Figure 3-23. Well section window of the 10-22 well displaying the PIGN, PIGE, and the core lab measurement points within the Foremost Fm and BBRS unit. The purple dots representing the helium porosity measurements (RCA), the red dots representing the total porosity measurements (TRA), and the green dots representing the effective porosity measurements (TRA). Note that the log calibration took place before this figure was taken.....	72
Figure 3-24. Well section window of the 10-22 well displaying the permeability in both the Foremost Fm and BBRS unit calculated using the Timur-Coates equation, the KINT_GEO permeability from the ELAN dataset, as well as the plotted core lab measurements. The nitrogen (orange), pressure-decay (pink), and Klinkenberg (blue) permeability points are superimposed over the calculated well logs. Note that the log calibration took place before this figure was taken. ....	78
Figure 3-25. The relationship between the calculated effective porosity and intrinsic permeability for the BBRS unit. ....	80
Figure 3-26. Before and after log-to-core calibration of K_INT data for the 10-22 injector well, from Swager (2015). ....	83
Figure 3-27. The input (a) and output (A) of a normal score transformation. The percentage of data represents the frequency of occurrence for PHIE values in the Foremost Formation.....	85
Figure 3-28. The input (b) and output (B) of a normal score transformation. The percentage of data represents the frequency of occurrence for PHIE values in the BBRS unit. ....	86

Figure 3-29. The input (c) and output (C) of a normal score transformation. The percentage of data represents the frequency of occurrence for PHIE values in the Pakowki Formation. ....	86
Figure 3-30. Resultant output of the normal score transformation on the PHIE data for the Foremost Formation, displaying the probability of occurrence for the modeled PHIE data range. ....	87
Figure 3-31. Resultant output of the normal score transformation on the PHIE data for the BBRs unit, displaying the probability of occurrence for the modeled PHIE data range. ....	87
Figure 3-32. Resultant output of the normal score transformation on the PHIE data for the Pakowki Formation, displaying the probability of occurrence for the modeled PHIE data range. ....	88
Figure 3-33. The major directional range in distance (m) with an exponential model variogram attempting to fit the PHIE data. ....	90
Figure 3-34. The minor directional range in distance (m) with an exponential variogram model attempting to fit the PHIE data. ....	90
Figure 3-35. The vertical directional range in distance (m) with an exponential variogram model attempting to fit the PHIE data. ....	90
Figure 3-36. The upscaled PHIE and K_INT curves displayed as blocked columns in a well section window for the 10-22 injector well within the BBRs unit and the Foremost Formation. ....	94
Figure 3-37. PHIE histogram for the BBRs unit, displaying how the data is represented in the well logs (red), upscaled cells (green), and modeled property (purple) in the 3-D model. ....	96
Figure 3-38. K_INT histogram for the BBRs unit, displaying how the data is represented in the well logs (red), upscaled cells (green), and modeled property (purple) in the 3-D model. ....	97
Figure 3-39. The 25 sq. km FRS model populated with PHIE in the Foremost Fm, BBRs unit, and Pakowki Fm. Wells below the model section display the upscaled cells. ....	98
Figure 3-40. The 25 sq. km FRS model populated with K_INT in the Foremost Fm, BBRs unit, and Pakowki Fm. Wells below the model section display the upscaled cells. ....	98
Figure 3-41. Assigned pore volume bins based on pore volume sum data. The plot displays the occurrence frequency for the BBRs unit in a 1 km by 1 km clipped volume centered on the main 10-22 injector well in the FRS model. ....	102

Figure 3-42. Total effective pore volume data for the BBRs unit in the 1 km by 1 km clipped volume. The occurrence frequency and pore volume actual frequency are shown to demonstrate the corresponding P10-50-90 percentile case ranking. ....	103
Figure 4-1. The tartan grid used to upscale the static geomodel. Finer cell sizes (8.4 x 8.4 x 0.5 m) are located closer to the 10-22 injector well. Modified from Lee (2015). ....	105
Figure 4-2. Upscaled 3-D grid of the dynamic model demonstrating the tartan grid configuration used. The three zones consisting of the Foremost Fm, BBRs unit, and Pakowki Fm are labelled. Figure modified from Lee (2015) with a Vertical Exaggeration (V.E.) of 5. ....	106
Figure 4-3. A Brooks-Corey model modification by Lee (2015) to approximate relative permeability of CO <sub>2</sub> to water saturation. ....	108
Figure 4-4. Simulated CO <sub>2</sub> injection into the BBRs unit over a five-year period constrained by the maximum allowable BHP. Figure taken by Lee (2015). ....	111
Figure 4-5. 3-D cross-section displaying the gas saturation and distribution of the injected CO <sub>2</sub> plume one-year into the injection period for the P50 case in the heterogeneous geodynamic model with V.E. of 1. ....	114
Figure 4-6. 3-D cross-section displaying the distribution of the injected CO <sub>2</sub> plume five years into the injection period for the P50 case in the heterogeneous dynamic model with V.E. of 1. ....	115
Figure 4-7. 3-D cross-section display of the distribution of the injected CO <sub>2</sub> plume 1 year post-injection for the P50 case in the heterogeneous geodynamic model with V.E. of 1. ....	116
Figure 4-8. 3-D cross-section display of the distribution of the injected CO <sub>2</sub> plume 10 years post-injection for the P50 case in the heterogeneous geodynamic model with V.E. of 1. ....	117
Figure 4-9. CO <sub>2</sub> saturation profile along the E-W direction for the P50 case of the heterogeneous geodynamic model. (A) After one-year during the injection period, (B) after five-years during the injection period, (C) one-year post-injection period, and (D) ten-years post-injection period. Figures taken and modified from Lee (2015). ....	118
Figure 4-10. Plan view of the simulated scenarios for the P50 case of the heterogeneous geodynamic model, depicting the CO <sub>2</sub> plume edges. Figure taken and modified from Lee (2015). ....	119
Figure 4-11. The pressure plume build-up sequence developed in the dynamic geomodel after (A) one-year of injection, (B) five-years of injection, (C) one-year post-injection, (D) five-years post-injection, and (E) ten-years post-injection	

period. The main injector well 10-22 is displayed in red running through each sub-figure. Note 1 bar = 0.1 MPa. .... 120

## List of Symbols, Abbreviations, and Nomenclature

<b>Symbol</b>	<b>Definition</b>
%	Percentage
*	Multiplication
°	Degree
$\phi$	Total Porosity
>	Greater than
<	Less than
$\approx$	Approximately Equal to
$\Delta p$	Differential Pressure
xx	Scalar Multiplier
1-C	One-Component
3-C	Three-Component
2-D	Two-Dimensional
3-D	Three-Dimensional
4-D	Four-Dimensional
1WS	First White Specks Member
AER	Alberta Energy Regulator
asl	Above Sea Level
API	American Petroleum Institute (Gamma Ray Units)
atm	Atmosphere
BBRS	Basal Belly River Sandstone
BF	Bound-fluid
BFV	Bound-fluid Volume
BHP	Bottom-Hole Pressure
C	Centigrade
CCS	Carbon Capture and Storage
CH <sub>4</sub>	Methane Gas
Cm	Centimetre
CMC	Carbon Management Canada
CMR	Combinable Magnetic Resonance
CO <sub>2</sub>	Carbon Dioxide Gas
CREWES	Consortium of Research in Elastic Waves Exploration Seismology
DPSS	Density Porosity Log Calibrated to Sandstone
DT	Transit Time or Sonic Log
dX	Change in the X-direction
dY	Change in the Y-direction
E	Easting
ELAN	Elemental Log Analysis
EOR	Enhanced Oil Recovery
ERP	Emergency Response Plan
FF	Free-Fluid

FFV	Free-Fluid Volume
Fm.	Formation
FRS	Field Research Station
g/cc	Grams per Cubic Centimeter
GGs	Gaussian Geostatistical Simulation
GHG	Greenhouse Gas
GPS	Global Positioning System
GRFS	Gaussian Random Function Simulation
GR	Gamma Ray
h	Thickness
He	Helium Gas
HC	Hydrocarbon
Hz	Hertz
I	Impedance
IEAGHG	International Energy Agency Greenhouse Gases
Inj.	Injection
inSAR	Interferometric Synthetic Aperture Radar
K_INT or $k$	Intrinsic Permeability
$k_{\text{CO}_2\text{-H}_2\text{O}}$	Relative Permeability of CO <sub>2</sub> to H <sub>2</sub> O
kg/m <sup>3</sup>	Kilograms per Cubic Meter
$k_h$	Horizontal Permeability
KINT_GEO	Intrinsic Permeability (ELAN)
Km	Kilometer
$k_{\text{TIM}}$	Timur-Coates Permeability
$k_v$	Vertical Permeability
$k_v/k_h$	Ratio of Vertical to Horizontal Permeability
m	Meter
m <sup>3</sup> /day	Cubic Meter per Day
m/s	Meters per Second
Max	Maximum
mD	Millidarcy
μs/ft	Micro-seconds per Feet
mg/L	Milligrams per Liter
Min	Minimum
mm	Millimeter
MMV	Measurement and Monitoring Verification
MPa	Mega-Pascal
MPa/km	Mega-Pascal per Kilometer
ms	Milliseconds
N	Northing
n	Number of Cells
N <sub>2</sub>	Nitrogen Gas
N-S	North-South
NAN	Not a Number (Does not exist)
NE	North-East

NMO	Normal Move Out
NMR	Nuclear Magnetic Resonance
NPSS	Neutron Porosity Calibrated to Sandstone
NW	North-West
nX	Number of Cells in the X-direction
nY	Number of Cells in the Y-direction
nZ	Number of Cells in the Z-direction
Pa	Pascal
PHIE	Effective Porosity
PHIT	Total Porosity
PIGE	Effective Porosity with bound water
PIGN	Total Porosity without bound water
ppm	Parts Per Million
P-impedance	Compressional Impedance
P-wave	Compressional Wave
psi	Pounds per Square Inch
PVT	Pressure-Volume-Temperature
QC	Quality Control
R	Reflectivity
RC	Reflection Coefficients
RCA	Routine Core Analysis
RHOB or $\rho$	Bulk Density
S	Southing
$S_{gCO_2}$	Saturation of Carbon Dioxide Gas
$S_w$	Water Saturation
$S_{wcr}$	Critical Water Saturation
$S_{wmax}$	Maximum Water Saturation
$S_{wmin}$	Minimum Water Saturation
$S_{wirr}$	Irreducible Water Saturation
S-wave	Shear Wave
SE	South-East
sq. km	Square-Kilometer Area
STP	Standard Temperature and Pressure
T	Period
t	Ton
t/CO <sub>2</sub>	Tons per CO <sub>2</sub> gas
TDR	Time-Depth Relationship
TDS	Total Dissolved Solids
TRA	Tight Rock Analysis
TWT	Two-Way Time
v	Velocity
V/V	Volume/Volume
$V_p$	Compressional Wave Velocity
$V_p/V_s$	Ratio between P-wave and S-wave Velocity
$V_s$	Shear Wave Velocity
$V_{shale}$	Volume of Shale

V.E.  
Volume\_Clay  
VCL  
VSP  
VXBW  
W  
WCSB

Vertical Exaggeration  
Volume of Clay  
Volume of Clay  
Vertical Seismic Profiling  
Volume of Bound Water  
Westing  
Western Canada Sedimentary Basin

## Chapter One: **Carbon Management**

### **1.1 CO<sub>2</sub> Capture and storage: A step forward**

Carbon dioxide, CO<sub>2</sub>, is a naturally occurring Greenhouse Gas (GHG) that is a minor constituent of the atmosphere and plays a key role in the environment. Not only does the chemical compound absorb infrared radiation in the atmosphere, but it also plays a critical role in the weathering of rocks and is the direct input for photosynthesis – producing organic matter that serve as carbon sinks within the biosphere (Hansell and Carlson, 2013). Since the onset of the Industrial Revolution from the 18<sup>th</sup> Century, urbanization and industrial processes have taken flight leading to increasing fossil fuel emissions. This anthropogenically induced increase has offset the balance of the carbon cycle that the Earth naturally has in place for releasing and storing carbon compounds.

The increasing GHG emissions into the atmosphere through anthropogenic activities have been identified as a driver for global climate change. Almost 80% of the GHG emissions from human sources are from burning fossil fuels and industrial processes, which are likely to be the dominant cause of the observed warming that has occurred since the mid-20<sup>th</sup> Century (Environment Canada, 2015). In Figure 1-1, the chart shows that between 1990 and 2011, global GHG emissions grew by approximately 42%, and even though Canada contributes approximately less than 2%, emissions still grew by 19% during this period (Environment Canada, 2015). With this increase of GHG emissions, consequences will follow to impact not only the environment, but also human health and the economy as a whole.

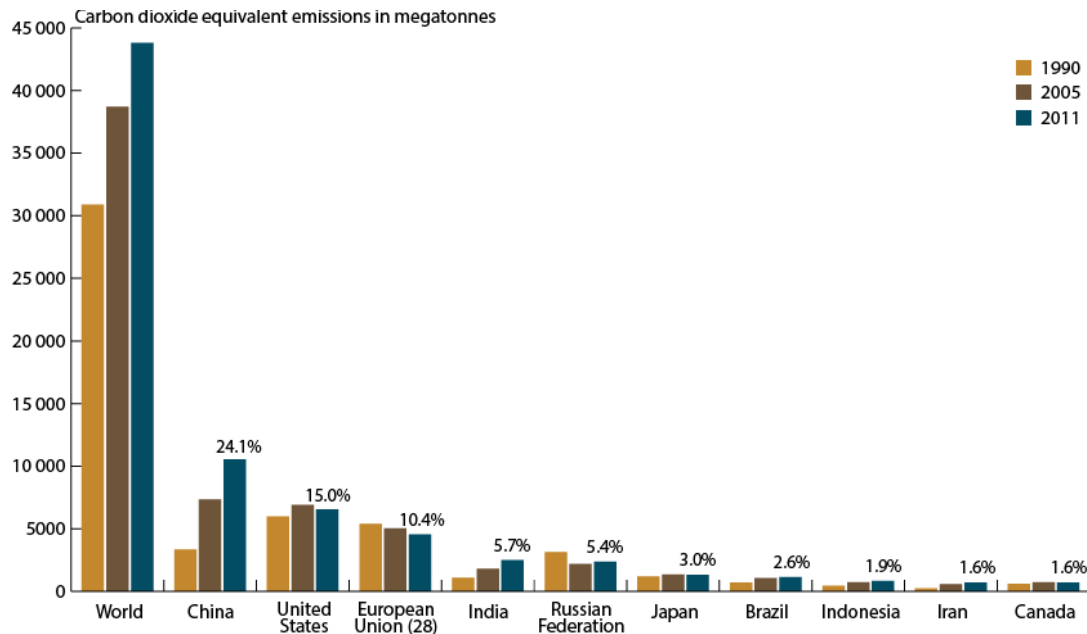


Figure 1-1. Global GHG equivalent emissions in megatons from 1990 to 2011 for selected developed and developing countries (Environment Canada, 2015).

One method that can capture up to 90% of the CO<sub>2</sub> emissions produced from burning fossil fuels from large stationary sources, and industrial processes is Carbon Capture and Storage (CCS) (Newmark et al., 2010). CCS is a method of sequestration acting to reduce increasing CO<sub>2</sub> concentrations in the atmosphere. The chain process (Figure 1-2) consists of CO<sub>2</sub> capture, conditioning (dehydration, non-condensable gas separation, and/or liquefaction, compression/pumping, transport) (Li et al., 2011), and long-term isolated subsurface storage that is injected typically in a supercritical phase (IPCC, 2005; Alshuhail, 2011).

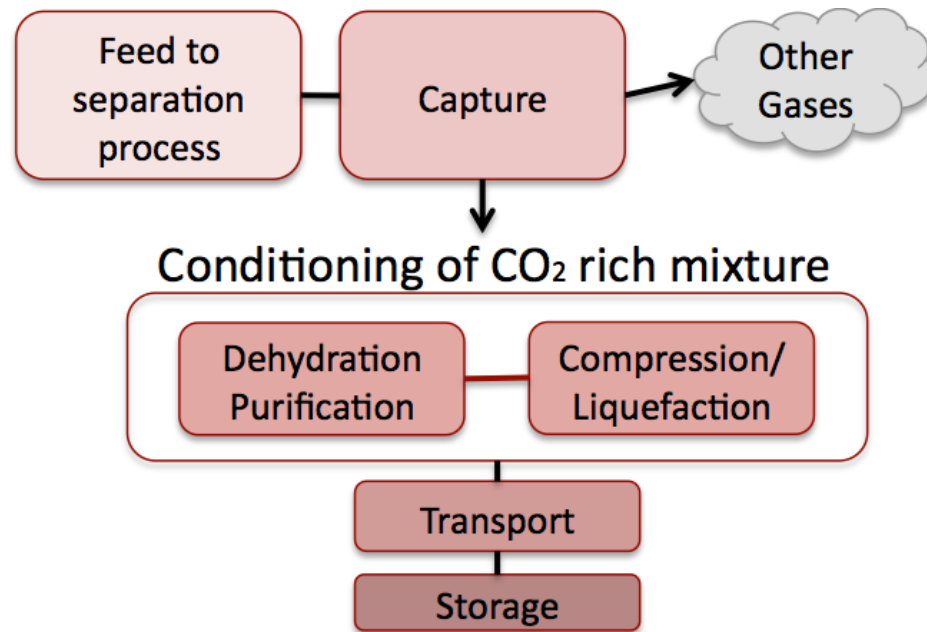


Figure 1-2. The simplified CCS process illustrating the steps from capture through to storage (modified from Li et al., 2011).

For successful sequestration, the injection reservoir interval must have the capacity to store the CO<sub>2</sub>, which is dependent on the porosity, permeability, pressure, depth, and temperature of the formation (IPCC, 2005). The pressures used for injection must not exceed caprock failure pressures, as this will lead to induced fracturing not only in the target interval, but also potentially in the impermeable seal above (Alshuhail, 2011; Bachu, 2002). To ensure proper confinement and isolation of the CO<sub>2</sub>, there must be a seal or a set of impermeable layers above the target interval to prevent mobility and leakage.

## 1.2 CO<sub>2</sub> Properties

The Pressure-Volume-Temperature (PVT) properties of CO<sub>2</sub> require consideration when performing site selection for a CCS project. The pressure, temperature, and storage capacity of the reservoir will be dependent on the stratigraphic depth, requiring preparation and adjustments for the CO<sub>2</sub> to be injected. The physical phase of CO<sub>2</sub> has a temperature-pressure relationship, shown in Figure 1-3.

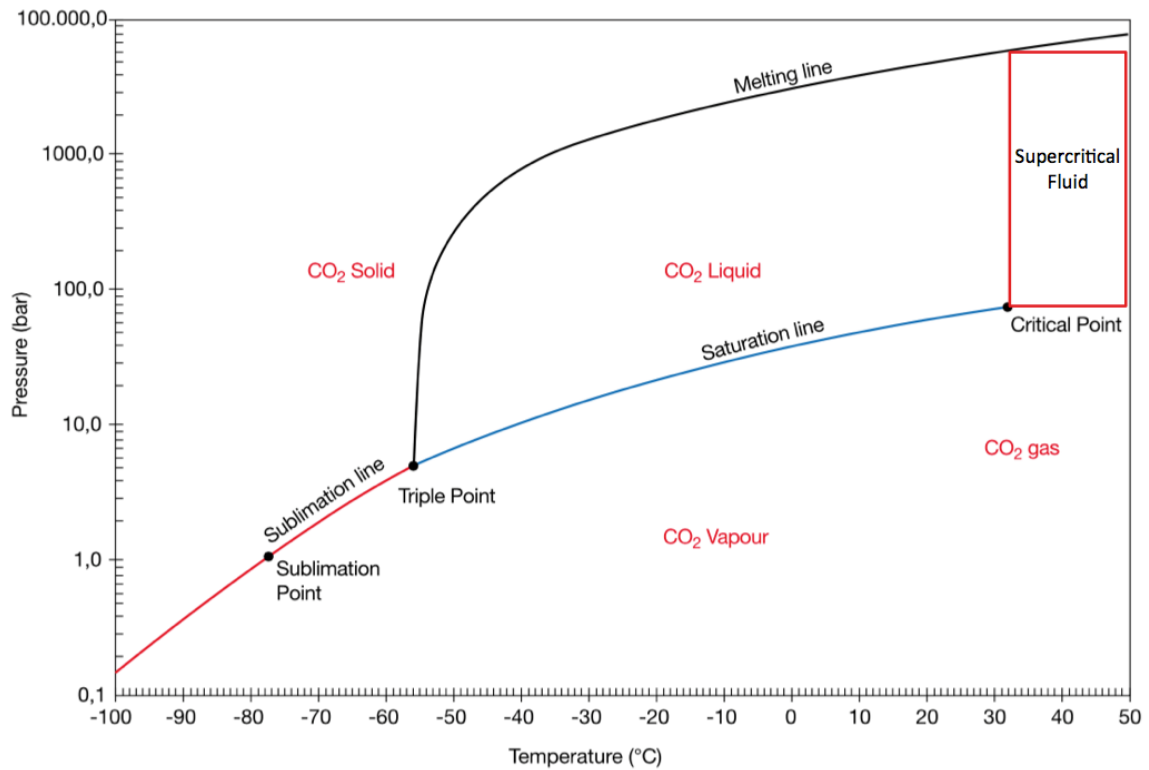


Figure 1-3. The CO<sub>2</sub> pressure-temperature physical phase diagram modified from IPCC (2005). Note 1 bar = 0.1 MPa.

The standard temperature and pressure (STP) conditions on Earth’s surface where CO<sub>2</sub> remains in a gaseous phase are 0°C and approximately 1 atmosphere (atm) or 10,000 Pascals (Pa) (Calvert, 2009). Factors that will affect the CO<sub>2</sub> injected into a reservoir other than temperature and pressure include the mineralogy of the formation and the pore fluid composition. These four factors will govern how the injected CO<sub>2</sub> will react with the reservoir.

For all CCS projects that occur within Alberta, legislation by the Alberta Energy Regulator (AER) requires that the target interval for CO<sub>2</sub> sequestration be at a depth greater than 1000 meters (Alberta Energy, 2013). At this depth, CO<sub>2</sub> will be a supercritical fluid as both the temperature and pressure exceed the critical point of 31°C and 7.3 MPa (Cummings et al., 2012). Note that the lithostatic and hydrostatic pressure, as well as geothermal gradients differ with geographic location; thus each sequestration project is unique. The physical state of the CO<sub>2</sub> will impact the type of Monitoring and

Measurement Verification (MMV) technologies within the monitoring plan that aim to manage and mitigate the assessed potential risk associated with CO<sub>2</sub> injection.

### **1.3 Trapping mechanisms**

There are four types of trapping mechanisms that enable carbon sequestration. These include hydrostatic, residual, solubility, and mineral trapping methods. Depending on the reservoir's rock and pore fluid geochemistry, as well as its storage capacity, these four trapping mechanisms will occur over the duration of the injection and storage process for any CCS project. A brief summary of each type can be seen below, however for further descriptive details see the work completed by Zhang and Song (2014).

#### ***1.3.1 Stratigraphic trapping***

Injected CO<sub>2</sub> (supercritical fluid or gaseous state) into a porous reservoir trapped by an overlying impermeable and laterally extensive caprock that prevents vertical migration. As a result of the buoyancy of the CO<sub>2</sub>, it will percolate up through the reservoir rock and accumulate at the reservoir/caprock interface. This type of trapping mechanism is considered to be a “prerequisite for any storage site to prevent leakage of CO<sub>2</sub> during the time it takes for the other trapping mechanisms to come into effect” (Zhang and Song, 2014). (Zhang and Song, 2014; Nelson et al., 2005; CCP, 2015; McPherson, 2012)

#### ***1.3.2 Residual trapping***

Injected CO<sub>2</sub> (supercritical fluid or gaseous state) displaces the formation fluid in the rock pore spaces. Once the injection period is completed, the CO<sub>2</sub> percolates up through the rock as a result of buoyancy and the formation fluid then replaces the volume of occupancy. This mechanism occurs relatively fast, and capillary forces are dominant where the majority of CO<sub>2</sub> has migrated upward due to density differences – however disconnected droplets of CO<sub>2</sub> will remain immobile within pores of the rock (Zhang and

Song, 2014). (Zhang and Song, 2014; Nelson et al., 2005; CCP, 2015; McPherson, 2012)

### ***1.3.3 Solubility trapping***

The solubility of CO<sub>2</sub> is dependent on the temperature, pressure, pH, salinity, as well as other aqueous chemical compounds that are present within the formation fluid. Injected CO<sub>2</sub> (supercritical fluid or gaseous state) into a porous reservoir dissolves into the formation fluid and produces carbonic acid, as well as bicarbonate and carbonate ions which can act to lower the pH of the formation fluid (McPherson, 2012; CPP, 2015). The pore fluids are only able to dissolve approximately 5% of the injected CO<sub>2</sub> by mass (McPherson, 2012), resulting in the slow dissolution rates. The dissolution of CO<sub>2</sub> primarily occurs at the caprock-reservoir interface, where the buoyant CO<sub>2</sub> will accumulate. The formation fluid with dissolved CO<sub>2</sub> is denser than that without, creating not only a density gradient but also a concentration gradient. This creates a convection system causing the formation fluid with dissolved CO<sub>2</sub> to sink to the bottom of the reservoir, and brings other volumes of formation fluid in contact with the injected CO<sub>2</sub> (Zhang and Song, 2014). (Zhang and Song, 2014; Nelson et al., 2005; CCP, 2015; McPherson, 2012)

### ***1.3.4 Mineral trapping***

Dissolved CO<sub>2</sub> reacts with the divalent cations within the formation fluid present in the reservoir to precipitate solid carbonate minerals. Depending on the original geochemistry prior to injection, reaction kinetics may differ. Carbonate minerals such as calcite, magnesite, and siderite have been found to form at a faster rate than wollastonite, forsterite, and kaolinite (McPherson, 2012). Although some of the minerals formed can undergo reverse reactions that tend to occur slowly, this depends on the temperature, pressure, salinity, pH, and concentrations of other chemical compounds found in the formation fluid (Zhang and Song, 2014). Generally this type of trapping mechanism is considered to be permanent and a stable form of sequestering CO<sub>2</sub>, with the downfall of

lengthy geological time periods for successful storage. (Zhang and Song, 2014; Nelson et al., 2005; CCP, 2015; McPherson, 2012)

#### **1.4 Reservoirs for sequestration**

There are two main types of sites for the interest of sequestration, these include saline-water (brine) formations and depleted hydrocarbon (HC) reservoirs (Hovorka et al., 2008). For CCS in depleted HC reservoirs, the geometry of the reservoir, seal integrity, and physical trapping mechanism are known (Lawton et al., 2014) due to previous investigations prior to and during production. The injection of CO<sub>2</sub> has also been used for enhanced oil recovery (EOR), by reversing the trends of pressure decline, due to the miscibility of CO<sub>2</sub> within oil to increase the volume and decrease the viscosity of the remaining oil to promote mobility (Hovorka et al., 2008). One potential risk for this type of site is leakage through abandoned wells.

With CCS in deeper brine formations, there are multiple seals that may overlay the interval to prevent vertical movement of the plume, with few wells penetrating the formation to cause leakage pathways (Lawton, 2013). The main trapping mechanism with this site type is solubility, which may pose risks if the reservoir itself is not geometrically confined, especially since there is typically little knowledge on the integrity of the seal (Lawton, 2013) due to the lack of exploration.

#### **1.5 Monitoring, measurement, and verification plans: An overview**

During the preliminary stages of a CCS project, one of the key elements in managing and mitigating risks come from the development of a reliable and cost-effective pre-injection Monitoring Measurement Verification (MMV) plan. Once reviewed and granted, the operating company is responsible for deploying the MMV throughout the life cycle of the project, to define baseline measurements and the sequential of those taken after CO<sub>2</sub> injection into the subsurface. Each MMV plan is site-specific, and the frequency of monitoring with selected technologies is outlined in a schedule for the entire span of the CCS project. Similarly to constructing an Emergency

Response Plan (ERP), a MMV plan ensures that all potential situations that have been analyzed for risk have been considered with pre-planned procedures with an effective response to take place immediately in the case of an emergency (Alberta Energy, 2013).

Throughout the duration of injection period, data are acquired utilizing the selected MMV technologies to demonstrate containment and conformance of the CO<sub>2</sub> in the subsurface. This is to ensure operations are not affecting the health and safety of the public and surrounding environment. In the province of Alberta, an updated MMV plan utilizing results from deployed monitoring technologies must be submitted to the AER every three years. Data acquisition utilizing the selected MMV technologies occurs throughout the duration of injection period, to demonstrate containment and conformance of the CO<sub>2</sub> in the subsurface. The data can also be used to update geostatic models and used for further fluid simulations to further predict the behaviour of the CO<sub>2</sub> injected. In the province of Alberta, the AER requires an updated MMV and closure plan based on operational data that has been acquired to ensure the safety and health of the general public and the surrounding environment. (Alberta Energy, 2013)

Preserving the site environment requires monitoring of the surrounding soil, groundwater, air, as well as the integrity of the caprock and stress regime within the reservoir. Any changes of chemical concentrations, pressure profiles, or distribution of the CO<sub>2</sub> plume within the subsurface is required to be monitored. There are many Best Practices Manuals (BPM) available to the general public that outlines observations and specific guidelines for site-specific CCS projects (e.g. CSLF, 2013). Monitoring programs aim to select tools which consider CO<sub>2</sub> plume imaging, caprock integrity, CO<sub>2</sub> migration into the overburden, quantification of in-situ CO<sub>2</sub>, reservoir storage efficiency, calibration of flow simulations, CO<sub>2</sub> leakage at surface, induced seismicity, and lastly well integrity (Chadwick et al., 2008).

Technologies selected should reflect a cost-benefit relationship, which target both deep and shallow monitoring objectives. A ranking system was developed for Shell Canada's QUEST CCS project located in Fort Saskatchewan, Alberta with the highest value ranking technologies to include: down-hole pressure-temperature gauge, well-head CO<sub>2</sub> detectors, satellite or airborne hyperspectral image analysis, cement bond logs,

annulus pressure monitoring, operational integrity assurance system, time-lapse temperature logging, 3-D Vertical Seismic Profiling (VSP), 3-D surface seismic, Interferometric Synthetic Aperture Radar (inSAR), time-lapse saturation logging, time-lapse density logging, mechanical well integrity pressure testing, time-lapse sonic logging, artificial tracer monitoring, and time-lapse surface microgravity (CCSNetwork, 2012). Another industrial scale CCS project within Canada includes the International Energy Agency Greenhouse Gases (IEAGHG) Weyburn CCS project located in the Midale field, Saskatchewan. Technologies selected for the designed MMV plan include: baseline 3-D seismic surveys, time-lapse 3-D surveys with permanent arrays, passive seismic surveys, controlled-source electromagnetics, time-lapse gravity, inSAR, Global Positioning System (GPS), tiltmeters, groundwater and soil-gas monitoring, cross-well seismic and electrical monitoring, surface-to-downhole electrical monitoring, real-time pressure and temperature, fluid sampling, time-lapse VSP, and cross-well seismic (CCSNetwork, 2012). Depending on the scale of the project, some technologies may propose greater cost efficiency than others – however, the lists of technologies for both sites aim to provide confidence in the storage security of the injected CO<sub>2</sub>.

Great volumes of research and development on carbon sequestration have been completed, and continue as there are still uncertainties that remain. Small-scale pilot sites are a required step in research and development to challenge and enhance the technologies at a scale greater than that tested at the lab bench. By testing hypotheses at a pilot scale, detection thresholds, imaging limitations, and the reliability of the monitoring techniques can truly be defined with room for improvement.

## **1.6 From bench to field: What is the Field Research Station?**

The Field Research Station (FRS) is a field pilot site located in Newell County, Alberta and serves to bridge the gap between research completed on the lab bench scale and projects focused on building technologies that are economically sustainable to operate and be implemented at a larger industrial CCS project scale (Figure 1-4).

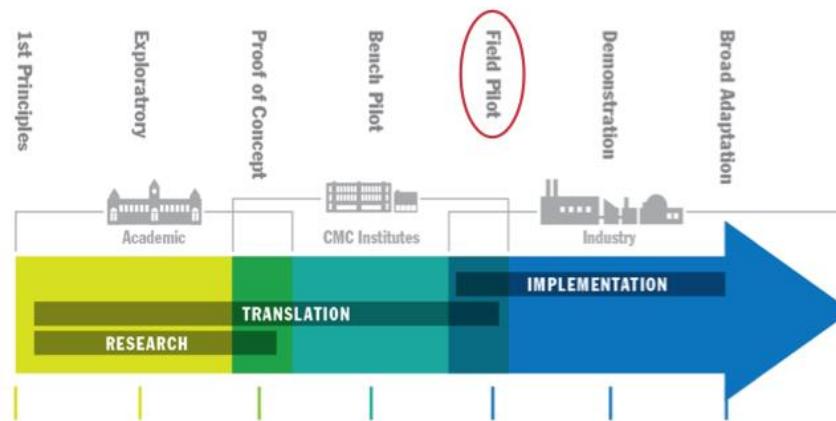


Figure 1-4. Applied spectrum that constitutes CCS projects. Modified from Lawton et al. (2014).

The FRS was established by Carbon Management Canada (CMC) Research Institutes under the Containment and Monitoring Institute (CaMI), where there are four main research themes to be incorporated through the lifetime of the FRS. These include the (1) Recovery, Processing, and Capture, (2) Emerging and Enabling Technology, (3) Secure Carbon Storage, and (4) Accelerating Deployment. The site will be available for a broad suite of researchers, and act to test cutting-edge MMV technologies for the injection and storage of up to 5000 tons (t) of CO<sub>2</sub> injected over a five-year interval. More specifically, the detection thresholds of current MMV technologies will be assessed, new MMV technologies will be developed for fluid monitoring, as well as contributing efforts to improve and enhance 4-D seismology for fluid containment and conformance.

Upon permit approval, the FRS will undertake controlled CO<sub>2</sub> release of up to approximately 1000 t per year into the brine formation interval target A, located at 300 m depth. It is important to note that the FRS will not serve as a long-term storage site. The FRS will deploy various monitoring techniques and will be able to determine CO<sub>2</sub> detection thresholds for new MMV technologies, and will be the first of its kind internationally. Figure 1-5 demonstrates the FRS site layout of planned infrastructure, including the proposed injection and monitoring wells alongside locations of monitoring technologies.

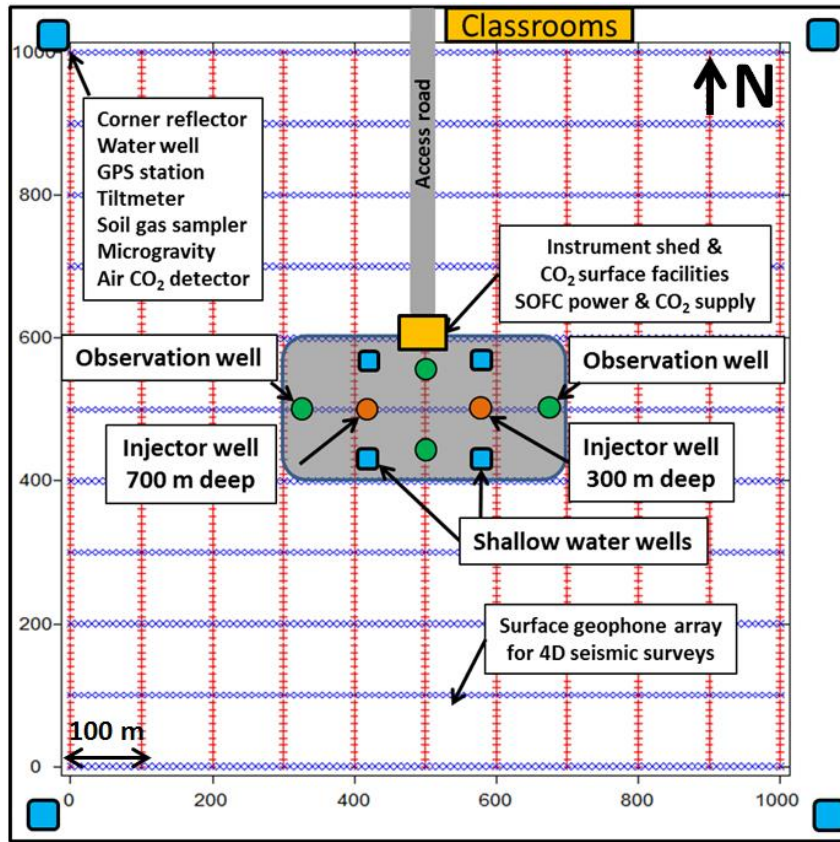


Figure 1-5. Preliminary FRS site layout by Lawton et al. (2014). Locations of wells and MMV instrumentation are outlined.

The development of this research site will not only address health, safety, and environmental concerns – but will act to test injection and reservoir management, and models that have only been tested virtually. Implementation of MMV technologies over the course of a CCS project is required not only by regulators, but also is needed to confirm the behaviour of the CO<sub>2</sub> in the subsurface, to gain acceptance by the public, as well to reduce any potential liability for the study area in the future. Each CCS project is unique in that no storage site is the same, thus determining the fate of injected CO<sub>2</sub> will depend on different monitoring plans that will be site-specific. By improving MMV technologies, the management and mitigation of the risks associated with CO<sub>2</sub> sequestration will improve as well.

The region of study is geologically stable with flat-lying subsurface layers, with no observed fault structures. Seismic interpretation of reflection and imaging techniques

have provided a means to identify and characterize the lack of any discontinuities, and an understanding of the regional behaviour of the lithology and thickness of layers that are of interest for CO<sub>2</sub> sequestration.

The FRS comprises primary efforts from CMC Research Institutes (CMCRI), the Consortium of Elastic Wave Exploration Seismology (CREWES) at the University of Calgary, and Cenovus Energy.

### **1.7 Thesis objectives**

The main objective behind this thesis is to construct a static geomodel that incorporates both geological and geophysical characterization of the target A and seal A intervals of the FRS site. The analyses and fluid-flow simulation results, where up to 5000 t/CO<sub>2</sub> is injected in gas-phase into the main target interval A over a total five-year duration, will be used towards obtaining an injection license as part of Directive 051 from the Alberta Energy Regulator.

Utilizing the available but limited wireline, core, and seismic data, the geomodel is populated by two main calculated petrophysical parameters which include effective porosity and intrinsic permeability. The characterization of the target interval will provide storage capacity and injectivity information, which is governed by the connected pore spaces and fluids present in the reservoir. The characterization of the seal interval will provide information about the caprock integrity, where the lithology and continuity of the stratigraphy determine the risks and fate of the CO<sub>2</sub> gas plume. Intra-formational fractures or faults need to be identified and characterized to understand the potential and preferential leakage pathways. The pressure and temperature regimes play a key role on the phase of injected CO<sub>2</sub> volumes, thus governing the dominant type of trapping mechanism to occur once injected. The construction of this static geomodel will illuminate the expected structural and geochemical trapping mechanisms based on the conducted geological and geophysical interpretation.

The fluid-flow simulations will act as preliminary educated estimates of how both the target and seal intervals will react when subject to the controlled release of CO<sub>2</sub> over time. Knowledge of the plume behaviour including its size, shape, and distribution in the

subsurface is required to assess the potential risks associated and related to larger industrial CCS projects. The dynamic geomodel and simulation results will provide a basis of simulator parameters required, and will illuminate where remaining static and dynamic uncertainties exist.

The product of this work will provide a baseline of characterization, where automatic workflows have been established to allow for the static model to be updated and refined upon acquisition of newer datasets. The simulation results of injecting up to 5000 t/CO<sub>2</sub> in gas-phase will also provide insight into the calculated plume behaviour, and guide the location of monitoring technologies and sampling strategy to be used in the MMV plan. Most importantly, the value of this work presents a Best Practice Manual demonstrating a methodological workflow to incorporate integrated datasets to aid in the characterization of a target formation, and can be applied in other academic and commercial studies.

## **1.8 Thesis contributions**

All of the work presented henceforth represents combined efforts with collaboration from the University of Calgary, CMC Research Institutes, CREWES, Schlumberger Ltd., Cenovus Energy, Husky Energy, and Taurus Reservoir Solutions Ltd. I was the lead investigator responsible for the manuscript composition, data collection, as well as the research and analysis completed throughout Chapter 1 – 5. Specific contributions for Chapter 3 include the baseline characterization of the geophysical datasets, involving seismic interpretation, seismic well ties, velocity modeling, and seismic attribute work. The two 3-D seismic volumes were provided by Cenovus Energy (1997) and CMC Research Institutes (2014). As for the geological dataset, I completed wireline interpretation, petrophysical calculations, data transformation and variogram analyses. Roy Lindseth provided his efforts in editing the manuscript.

Christian Abaco (Senior Geophysicist, Husky Energy) was involved in the seismic attribute work, providing conceptual formation of attribute calculations, and aided with computing the spectral decomposition and semblance seismic attributes.

Wade Zaluski (Senior Geologist, Schlumberger Ltd.) was involved in quality control, quality assurance, and troubleshooting throughout the project duration. Specific contributions include providing a set of equations used for computing the structural model surfaces, the early stages of the seismic well-tie process, assisted with the petrophysical calculations of effective porosity and intrinsic permeability, contributed assistance with the data transformations and variogram analyses, and provided the P10-50-90 framework equations in Chapter 3. He also was heavily involved in contributing to the construction of the static model. This includes aiding with defining the model geometry, upscaling logs, and property generation using the Gaussian random function simulation algorithm.

Lee Swager (Senior Petrophysicist, Schlumberger Ltd.) was involved in completing the Electrical Log Analysis for the 10-22-17-16W4 well, derived the petrophysical approach and equations for effective porosity, volume of clay, and bound/free-fluid volumes, provided conceptual background information about wireline calculations and core lab analyses, as well as completing the log-to-core calibration calculations for the 10-22-17-16W4 well in Chapter 3. The core plugs were provided by CMC Research Institutes, and lab analyses were conducted by Schlumberger Reservoir Laboratories Canada.

Si-Yong Lee (Principal Reservoir Engineer, Schlumberger Ltd.) contributed to the early stages of the variogram analyses, conducted the fluid-flow simulations for the dynamic modeling, and provided conceptual background information from the dynamic modeling results for Chapter 4. Specific contributions include upscaling the dynamic model using a tartan gridding method, compile the fluid-flow simulation parameters, modified the injection plan for dynamic modeling, and lastly, provided the figures demonstrating the fluid-flow simulation results for the P50 case. Somayeh Goodarzi (Reservoir-Geomechanics Engineer, Taurus Reservoir Solutions Ltd.) provided the rock compressibility required for dynamic modeling, calculated from three core plug samples near the target interval at 300 m depth.

## 1.9 Study area

The study area is within the province of Alberta, located in Newell County approximately 190 km southeast of Calgary (Figure 1-6) in Section 22, Township (TWP) 17, and Range 16 west of the 4th Meridian. The lease of the land is courtesy of Cenovus Energy, that has previous access to approximately a  $\frac{3}{4}$  section and the FRS utilizes 1 square-kilometre (sq. km) of the area. Site selection was based on the open field and road access, the near-flat terrain, quiet ambient seismic noise levels, and the lack of high-pressure pipelines in the area (Lawton, 2013). There are two intervals that appear to be suitable sand reservoir units, with overlying shale-sand sequences for caprock intervals. As well, many seismic and wireline datasets pre-exist in the area for initial site characterization.



Figure 1-6. Cropped map of Alberta outlining the location of the FRS study area (Google Maps, 2016).

For stratigraphic reference the outline for the primary and secondary injection zones and seals are listed in Table 1-1. Initially, this study aimed to characterize and simulate a primary and secondary target interval for CO<sub>2</sub> injection. The geological background of both will be discussed, however further reservoir characterization and modeling will focus on the primary injection target interval known as Target A. Target A is located at 300 m depth, known as the Basal Belly River Sandstone (BBS) unit. Target B is located at 500 m depth, known as the Medicine Hat Member (Mb).

Table 1-1. Stratigraphic column outlining past and present nomenclature used for the FRS model study area modified from Nielsen et al. (2003).

<i>McNeil and Caldwell (1981)</i> <i>Webb et al. (2005)*</i> <i>Nielsen and Schröder-Adams (1999)**</i> <i>Leckie and Smith (1992) ***</i>			<b>THIS STUDY</b> <i>After Nielsen et al. (2003),</i> <i>Leckie et al. (2004), and</i> <i>Christopher et al. (2006)</i>			<b>Well Tops &amp; Seismic Horizons Used</b>	<b>General Lithology</b>	<b>Reservoirs &amp; Seals</b>
<b>PERIOD</b>	<b>STAGE</b> <b>AGE (Ma)</b>	<b>SEDIMENTARY CYCLES</b>	<b>ALBERTA SOUTHERN PLAINS</b>	<b>ALBERTA SOUTHERN PLAINS</b>				
CAMPANIAN	84	NIOBRARA MARINE CYCLOTHEM REGRESSION	MONTANA GROUP	BEARPAW FORMATION	BEARPAW			
				OLDMAN FORMATION	OLDMAN			
				FOREMOST FORMATION	FOREMOST		Seal	
					BASAL BELLY RIVER SST		Primary Injection	
				PAKOWKI FORMATION	PAKOWKI			
				MILK RIVER FORMATION	MILK RIVER			
SANTONIAN	87	TRANSGRESSION COLORADO GRP NIOBRARA FM	FIRST WHITE SPECKS MEMBER	COLORADO		Seal		
			MEDICINE HAT MEMBER	MEDICINE HAT		Secondary Injection		

### 1.10 Data and software used

Well locations, deviation surveys, well tops, well logs, and core data from 198 wells within a 10 km radius of the main FRS onsite well 10-22-17-16W4 (10-22) were obtained. For the construction of the petrophysical model, only 88 of the 198 wells were analyzed thoroughly and are found within the TWP 17. For the well tie process, only three wells were tied to the two 3-D seismic P-P reflection volumes. A map of the FRS site, the surrounding wells, and the two 3-D seismic datasets are shown in Figure 1-7.

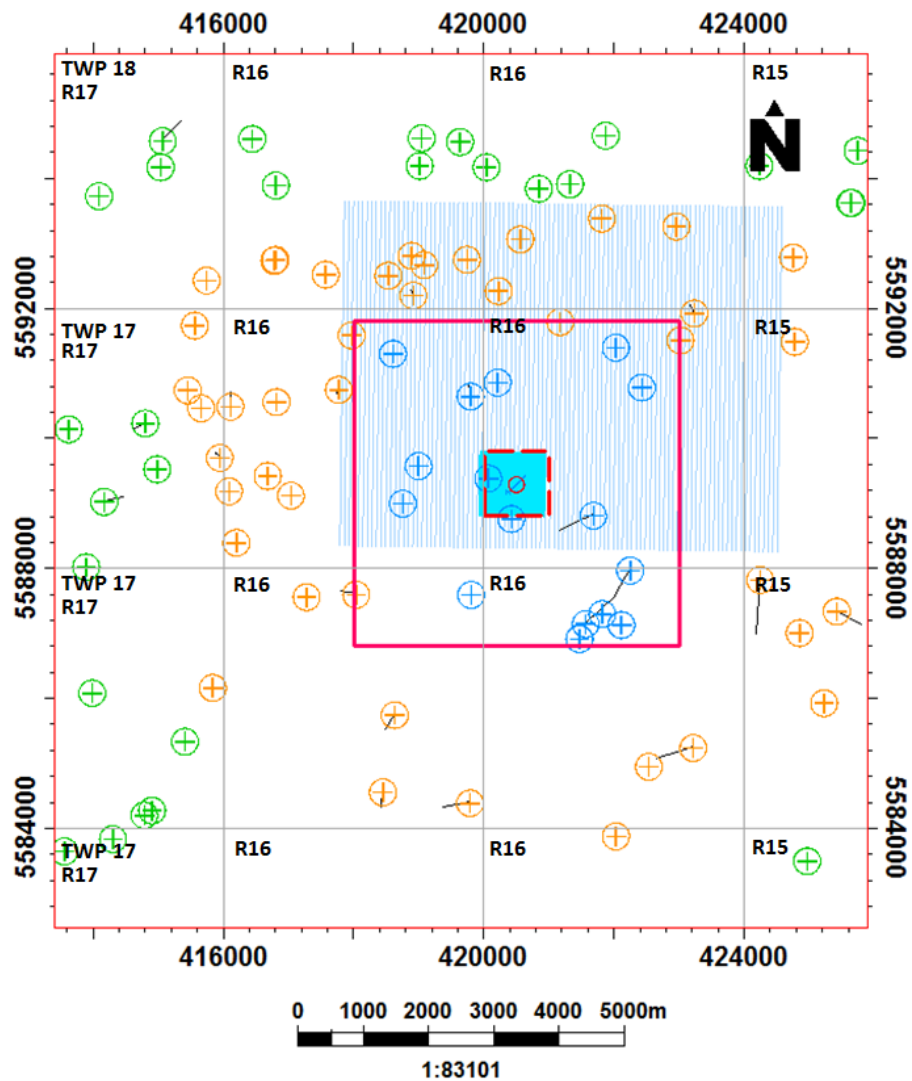


Figure 1-7. Map of data used in the FRS initial geomodel. The 88 wells analyzed in detail are displayed as crosshairs, where the 10-22 injection well is in the center of the FRS.

The green wells are located within the greater TWP 17 and 18, the orange wells are located within 10 km of the 10-22 wells, and the blue wells are located within 5 km of the 10-22 well. The static model domain is outlined by the 5 km by 5 km red polygon. The 1 km by 1 km red dotted polygon represents a localized region about the 10-22 within the 25 sq. km static model. Two 3-D seismic surveys are displayed, with the larger 30 sq. km 1997 Cenovus 3-D volume in dark blue, and the smaller 1 sq. km 2014 CMCRI 3-D volume in light blue. The R denotes the Range west of the 4<sup>th</sup> Meridian.

Two 3-D seismic P-P reflection volumes were used for interpretation of subsurface formations. A 30 sq. km 3-D/1-C volume was provided courtesy of Cenovus Energy that was collected in 1997. The newly acquired 1 sq. km 3-D/3-C seismic volume was collected in May 2014 by CMC Research Institutes. Information on both seismic surveys can be seen in Table 1-2. The newly acquired 3-D/3-C volume is located within the extent of the larger 1997 3-D/1-C volume. The 3-D datasets were re-processed into post-stack migrated seismic volumes by Dr. H. Isaac, a researcher in CREWES and CMC Research Institute groups, which were used for interpretation using Petrel™ E&P Software Platform 2015.1.

Table 1-2. Acquisition parameters of the two stacked and migrated 3-D seismic volumes.

<b>Type of Seismic Reflection Volume</b>	3-D/1-C	3-D/3-C
<b>Date</b>	1997	2014
<b>Company</b>	Cenovus Energy	CMCRI
<b>Seismic Reference Datum</b>	800 m	800 m
<b>Receiver Spacing</b>	70 m	10 m
<b>Receiver Line Spacing</b>	140 m	100 m, 50 m center
<b>Source Spacing</b>	140 m	10 m
<b>Source Line Spacing</b>	140 m	100 m, 50 m center

<b>Source</b>	Dynamite	Vibroseis
<b>Replacement Velocity</b>	2600 m/s	2600 m/s
<b>Sample Interval</b>	2 ms	2 ms
<b>Filter</b>	None	Bandpass 15/20-120/140

The IHS Energy Canada database provided the data used in the construction of the 3-D model, which was completed in Schlumberger's Petrel™ version 2015.1 licensed to the University of Calgary (Table 1-3). Information retrieved from these sources was provided access through Schlumberger Limited. The CREWES Syngram application was used to construct initial P-P synthetic seismograms from well log data. Google Maps™ 2016 was used to generate location maps. Microsoft® PowerPoint® and Word® were used to construct and edit figures and tables.

Table 1-3. A summary of the software used in the completed work for this project.

<b>Software</b>	<b>Company</b>	<b>Use</b>
Syngram	CREWES	An application to compute P-P and P-S synthetic seismograms from well log data, where logs and source wavelets can be edited.
AccuMap®	IHS Energy Canada	Data management and analysis software that enables online access to oil and gas databases for well location, production, and geological information.
Acculogs	IHS Energy Canada	A database that allows users to connect to data within Canada found in AccuMap®. Enables online access to digital LAS files, production, core data, well location and borehole deviation surveys from registered wells within the WCSB.

Petrel™ E&P	Schlumberger Canada Limited	An advanced interpretation environment that enables integration of geological and geophysical data to characterize subsurface target volumes.
-------------	--------------------------------	---

### 1.11 Thesis structure

This thesis is comprised of a total of five chapters. Chapter 1 establishes the motivation and objectives behind the research completed by reviewing the basic principles of CCS, the properties and trapping mechanisms of CO<sub>2</sub> which make CCS a successful method for decreasing the increasing GHG emissions. An overview of the monitoring techniques that are widely used for CCS MMV monitoring plans is provided. The motivation for research objectives are outlined, the location of study is introduced, as well as the software used to complete data analyses and interpretation. The regional geology and geological background of both target and seal intervals of the FRS are discussed in Chapter 2. The constructed model workflow used is discussed in detail in Chapter 3, which incorporates the geological input presented in Chapter 2. The data suites available for the development of the FRS baseline model is outlined and explained. The populated property model serves as an integrated database incorporating both the geological and geophysical data available. For geological input, qualitative and quantitative interpretation of the wireline logs were completed and discussed. Petrophysical computations of the two main properties modeled, porosity and permeability, are described in this section. For geophysical input, qualitative interpretation including the well tie process, velocity modeling, and seismic attributes are included. The 5 km by 5 km model geometry and structural definition, cell population, and statistical uncertainty are also discussed. Chapter 4 introduces the FRS model parameters and prerequisites required for fluid simulation, and discuss the initial first pass of simulation results for an injection of up to 1000 tons of CO<sub>2</sub> per year over a five year period. Chapter 5 aims to discuss the completion of baseline objectives for the FRS. Final conclusions are drawn from the completed research, potential future research, as well as the next steps for the baseline geostatic model are also reflected upon.

## Chapter Two: **Geological Background**

During Late Campanian time, Southern Alberta was located at approximately 55° N paleolatitude, in a warm, humid, temperate to subtropical climatic setting (Hamblin and Abrahamson, 1996). Shetsen (1987) mapped the surficial geology of the area and determined that the sediments of the FRS study region are composed of till of uneven thickness, with up to 30 m of locally water-sorted material. These glacial melt-out sediments are stagnation moraines, reworked by fluvial processes and further aeolian erosion leaving undulating to hummocky topography of varying till thickness defining the current topography of Newell County. The unconsolidated materials are thickest in the NW and SE areas. As the volume of clay within the glacial sediments increases, it reduces their permeability, slowing rates of groundwater recharge from precipitation and reducing infiltration of any contaminants in the area. (Worley Parsons Komex, 2008; Shetsen, 1987)

The Montana Group (Gp)/Belly River Group composed of the Bearpaw, Oldman, and Foremost formations was deposited during this time. The Oldman Formation (Fm) was deposited primarily in a transgressive environment, and is composed of two divisible parts that include the Lethbridge Member and Comrey Member (Russell and Landes, 1940; Hamblin, 1997). The Lethbridge Member consists of mudstone-dominated strata bearing carbonaceous sandstones and shales, with bentonitic beds and, near the top, the Lethbridge Coal Zone (NRCAN, 2014). The lower Comrey Member consists of lenticular fining-upward sandstone-filled fluvial channels that form an amalgamated sheet, and has a thickness of 15 m near the base (Hamblin, 1997). The fresh water deposited light-grey cross-bedded sandstones are generally weakly cemented and form the topography of the commonly known Alberta Badlands (NRCAN, 2014). The Oldman Formation overlies the Foremost Formation, acting as a secondary seal atop the primary seal interval for target A. Table 2-1 identifies the major hydrogeological units in the stratigraphic column for the Newell County region.

Table 2-1. The major hydrogeological units in the stratigraphic column for the Newell County region, modified from Worley Parsons Komex (2008).

Formation	Member	Dominant Lithology	Aquifer/Aquitard	Thickness (m)	
Overburden		Clay, Till, Silt, Sand, Gravel	Both	1-120	
	Sand, Gravel	Sand, Gravel	Aquifer	0-40	
Horseshoe Canyon		Sandstone, Siltstone, Coal	Aquifer	<80	
Bearpaw		Shale	Aquitard	<140	
Belly River Group	Oldman	Lethbridge	Mud, Coal, Sand	Aquifer	<20
		Dinosaur Park	Sandstone, Siltstone, Mudstone	Aquifer	<50
		Siltstone	Siltstone, Shale, minor Sandstone	Aquitard	<20
		Comrey	Sandstone, Siltstone	Aquifer	<20
	Foremost	Taber	Coal	Aquifer	<15
			Siltstone, Shale, some Sandstone	Aquifer	<110
		McKay	Coal	Aquifer	35
		Basal Belly River	Sandstone	Aquifer	20

## 2.1 Summary of target and seal zones A and B

The summary of the target and seal intervals are described in their respective order of deposition, and refer to their formal academic nomenclature. The intervals do not outcrop in the FRS study region, thus core from the newly drilled injection well 10-22-17-16W4 has been slabbed and photographed to display the nature of these rocks.

### 2.1.1 Medicine Hat Member

Target B is located within the Medicine Hat Member at approximately 500 m depth, below the First White Specks Member in the Colorado Group. The member consists of at least three upward-coarsening very fine-grained sandstone and siltstone

units that were deposited in a shallow marine shelf environment during the Santonian stage (Leckie et al., 1994).

These units are a heterogeneous mix of thinly bedded, very-fine to fine-grained sandstone and coarse siltstone beds (Schröder-Adams et al., 1997). They individually range from 3 – 11 m and combine to attain a total thickness of up to 60 m (Leckie et al., 1994). Coarser sand and bioclastic material are most commonly present at the top of the sand bodies, which gives each coarsening upward sandstone unit a sharp contact at the top, and a gradational base (Schröder-Adams et al., 1997). The sandstone units in Figure 2-1 are described as compositionally mature litharenites that are graded, calcareous, and mottled as a result of bioturbation and vertical burrows identified by the *Skolithos* Ichnofacies (Schröder-Adams et al., 1997).



Figure 2-1. Photo of the slabbed core interval identifying the sandstone beds within the Medicine Hat Member interval at a depth of 504 to 506 m.

As a whole, the Medicine Hat Member has been studied by Schröder-Adams et al. (1997) and Nielsen et al. (2003), who published porosity values ranging from 10 – 14%, with permeability values generally less than 1 mD. The low permeability likely corresponds to the abundant siltstone and shale intervals, whereas in a more recent study the sandstone packages have been tested to have permeability values up to 70 mD (La Croix et al., 2013).

### ***2.1.2 First White Specks Member***

The First White Specks (1WS) Member is a calcareous mudstone that overlies the Medicine Hat Member of the Niobrara Formation within the Colorado Group. In this project, the 1WS Member is referred to as the top of the Colorado Group. The deposition of the 1WS Member is the result of the maximum extension of the Interior Seaway during the Late Santonian as a part of the Niobrara Cycle (Nielsen et al., 2008).

The 1WS Member thickness ranges from 20 – 80 m, that thins eastward (Nielsen et al., 2008), and is comprised of dark gray shales that are fissile to platy in nature (Nielsen et al., 2003). The presence of thin bentonite layers (0.5 – 3 cm) (Nielsen et al., 2003) results in high uranium content linked to the organic content, and can be detected in spectral gamma ray curves (Leckie et al., 1994). The lack of bioturbation, in comparison to the overlying Milk River Formation and underlying Medicine Hat Member (Nielsen et al., 2003; Nielsen et al., 2008), describes a dysoxic environment where both low energy and low oxygen levels were present at the seafloor during the time of deposition (Nielsen et al., 2008). The abundant laminae of fecal pellets, rich in nanofossils, numerous bentonite layers, and low-angled beds depict a paleoenvironment that had a low energy regime in a low offshore to a shelf setting (Nielsen et al., 2008).

The significant volumes of clay and mud within the 1WS Member should act as an effective barrier (Figure 2-2). This will create a laterally extensive impermeable barrier (Taylor, 2011) overlying the Medicine Hat Member – a key element in providing a cap to inhibit further vertical migration of CO<sub>2</sub> from the reservoir. However, abundant clay minerals in subsurface formations can affect drilling and completion operations,

creating other challenges due to increased fluid sensitivity.



Figure 2-2. Photo of the slabbed core interval identifying the caprock seal interval of the 1WS Member at a depth of 480 to 482 m.

### ***2.1.3 Basal Belly River Sandstone Unit***

Target A is a regression shoreline sandstone deposit. It is the basal unit of the Foremost Formation, an interval of approximately 290 – 310 m depth deposited during the Late Cretaceous within the Western Canada Sedimentary Basin (WCSB) in the Montana Group (Hamblin and Abrahamson, 1996). Within Newell County, the Foremost Formation (including the Basal Belly River Sandstone unit) was measured to have a thickness of 225 m (Worley Parsons Komex, 2008).

Within the WCSB, the complete Basal Belly River Sandstone (BBRS) unit is comprised of seven stacked composite regressive cycles (Hamblin and Abrahamson,

1996) oriented N – S. The successive cycles have been interpreted to include both shoreface and channel/valley-fill depositional environments (Hamblin and Abrahamson, 1996) recording a marine to non-marine transition (Gordon, 2000). The porosity values in the shoreface sandstones generally range from 10 – 24% with 8 mD permeability, and those in related channel/valley-fills have porosity values averaging 18% with 45 mD permeability due to the larger grain sizes (Hamblin and Abrahamson, 1993). Numerous studies that include full reservoir characterization have been completed, but they are geographically limited to those specific regions within Alberta where the BBRS unit is predominantly gas bearing, with exception of the Peco Field (Twp. 47-48, Range 15-17W5) and the Pembina Field (Twp. 47-49, Range 1-10W5) where it is charged with oil (Hamblin and Abrahamson, 1996). Most producing fields are north of the FRS in the Central Plains near Edmonton (Gordon, 2000). Summaries have been provided by Shouldice (1979), Hamblin and Lee (1995), and Hamblin and Lee (1997) to organize the play types of the BBRS unit in the Plains as: (1) Cycles 1-3 that include either up-dip pinch-out features in the BBR shoreline or channel sandstones into marine shales, seen west of the 5<sup>th</sup> Meridian. (see Ferrybank, Herronton, Pembina, and Rowley fields); (2) Cycles 4-7 that demonstrate the nearly horizontal widespread BBR shoreline sandstones intertongued with marine shales in Southern Alberta and Saskatchewan, and subtly draping over the Sweetgrass Arch or the underlying Paleozoic structure (Atlee-Buffalo, Bashaw, and Provost fields) (Hamblin and Abrahamson, 1996).

The reservoir is described as a fine to medium-grained sandstone of poorly to well-sorted, angular to sub-angular grains, loosely packed with calcite cement pore-fill (Figure 2-3). Large crystals of diagenetic calcite cement make up to 40% of the rock, and diagenetic clay up to 20%. The diagenetic clay consists of kaolinite (10%), chlorite (5%), while the remaining 5% includes volumes of illite, montmorillonite, and smectite (Hamblin and Abrahamson, 1996). The sandstone permeability is affected by the abundant clay-rich horizons and discrete calcite cemented horizons that create vertical and lateral flow barriers. Drilling through the BBRS unit often damages the under-pressured sandstone with its abundant clay content. The kaolinite acts to block pore throats under high pressure fresh-water drilling systems, and acid treatments can produce

iron oxide gels from the chlorite content. (Hamblin and Abrahamson, 1996)



Figure 2-3. Photo of the slabbed core interval identifying the sandstone reservoir of the BBRs unit at a depth of 298 to 300 m.

#### ***2.1.4 Foremost Formation***

The Foremost Formation is composed of interbedded sandstone, siltstone, marine mudstones, and two coal zones – all of which represent transgressive and regressive cycles (Hamblin and Abrahamson, 1996). The Taber Coal Zone is at the top of, and the McKay Coal Zone is at the base of the formation (NRCAN, 2014). The overlying members of the Foremost Formation act as a seal to the bottom-most N – S oriented BBRs unit, located below the McKay Coal Zone (Worley Parsons Komex, 2008). For the purpose of this study, the Foremost Formation and the BBRs unit were separated to

conduct reservoir property modeling and evaluation for each (Figure 2-4).



Figure 2-4. Photo of the slabbed core interval identifying the mixture of lithology within the Foremost Formation over the depth interval of 288 to 290 m.

The complex caprock heterogeneity is displayed with facies that change from (a) marine clays with shell fragments, into (b) bioturbated mudstones, and (c) into the McKay coal zone that overlies the BBRS target A interval. The coal zone (c) did not show any cleats or visible fracture systems, and appeared intact in segments with a thickness of at least 3 cm. The other coals at shallower depths appeared more unconsolidated, and this could be attributed to the high water-saturation when at environmental conditions. The high water-saturation in the coals, alongside the adsorbed methane (CH<sub>4</sub>) gas, and low permeability (Beaton, 2003) suggests little relative permeability. Thus the coal zones and marine clays within the Foremost Formation should be capable of providing caprock integrity, and will limit vertical migration of any

injected CO<sub>2</sub> into the BBRs reservoir.

## **2.2 Hydrogeological background of Newell County, Alberta**

One of the main risks of injecting CO<sub>2</sub> into the subsurface at depths less than 1 km is leakage through nearby abandoned wells and water wells on private properties. The addition of CO<sub>2</sub> into potable water can affect the pH levels, solubility, and mobility of naturally occurring elements or compounds and potentially increase their concentration (Trautz et al., 2012). It is important to assess the static groundwater levels and the regional flow direction in order to adopt a hypothesis of how the plume will behave, by simulation preceding the injection. A regional groundwater assessment was conducted in Newell County, Alberta by Worley Parsons Komex Resources & Energy in August 2008. The data regarding static water levels, and general structure for groundwater flow, is taken from the report and provided in the FRS study.

The surface topography in the region of study is fairly flat, averaging around 770 m above sea level (asl) but steepens westward. As a rule of thumb, static groundwater levels mirror surface topography. The topographic divide forming the NE and SW boundaries of Newell County dominates the groundwater flow in the Bearpaw Formation and the Oldman Formation overburden. The divide forms the nearby drainage basins of the Red Deer River and Bow River, respectively. The regional recharge areas for groundwater have also been assessed. Of interest to this project, the local recharge area is just east of the Kitsim Reservoir and Lake Newell. The FRS region is an area of transition, but a small area of discharge just northwest of Highway 539 has been identified by Worley Parsons Komex (2008). The base of the groundwater protection is identified at the top of the Pakowki Formation, an extensive grey mudstone and siltstone that behaves as a major aquitard throughout the Newell County region. (Worley Parsons Komex, 2008)

The groundwater throughout Newell County has been characterized as brackish, containing up to 1000 – 3500 mg/L Total Dissolved Solids (TDS) (Worley Parsons Komex, 2008). Calcium hardness decreases with depth, but fluoride concentration increases to values exceeding safe drinking limits. The vulnerability of groundwater has

been determined to be low in the FRS study area as determined by the report. Much of the groundwater resources in Newell County are for agricultural use rather than domestic. Higher groundwater usage is found directly west of Lake Newell and south of the 7-22 well, measured to be less than 10 m<sup>3</sup>/day. No water wells will be directly affected by the injected CO<sub>2</sub> volume. Three nearby domestic water wells are located 5 km west and south from the main CO<sub>2</sub> injection well have a low probability of risk since groundwater flow is northward in the Foremost Formation and a discharge zone has been identified northwest of the site. A summary of subsurface formations and their respective groundwater flow can be found in Table 2-2 below. (Worley Parsons Komex, 2008)

Table 2-2. Extrapolated directional groundwater flow based on a static groundwater map (Worley Parsons Komex, 2008).

<b>Formation</b>	<b>Groundwater Flow Direction</b>
Overburden	NE, SW
Bearpaw	NE, SW
Oldman	NE
Foremost	N

## Chapter Three: **Development of the FRS Model**

### **3.1 Baseline characterization – geophysical**

#### ***3.1.1 Geophysical interpretation***

The interpretation of subsurface 3-D seismic horizons was completed after a thorough understanding of the impedance change at each reflector. The changes in acoustic impedance will affect whether the reflector is a trough or a peak. It is also important to remain consistent in identifying these in a seismic volume, as the seismic processor may or may not have changed the polarity of the data. In this data set, the SEG convention was used, where a peak can be identified as going from low to higher acoustic impedance and a trough as going from high to lower acoustic impedance values. An initial P-P synthetic seismogram was completed utilizing the compressional sonic and bulk density logs from the 7-22-17-16W4 (7-22) well in Syngam, prior to the newly drilled 10-22 well. This aided in identifying the approximate two-way time (TWT) at which the reflectors should be expected to occur in the seismic volumes. A manual comparison of a (A) 2-D seismic line (N – S) with interpretation completed by Cenovus Energy, a (B) shortened 1985 2-D seismic line (N – S) provided by Cenovus Energy, and the (C) initial P-P synthetic seismogram for the 7-22 well completed for visual verification and is shown in Figure 3-1.

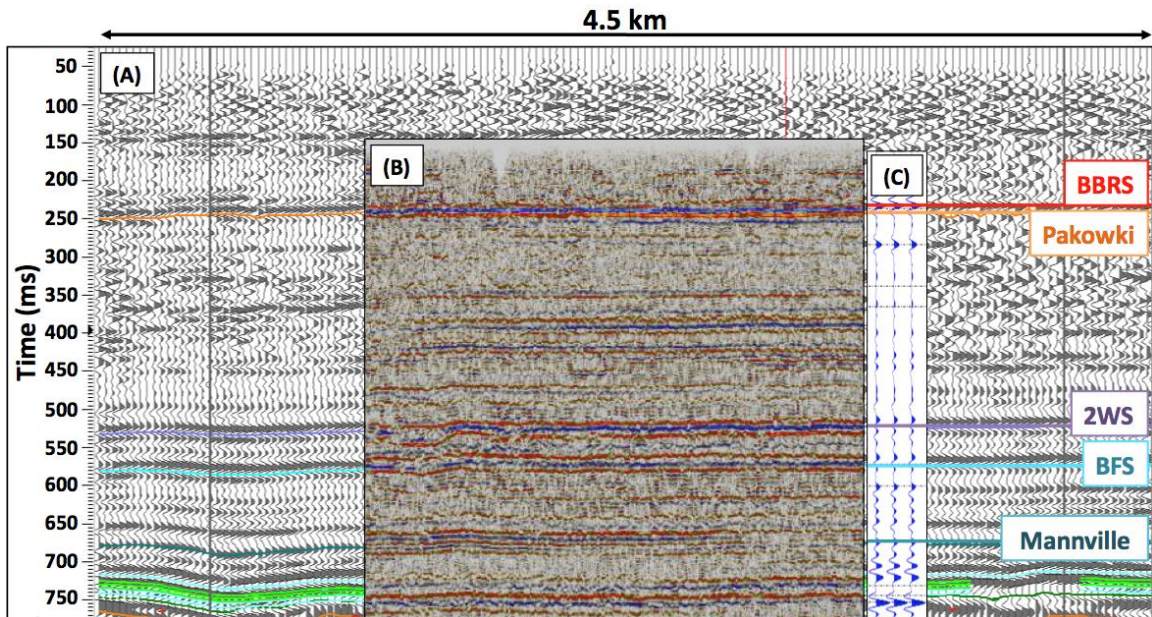


Figure 3-1. A manual overlay of (A) previously interpreted 2-D seismic line (N – S) by Cenovus Energy, (B) a shortened 1985 2-D seismic line (N-S) , and (C) the initial P-P synthetic seismogram completed on the 7-22 well.

Utilizing both the initial P-P synthetic seismogram and the manual overlay comparison as visual verification, the 2014 and 1997 seismic volumes were interpreted based on the values shown in Table 3-1. This shows whether the top of the subsurface horizon was interpreted either as a peak, trough, or zero-crossing alongside their respective approximate occurrence time in milliseconds (ms) estimated from the initial P-P synthetic seismogram of 7-22 well.

Table 3-1. Subsurface horizons correlated to the interpreted seismic reflector type and the expected approximate TWT occurrence.

Seismic Horizon	Expected Time Occurrence (ms)	Expected Reflector Type
BBRS unit	245	Peak
Pakowki Fm	250	Zero-Crossing (Z-type)
Milk River Fm	298	Peak

Colorado Gp	353	Trough
Medicine Hat Mb	373	Zero-Crossing (S-type)
Second White Specks Fm	500	Trough
Base Fish Scales Fm	560	Trough
Bow Island Fm	600	Peak
Mannville Gp	658	Peak

Subsurface reflectors were interpreted using both manual and seeded 3-D auto-tracking. The seeded 3-D auto-tracker enables an algorithm to deploy the selected reflector based on a recognition pattern and a seed confidence level. Recognition patterns can be defined as peaks, troughs, zero crossing, or none (flat). The seed confidence level determines the acceptance or rejection of a horizon expansion based on the confidence percentage assigned to the tracker to apply to the seed values (Schlumberger Ltd., 2015). It was found that using a seed confidence level of 30% was useful for strong reflectors. Depending on the lateral continuity and amplitude strength of the subsurface reflectors, manual interpretation was used in order to capture the reflector through subdued and weak amplitude regions of both the volumes. During manual interpretation, the amplitude and proximity of discontinuous reflectors was given priority. This method aided in the completion of interpretation over the span of the regional seismic volume; however difficulty was found to create artificial linear artefacts that later required removal (Figure 3-2).

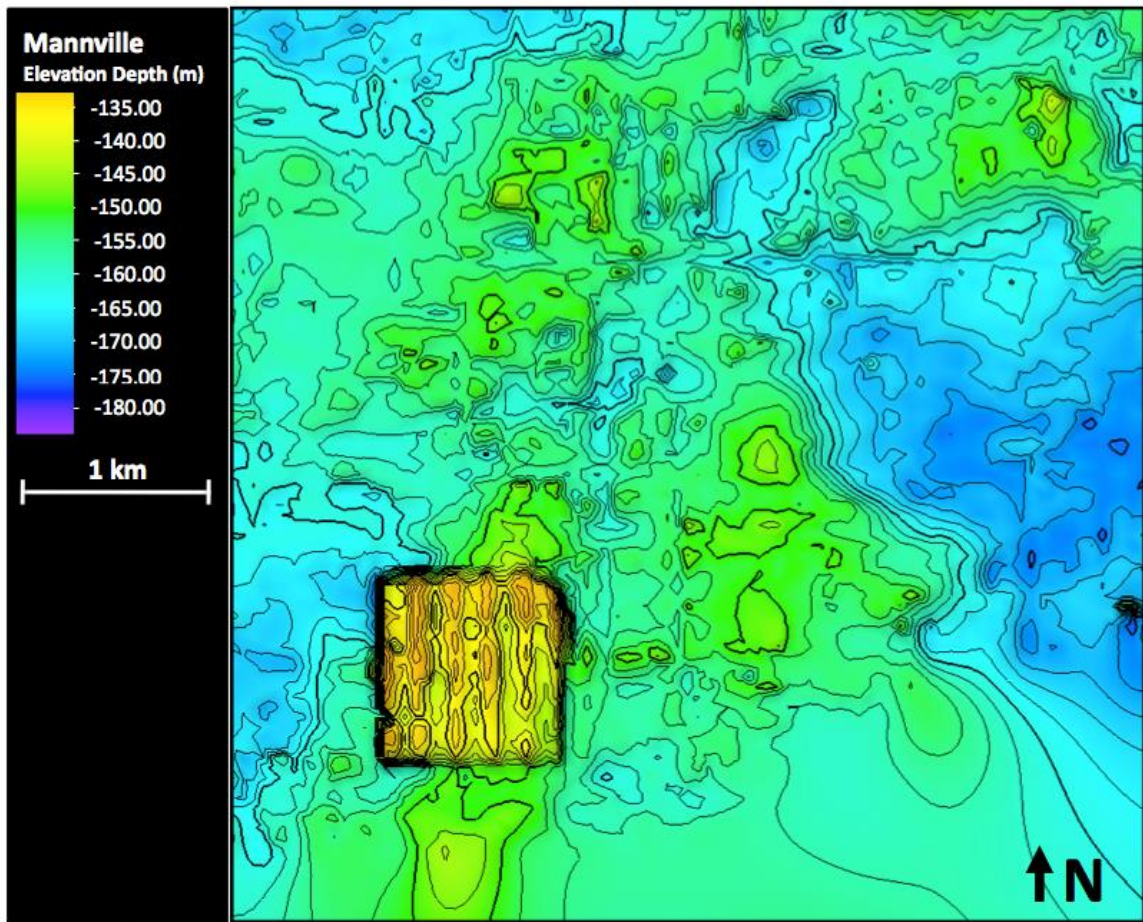


Figure 3-2. Top of the Mannville Gp depth-converted surface displaying the linear artefacts from the difference in TWT (ms) as interpreted on both the 1997 and the 2014 3-D seismic volumes. The outlined 1 km by 1 km area is the 2014 3-D seismic volume, occurring at an earlier TWT. The contoured intervals are every 2.5 m, where every bold line occurs every 5<sup>th</sup> line.

Most reflectors displayed consistent amplitude and phase over a wide area resulting in minimal manual editing. Interestingly enough, these are the horizons interpreted below 500 ms which include the top of the Second White Specks, Base Fish Scales, Bow Island formations, and the top of the Mannville Group. This could be due to the acquisition parameters of each survey, allowing for not only higher fold in the seismic volumes at greater depths but also being able to capture these formations due to their strong impedance contrasts. As well, the bulk density of formations increases with depth due to the pressure and compaction over time leading to greater contrasts of impedance. Another cause for greater impedance contrasts located at depths below the top of the

Mannville Group include lithological changes, where the deposition of carbonate rock introduces a greater bulk density value of  $2710 \text{ kg/m}^3$  (Rider and Kennedy, 2011). The two shallow exceptions to this finding include the high amplitude peak characteristic of the top of the BBRS unit, and a clear zero-crossing that follows denoting the top of the Pakowki Formation. The two subsurface horizons that presented great difficulty in seismic interpretation on both volumes include the tops of the Colorado Group and the Medicine Hat Member. One possible reason for this could be the lack of definition between the two units on the density log. Another reason for the lack of distinction could be the fact that the sandstone packages within the Medicine Hat Member appear as discontinuous lenses, with the maximum thickness of the lenses measured to be approximately 7 m. The sandstones amongst the mudstone and siltstones of the Medicine Hat Member can still be identified in the wireline logs, but are not thick enough to be resolved in the seismic volumes.

Integrating the overlapping regional and localized seismic volumes also presented difficulty, as the two did not perfectly align with each other in time. This is the combined result of different acquisition parameters, and processing workflows including stacking velocities. For two of the subsurface horizons at greater depths below the target injection intervals, it appeared that the newer seismic data set, even after the 1997 data was bulk shifted still had a difference in reflection time of approximately 1 – 5 ms. These include the horizons at the top of the Second White Specks Formation and the top of the Mannville Group. This resulted in conflicting interpretation of where the subsurface reflector was located at depth, not only giving edge effects but also placing the horizon at a greater time than what was interpreted on the 1997 3-D volume. A possible reason behind the difference in reflector location could be a difference in the phase of the data, as the 1997 volume was recorded using a dynamite source and the 2014 volume was recorded using a seismic vibrator source. As well, each 3-D seismic reflection volume encompasses different amounts of acquisition noise, along with varying processing step and techniques that also may contribute to the phase differences.

Another method that proved to produce a better result was completing two mistie corrections at two different locations within the 2014 localized volume to match the 1997

regional volume. This essentially works to minimize the difference in time at a specific cross-line and inline location, resulting in a smoother horizon interpretation on subsurface reflectors. Table 3-2 identifies the mistie pairs and what shift was applied to actively remove the interpretation imprint on the time surfaces.

Table 3-2. Mistie pairs on the 2014 and 1997 3-D seismic volumes with the associated vertical and phase correction.

<b>3-D</b>	<b>Inline #</b>	<b>Xline #</b>	<b>Vertical mistie (ms)</b>	<b>Correlation factor</b>	<b>Correction (ms)</b>	<b>Phase correction</b>
2014	65	75	-9.86	0.8321	-4.93	-133.2
1997	36	26	9.86	0.8321	3.94	132.4
2014	65	101	-2.25	0.8567	-1.12	2.3
1997	36	29	2.25	0.8567	1.12	-2.5

The mistie pairs enabled the two seismic volumes to repair the phase differences at these two locations, which overall displayed an improvement and rid interpretation edge artefacts, as well as most of the TWT differences at depth. The effects of the mistie process is shown as a before and after display in Figure 3-3, where the horizon interpretation across the two volumes at the specific inline composites are improved.

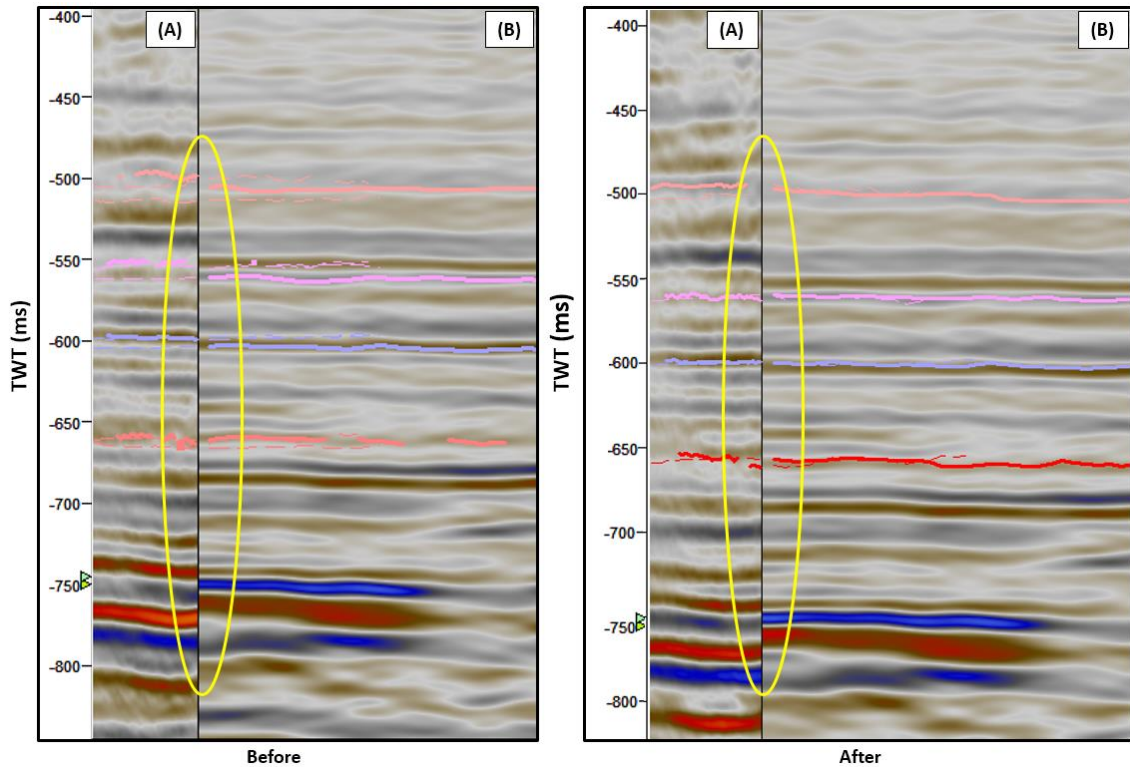


Figure 3-3. Before and after horizon interpretation as a result of the mistie process on both the (A) CMCRI 3-D and (B) Cenovus 3-D seismic volumes.

The final time surfaces included the horizon interpretation on both seismic volumes, and produced a smoother result with little to no footprint of the time differences. Minimal undulation and the lack of complex structure simplified this process, and is shown in Figure 3-4 displaying the BBRS horizon isochron map. The isochron displays a general time difference of 5 – 7 ms between the top of the BBRS unit and the top of the Pakowki Formation. Minor linear artefacts are shown as a result of subsurface horizon interpretation on the two 3-D seismic volumes. Other edge effects are shown along the east-side of the isochron map, and is caused by the lack of well control. The mistie correction served as a crucial step before completing the well ties, as each well top in depth must correspond to a similar range if not a specific time located in either seismic volume.

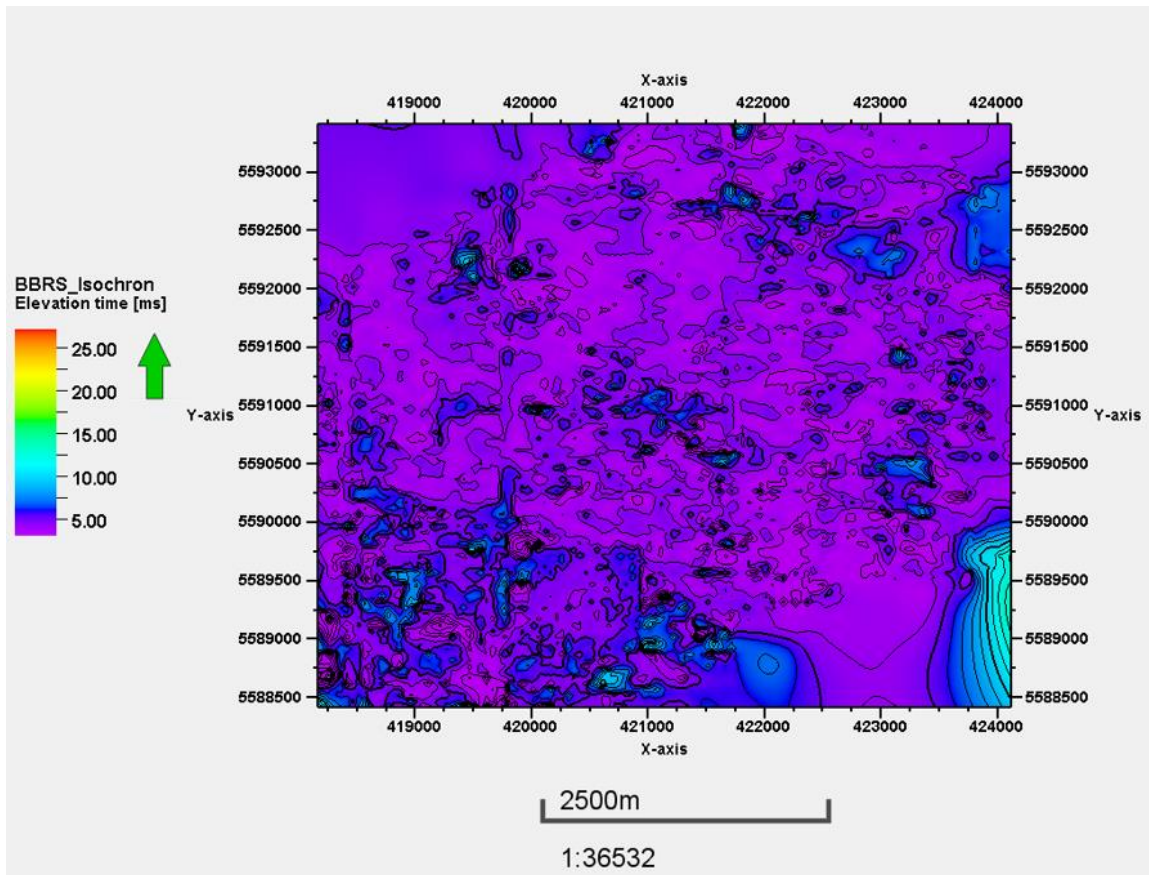


Figure 3-4. BBR5 unit isochron map displaying the interpreted TWT in both the Cenovus and CMCRI 3-D seismic volumes. The contoured intervals are every 1 ms, where every bold line occurs every 5<sup>th</sup> line.

### 3.1.2 Seismic well tie process

Integrating seismic and well data to estimate subsurface rock properties is key for reservoir modeling and is completed through a seismic well tie process, which has long remained qualitatively as an interpreter's art (Muñoz and Hale, 2012). In order to complete a well tie, four main components are required which include processed seismic data, sonic and density logs, and an estimated wavelet.

For the processed seismic data, well ties can be completed on both 2-D lines and 3-D volumes with either pre-stack or post-stack datasets. Pre-stack seismic data has more recently held a higher value for reservoir modeling, because greater detail can be extracted and used to constrain rock properties. Two elastic parameters that can be

extracted and computed from pre-stack data by the means of P-wave and S-wave velocities include Poisson's ratio and Young's modulus. These two parameters may aid with geomechanical reservoir simulations and can be compared to actual core lab measurements at depth (Sbar, 2014).

Velocity measurements can be obtained from either well or seismic data. From well data, dipole sonic logs and vertical seismic profiling (VSP) data can give both P-wave and S-wave velocities. From seismic data, these refer to the stacking velocities used to flatten the common-depth-point (CDP) gathers through the velocity analyses completed during the processing of P-P and P-S seismic volumes. This especially holds great importance in unconventional plays, where significant anisotropy and low homogeneity in lithology create difficulty in finding the targeted sweet spots. The availability of pre- and post-stack data is determined by economic feasibility and varies from project to project. Post-stack data does provide an increase in signal-to-noise ratio (SNR) and decreased data volume (Sbar, 2014), which promotes itself as appealing to geoscientists and industrial-type software.

The sonic and density logs are used to compute the impedance values of each formation with depth. An acoustic impedance (I) log is the product of velocity (v) and density ( $\rho$ ). The changes in acoustic impedance will affect whether the reflector is a trough or a peak. Equation 3.1 demonstrates the dependency of the reflection coefficients (RC) on the impedance values measured across a boundary,

$$RC = \frac{\rho_2 v_2 - \rho_1 v_1}{\rho_2 v_2 + \rho_1 v_1}, \quad (3.1)$$

where the subscript numbers 1 and 2 represent the first and second layer, respectively. The RC values represent a small portion of the energy, as approximately only 1% is reflected, thus many traces are used for stacking to enhance these reflections.

To produce the synthetic seismogram, a wavelet is required to convolve with the RC. Wavelets typically used are those for deconvolution of the seismic volume, or can be extracted from a specific well location within the seismic data. The phase of the wavelet will ultimately control the result of the synthetic seismogram. Most seismic volumes aim to produce a zero-phase data set, however phase differences amongst the wavelet and

seismic data are one of many causes for a poor seismic-to-well tie. Other causes of poor well-to-seismic match include defective wireline logs, erroneous overburden replacement velocity, hydrocarbon effects, inadequate spatial sampling, ineffective data processing workflow, residual static errors, noise, the presence of multiples in seismic data, incorrect migration velocities, as well as mis-positioning of shot/receiver locations (Bacon et al., 2007). For this model, the following data were used to complete seismic well ties:

- 1997 3-D P-P post-stack regional seismic Cenovus volume
- 2014 3-D P-P post-stack localized seismic CMCRI volume
- Compressional sonic logs
- Bulk density logs
- Extracted statistical wavelets at each 10-22, 7-22, 7-21 well location

In the Petrel software, there are two steps in completing a well tie. First is the sonic calibration, which corrects for any tool drift in measurement with depth. The wells used are those with sonic and bulk density log curves, which are required to compute the acoustic impedance and reflectivity. The qualities of both log types were substandard, and required editing as a result of cycle skipping and poor borehole conditions.

The second step involved the actual synthetic generation process, where the Time Depth Relationship (TDR) is applied to the sonic log in the well. To develop the TDR with respect to previously interpreted formation tops from well logs, either a sonic log or a check-shot survey can be used (Abbas, 2009). No check-shot data was available for this project, and so the TDR was developed using the calibrated sonic log in each well. For convolution, the wavelets were statistically extracted at the location of where the well bore penetrated the seismic volume. Each wavelet was zero-phase for the purpose of matching our approximate zero-phase processed seismic volumes. The three statistical wavelets extracted at wells 7-22 (1997 volume), 10-22 (2014 volume), and 7-21 (1997 volume) are shown in Figure 3-5, 3-6, and 3-7, respectively.

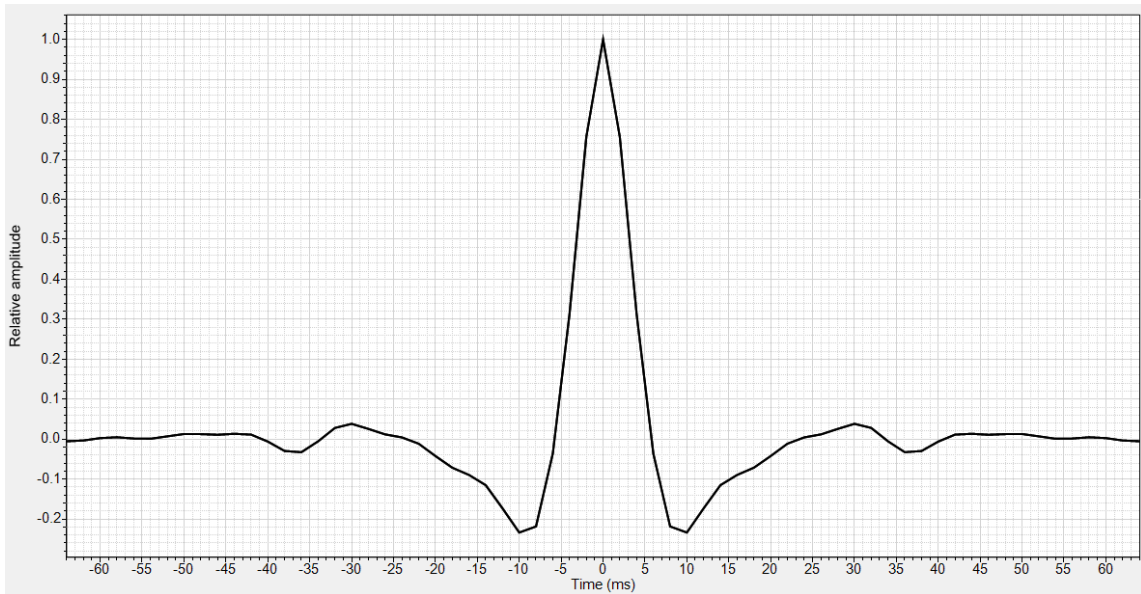


Figure 3-5. Statistical zero-phase wavelet extracted at the 7-22-17-16W4 well from the P-P Cenovus 3-D seismic volume.

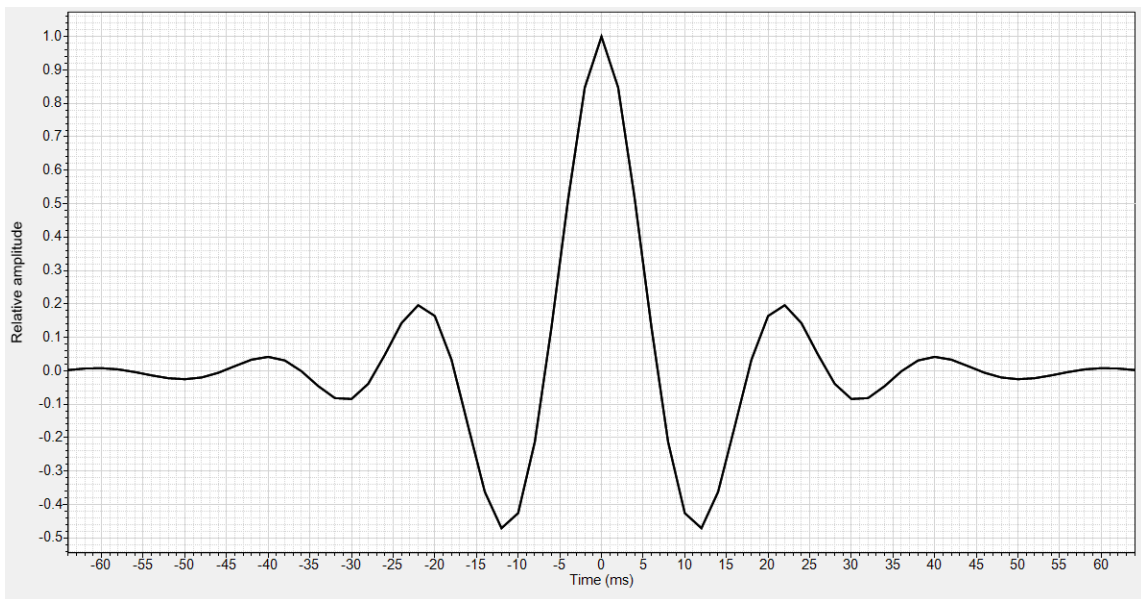


Figure 3-6. Statistical zero-phase wavelet extracted at the 10-22-17-16W4 well from the P-P CMCRI 3-D seismic volume.

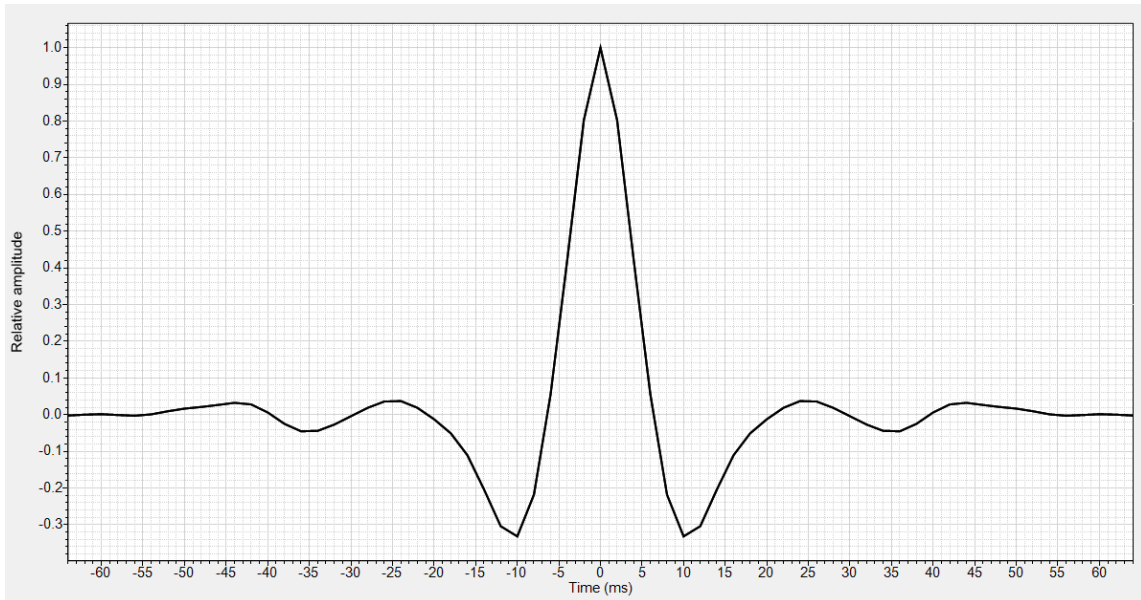


Figure 3-7. Statistical zero-phase extracted wavelet at the 7-21-17-16W4 well from the P-P Cenovus 3-D seismic volume.

Once the synthetic seismogram for each well was produced, an interpretation step was required as the wavelets used were not time-variant. No noise contributions were factored into the simple convolution matrix during the computation of the synthetic seismograms. As a result, the respective static noise-free synthetic seismograms were matched to their respective seismic volumes acquired with noise and a time-varying signal. Minor stretch-squeeze adjustments were applied to align major subsurface reflectors in the 7-22 and 7-21 synthetic seismograms with those of the seismic volume. Assigned time shifts through stretch-squeeze adjustments often are given a negative connotation, as it is essentially artificially forcing the fit of the data to match the TDR from each well. Matching reflectors through these types of adjustments may be visually pleasing, however can quickly and dramatically create erroneous interval velocities. Figure 3-8 displays a cross-sectional view of the inline 28 on the 1997 3-D seismic volume with the horizon interpretation of all subsurface formations, and tied well tops of the three vertical wells.

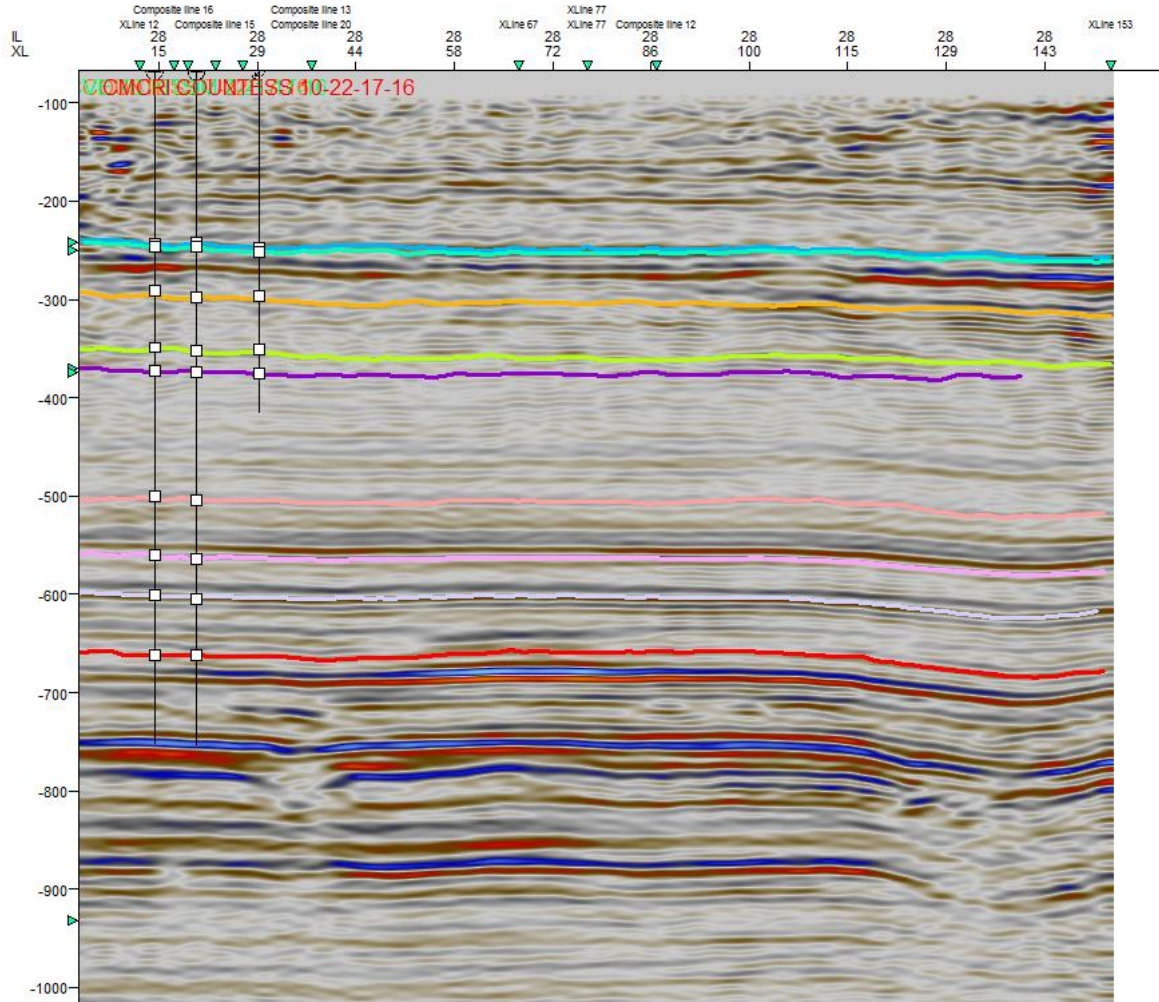


Figure 3-8. Seismic horizon interpretation completed on the 1997 3-D seismic volume, inline 28 with the three wells (7-22, 7-21, 10-22 from left) tied in depth. The white squares on each horizon represent the well tops that have been depth converted.

Two qualitative methods were used to QC the adjustments applied to each synthetic seismogram. Without checkshot or VSP data, the uncertainty or error of each TDR by the stretch-squeezing was unable to be measured quantitatively. The first qualitative method involves extracting the wavelet from the synthetic seismogram after the applied time-shifts to see how closely the extracted and convolved initial extracted wavelet match. However, this method of QC quickly proved itself as ineffective and inconclusive, as there were no apparent changes to the wavelets extracted at each of the three wells.

The second qualitative method involves exporting, analyzing, and comparing the two products of the three well ties, which include the output velocity and one-way time (OWT) with measured depth. This method proved to be comparatively useful in determining which wells experienced excessive stretch-squeeze adjustments, resulting in some high and erroneous interval velocities. The initial well tie process involved nine wells, however after analyses, all but three vertical wells were removed. The remaining three wells, two tied to the regional 1997 seismic volume and one tied to the localized 2014 volume, produced comparable output interval velocities (Figure 3-9).

The well tops marked at measured depth are those interpreted from the wireline data at the 10-22 well location. The interval velocities within each formation generally are within range of each other for each well. From 200 – 230 m depth, the output interval velocities display erroneous values, and this is interpreted as the casing effects of the initial sonic and bulk density logs. The synthetic seismograms for each well began with the first subsurface reflector tie to the top of the BBRS unit, and shallower reflectors were not interpreted or tied. The top of the Pakowki Formation required two steps of stretch-squeeze adjustments for the 7-21 well, which could be a possible reasoning behind why the interval velocity is lower than that computed for the 7-22 and 10-22 well. The 10-22 well required no stretch-squeeze adjustments, whereas one or two rounds of adjustments were completed on the 7-22 and 7-21 wells to obtain a visual for the seismic-to-well tie. The output interval velocity above the BBRS unit, as well as within the BBRS unit and top of the Pakowki horizons for the 10-22 and 7-22 appear to be within range of each other, producing similar velocities in comparison to the 7-21 (red) well. Below the Milk River Formation, the output velocities for each well have greater variability and become more dissimilar with depth as a result of the stretch-squeeze adjustments.

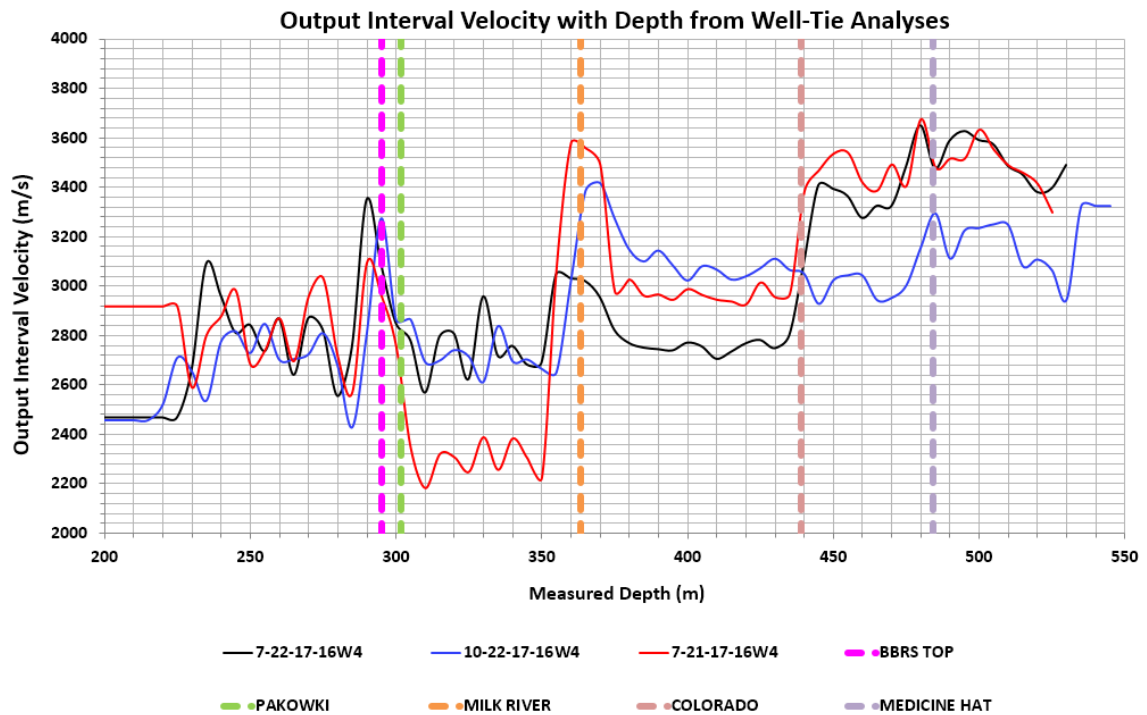


Figure 3-9. Output interval velocity at the 7-22, 10-22, and 7-21 well with depth as a product of the well tie process. The seismic horizons displayed vertically are displayed at their respective interpreted depth as completed as the formation top interpretation on the wireline data at the 10-22 well location.

A comparison of the OWT with depth demonstrates the differences of the TDR associated with each well. The TDR is an essential element in the well tie process, as this relationship is used for velocity modeling and further for seismic depth conversion.

Figure 3-10 demonstrates the similarity of TDRs across the three wells tied to the 3-D seismic volumes.

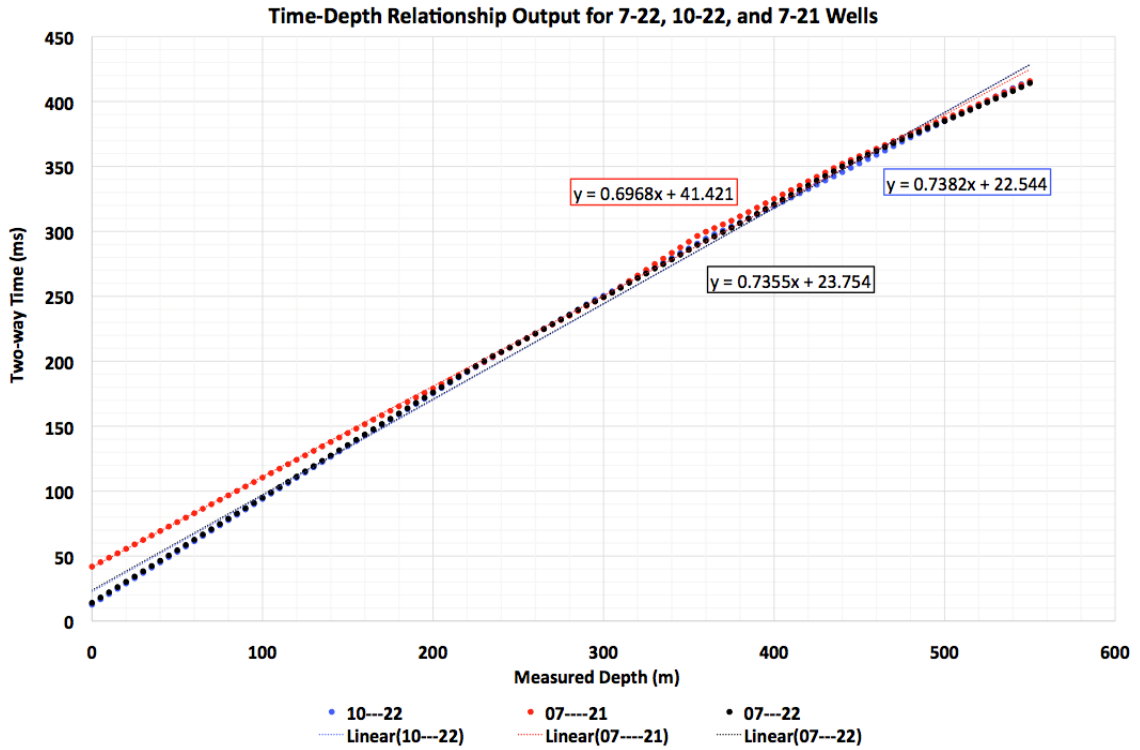


Figure 3-10. Time-Depth Relationship output as a result of the well tie process for the 7-22, 10-22, and 7-21 wells. The line of best fit for each TDR is plotted with the respective expression.

For each plotted TDR, the trendline equation was extracted and used to calculate formation velocities based on the expected depth occurrence from previous well ties and structural well top and seismic horizon interpretation. Table 3-3 displays the velocities calculated for each seismic horizon from the respective data trendline equations from the 10-22, 7-22, and 7-21 well TDRs.

Table 3-3. Comparison chart of the velocities computed from the 10-22, 7-22, 7-21 TDR trendline equations and the averaged output interval velocities from the well tie process.

Seismic Horizons	Trendline Equations Used to Calculate Interval Velocities (m/s)			Averaged Output Interval Velocities (m/s)		
	10-22	7-22	7-21	10-22	7-22	7-21
	$y=0.7382x+22.544$	$y=0.7355x+23.754$	$y=0.6968x+41.421$			
<b>BBRS unit</b>	2455	2447	2382	3068	2971	2858
<b>Pakowki Fm</b>	2460	2451	2390	2741	2790	2467
<b>Milk River Fm</b>	2499	2494	2461	3129	2792	3062
<b>1WS Mb</b>	2533	2533	2529	3042	3411	3488
<b>Medicine Hat Mb</b>	2548	2547	2553	3185	3463	3448
<b>Second White Specks Fm</b>	-	2599	2646	-	3456	3424
<b>Fish Scales Fm</b>	-	2612	2670	-	2913	3081
<b>Bow Island Fm</b>	-	2617	2679	-	2055	2062
<b>Mannville Gp</b>	-	2629	2770	-	3747	3638

In comparison to the averaged output interval velocities, the calculated interval velocities from the TDR trendline equation are generally much lower. Amongst each subset, the velocities calculated from the TDR trendline equations appear to be comparable between the three wells. Similarly, the output interval velocities computed from completion of the well tie process are comparable across the three wells and are within range of each other.

A trend of increasing velocity with depth can be seen in the velocities calculated using the TDR trendline equations for the three wells. However, the output interval velocities across the three wells do not all show the same trend. The Bow Island Formation and Fish Scales Formation show lower velocities than the formations above and below, and this is believed to be an interpretation artefact. During the well tie process, these two formation tops at depth created the most difficulty in matching the seismic reflectors in the synthetic seismogram to the corresponding seismic volumes. Thus, from the stretch-squeeze adjustments it is believed that the output interval velocities have been altered to a non-realistic value unrepresentative of the subsurface intervals. However, due to the location of the units, they are not of specific interest to the project and further critical QC methods were not applied to correct this issue.

For the purpose of velocity modeling, the output interval velocities were not used and the TDR with respect to each well was utilized for calculating the two velocity models. The two velocity models consider the seismic horizon interpretation on each volume and the depths to each subsurface unit from each seismic-to-well tie.

### ***3.1.3 Depth conversion via velocity modeling***

The interpretation of subsurface horizons on the two 3-D seismic volumes was completed in the time domain. However, reservoir characterization and modeling studies are typically completed in the depth domain. The information gained from seismic interpretation can be converted into depth through velocity modeling to then be integrated with other geological data suites, including wireline, petrophysical, and core data.

A multi-layered velocity model was computed for each seismic volume. The velocity model for the 2014 localized volume utilized the TDR produced from the 10-22 well tie, and the velocity model for the 1997 regional volume utilized the TDRs produced from the 7-22 and 7-21 well ties. Each model was run separately to calculate the interval velocities for each subsurface horizon zone down from the seismic datum of 800 m. The interval velocity ( $V_{int}$ ) in Equation 3.2 is a function of the sonic log, the TWT interpretation, and the TDR,

$$V_{int} = V = V_0 \quad (3.2)$$

where velocity ( $V$ ) and initial velocity ( $V_0$ ) are set to be a constant parameter for each layer. As stated by Etris et al. (2002), “the goal of velocity modeling is to derive a robust model that accurately predicts the true vertical velocity at and between wells”. The velocity models built for the 1997 and 2014 seismic volumes only consisted of velocity information from wireline logs. The models could however be enhanced by adding velocity information contained within the seismic data and weighted appropriately to create a broader velocity data set for critical review and QC (Etris et al., 2002). Table 3-4 and 3-5 display the velocity models for each subsurface layer with the assigned interval velocity for both the 2014 and 1997 3-D seismic volume, respectively. The velocity models are very comparable and similar when assigning interval velocities to each subsurface formation, and both show an increase of velocity with depth. Each model begins with velocities around 2470 m/s at the BBRs unit, and increase to velocities around and up to 3600 m/s at the Medicine Hat Member. Both velocity models display a low velocity dipping to 2900 m/s and lower into the 1900 m/s range for the Base Fish Scales and Bow Island Formations, respectively. These lower velocities are attributed to the stretch-squeeze adjustments, which ultimately had an effect on the TDR assigning the incorrect time for the subsurface reflectors.

Table 3-4. The velocity model produced from the three well TDR for the CMCRI 2014 3-D/3-C seismic volume.

Base		Model		
Interval	BBRS unit	$V=V_0=V_{int}$	$V_0$ : Constant (m/s)	2475
	Pakowki Fm			2477
	Milk River Fm			3191
	1WS Mb			2755
	Medicine Hat Mb			3693
	Second White Specks Fm			3467
	Fish Scales Fm			2978
	Bow Island Fm			1956
	Mannville Gp			3718

Table 3-5. The velocity model produced from the three well TDR for the 1997 Cenovus 3-D/1-C seismic volume.

Base		Model		
Interval	BRS unit	$V=V_0=V_{int}$	$V_0: \text{Constant (m/s)}$	2471
	Pakowki Fm			2477
	Milk River Fm			3145
	1WS Mb			2773
	Medicine Hat Mb			3479
	Second White Specks Fm			3484
	Fish Scales Fm			2955
	Bow Island Fm			1997
	Mannville Gp			3806

Reliable velocity models are geologically consistent (Etris et al., 2002) and take into account the lithology, stratigraphy, and depth of burial to which the compaction can affect velocity. Typical P-wave velocities for porous sandstone and shale successions saturated with water are within the range of 2000 to 3500 m/s (Bourbié and Coussy, 1987). The 1997 velocity model presents velocities that increase with depth, all within range of expected P-wave velocities in a sandstone-shale succession. Similarly, the 2014 velocity model presents velocities that also increase with depth, and again are within typical literature velocity ranges for a sand-shale succession. The only discrepancy as previously noted are the output interval velocities calculated for the Bow Island Formation. It is concluded that the erroneously low velocities are caused from the stretch-squeeze adjustments that were applied during the well tie process, and was not further investigated since it is below our target and seal reservoir characterization objective.

Both velocity models were successful in producing reasonable depth-converted seismic volumes. Upon thorough visual evaluation, the well tops interpreted in depth intersected the seismic horizon interpretation without pull up or down coning effects. The horizon interpretation completed on both seismic volumes were weighted and integrated into the model surfaces, which previously only considered well top interpretation. The weighting regime was tailored to consider a greater weight on the larger regionalized 1997 seismic volume of 70%, and 30% on the 2014 localized seismic volume. Figure 3-11 demonstrates the well tops intersecting the weighted model surfaces in the depth

domain. Utilizing the horizon interpretation completed on the two seismic volumes adds both data density to the greater FRS region and tunes finer details to the structure of the subsurface formations, which was not accessible beforehand with only wireline log interpretation.

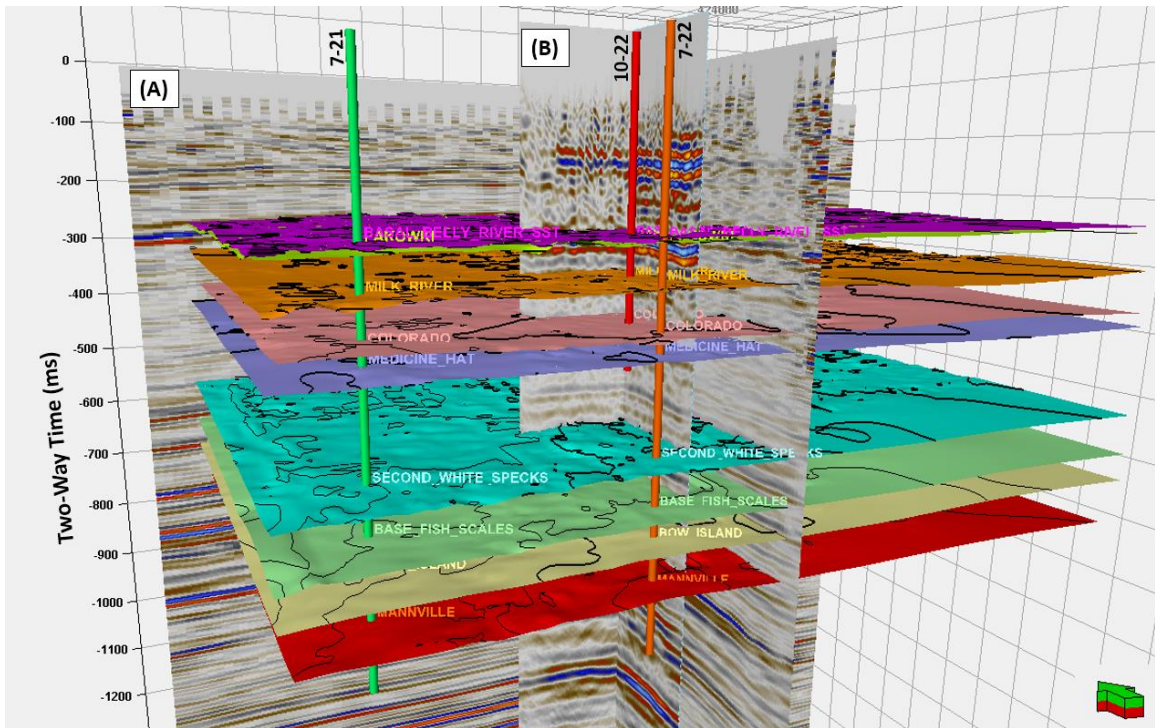


Figure 3-11. A display of the two 3-D seismic reflection volumes (A) Cenovus 1997 and (B) CMCRI 2014, with the three wells and well tops coinciding with their respective depth-converted subsurface horizons.

### 3.1.4 Seismic attributes

Another method used to extract information from the seismic data are seismic attributes. Numerous distinctive seismic attributes can be derived from raw and processed, pre- and post-stack volumes, which retrieve information from the reflection amplitudes, phase, and frequency (Barnes, 2006). Reflection amplitudes are directly related to the porosity or saturation of the formation, as the volume of pore space and liquids present affect the velocity and density of the rock. Changes in the velocity and density will ultimately affect the impedance at a subsurface boundary, where reflections

are generated. Reflection phase and frequency correspond to the geologic structure, and relative changes along a seismic reflector can highlight discontinuities and fractural trends in the subsurface. Attributes can provide both qualitative and quantitative insight on the geology of the subsurface (Anees, 2013), including but not limited to lithology, stratigraphy, depositional environments, as well as structural trends or fracture patterns (Anees, 2013).

In this project, the main objective of examining seismic attributes was to obtain additional information that may be derived from the seismic data such as depositional or fault/fracture trends that would aid in guiding the petrophysical model population. Focus was narrowed on the regional 1997 seismic volume, as the smaller localized 2014 volume was too small for visualizing any trends in the data. Time slices within 240 – 245 ms were analyzed for the target interval A, but snapshots are taken at 242 ms. As well, a comparison is completed at 694 ms to demonstrate the lack of structure in the reservoir.

Two volume and two horizon attributes were computed on the P-P 3-D seismic volume. Horizon attributes should adapt stratal slicing as a method to derive attributes from a seismic volume, because it removes structural ambiguity and sampling bias that might have occurred during seismic interpretation – remaining true to the depositional record. The stratal slicing method involves picking two subsurface horizons encompassing the target reservoir that are known to be flat-lying deposits, such as coal beds, and slices the seismic data at a specific time interval. If seismic horizon attributes are completed on simply the seismic interpretation, any underlying structural information may be missed. Stratal slicing was only completed for the spectral decomposition and semblance horizon attributes.

A total of four seismic attributes were computed, and addressed the reflection amplitude, phase, frequency, geometry, and texture of the data. The one attribute that addressed seismic reflection amplitude and texture was structural smoothing. The three other attributes that addressed the reflection phase, frequency, and geometry include semblance, ant-tracking, and spectral decomposition.

The structural smoothing attribute acts to reduce noise within the seismic data by applying a 3-D Gaussian filter. The filter itself is structurally oriented, where it calculates

the local orientation of the bedding planes within the data, thus improving the seismic signal and removing noise without removing critical information related to the geological stratigraphy. By enhancing the horizontal and vertical resolution of the seismic reflectors, horizon interpretation is made easier and also acts as a precursor filter that is often applied before computed other seismic attributes. The seismic z-slice at 242 ms shown in Figure 3-12 does not show any meaningful trends. The BBRS unit is known as a deltaic, wave-dominated shoreface deposit, and the three wells displayed were interpreted as a peak during seismic interpretation.

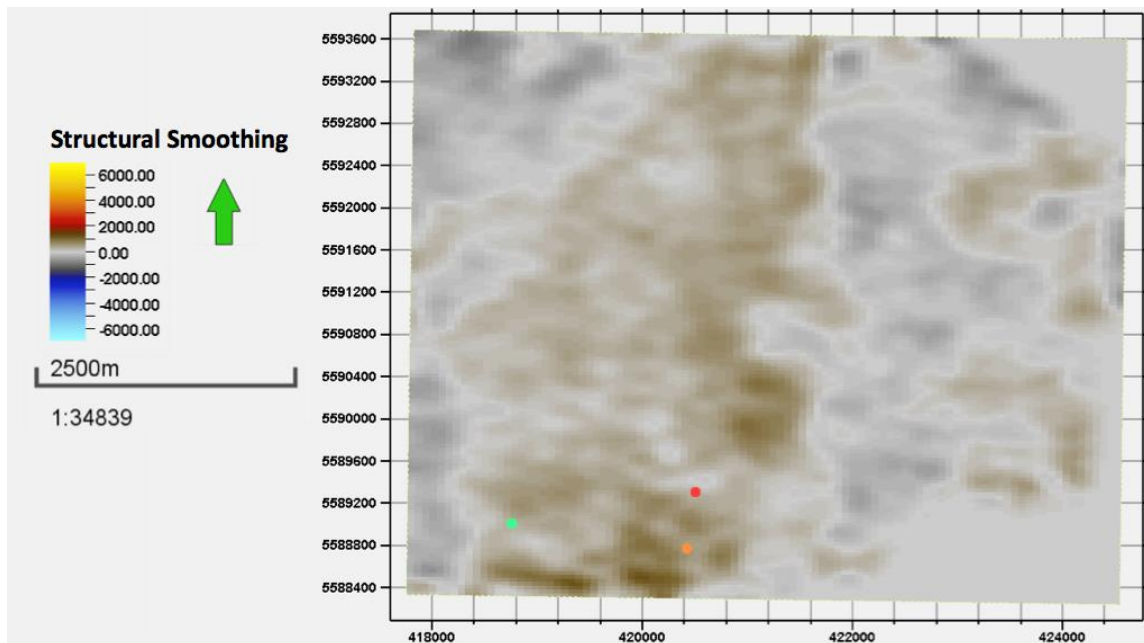


Figure 3-12. Structural smoothing z-slice in the Cenovus 1997 3-D seismic volume at 242 ms, intersection the BBRS unit interpretation. The three wells 7-21 (green), 10-22 (red), and the 7-22 (orange) are displayed in the SW corner.

Seismic coherency is a measure of continuity, identifying structural and lithological variations based on the lateral changes within the seismic responses (Marfurt et al., 1998). Coherency can be measured by a number of different seismic attributes, where semblance and variance are just two of them. Semblance comparatively measures how similar a particular seismic trace is to a group of seismic traces. The output volume contains semblance coefficient values ranging from 0 to 1, where 0 defines dissimilar

traces and 1 defines the identical case of traces. The sum of square energies within the stack of traces is divided by the sum of energies to obtain these coefficient values (Chopra, 2002). The attribute was completed in Attribute Studio, a Geomodeling software package separate to Petrel, with complimentary access provided by Abaco (2015). The user-defined window for computing semblance was a 3 ms x 3 ms window x 15 ms for the inline range, crossline range, and vertical smoothing parameters, respectively. The larger the inline and crossline filter length, the smoother the result. The vertical smoothing filter acts to enhance continuity amongst trace samples. The resulting stratal slices displayed no trend information considered useful, and Figure 3-13 displays the noisy attribute snapshot at 242 ms.

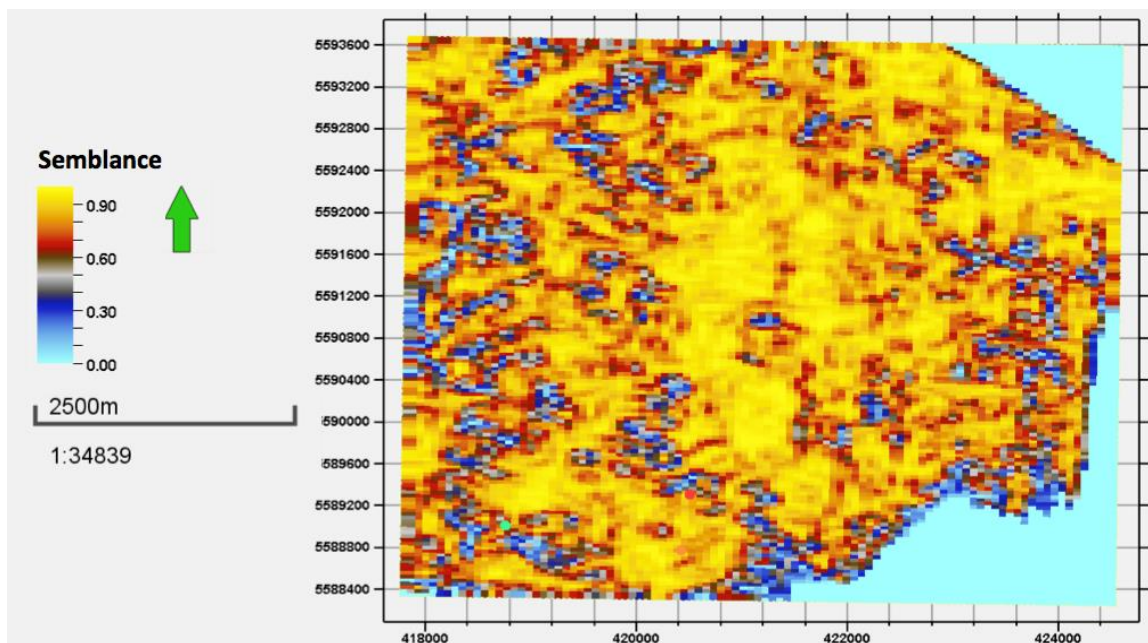


Figure 3-13. Semblance attribute map at z-slice 242 ms taken with a 3 ms x 3 ms x 15 ms filter window. The three wells 7-21 (green), 10-22 (red), and the 7-22 (orange) are displayed in the SW corner.

Ant-tracking is a seismic attribute that was created to aid with automatic fault and fracture interpretation, and is fuelled by the concept of electronic ants traveling the shortest distances from their nest to food sources. Bedding planes that do not represent faults or noise tend to be marked weakly in the ant-track volume (Chopra and Marfurt,

2007). The typical workflow for ant-tracking includes an input of a 3-D seismic volume that has been structurally smoothed to attenuate noise, then a variance volume to outline and detect linear and edge features, finally applying the ant-tracking attribute with either a passive or aggressive army of electronic ants. The difference between passive and aggressive ant-tracking is seen as the different amount of electronic ants deployed when searching the seismic volume for fault and fracture systems. Generally, the major linear features will be illuminated when deploying a passive ant-tracking attribute and both major and minor linear features will be illuminated when deploying an aggressive ant-tracking attribute. Often the aggressive ant-tracking attribute can highlight greater amounts of linear features, but these must be checked for their validity (Abaco, 2015). In part of the user-defined settings, a stereonet filter can be applied if prior knowledge of other linear system orientations should be ignored. For example, in this case the 0-180, 90-270 degree orientations were ignored to remove any seismic acquisition artefacts from the ant-tracking interpretation. From Figure 3-14, two general directions can be identified as a result of the ant tracking attribute, which include NW-SE and NE-SW. However, due to the randomness and lack of prominent orientations in the linear features shown, this attribute was declared not useful for further investigation of intra-formational fault and fracture systems. (Chopra and Marfurt, 2007; Nauriyal et al., 2010; Abaco, 2015)

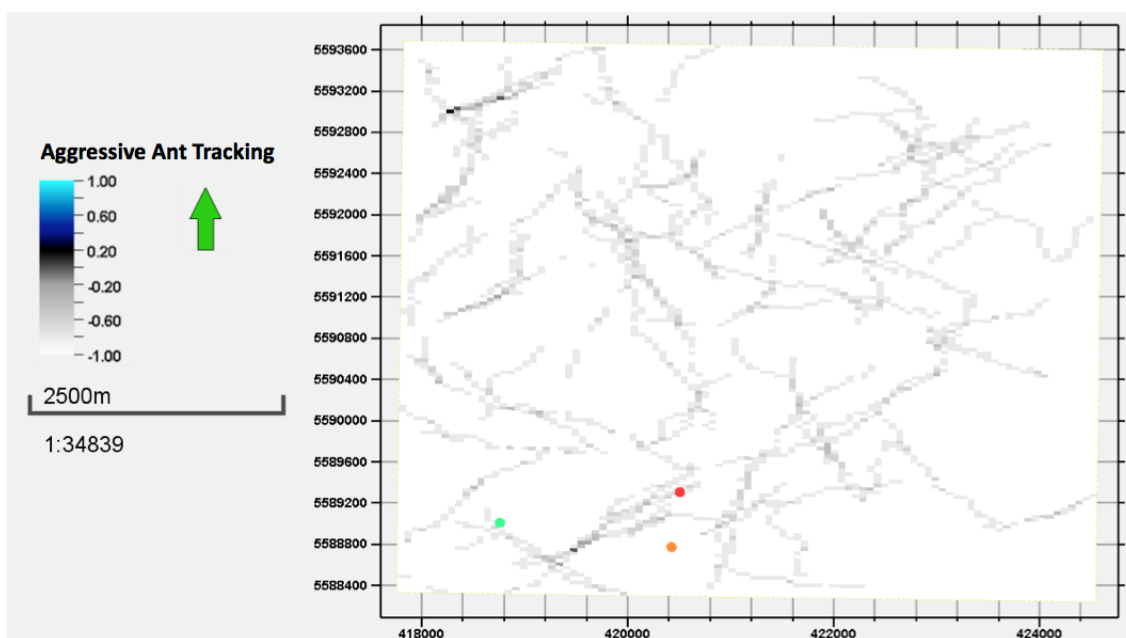


Figure 3-14. Aggressive ant tracking attribute z-slice at 242 ms. The three wells shown are 7-21 (green), 10-22 (red), and 7-22 (orange).

Spectral decomposition was the final attribute computed on the 1997 3-D seismic volume, and was one of the only attributes to find a depositional trend within a time slice of the target interval. This attribute was also completed in Attribute Studio, with complimentary access provided by Abaco (2015). Stratal slicing was used for this attribute, beginning from 230 ms down to the top of the Pakowki Formation at 250 ms. Spectral decomposition acts to transform the seismic signal from time to frequency domain into its component frequencies, by replacing a single input trace with a gather of corresponding traces (Subrahmanyam and Rao, 2008). The products are a series of volumes at specific frequency bands aiding to image where certain thin or thick beds may be most prominently resolved at a specific frequency. In this case, the depositional deltaic lobes were illuminated in yellow on the 50 – 70 Hz band volumes. This depositional feature was identified by Pederson (2016) and is shown amongst the three frequencies, but was not used in the petrophysical modeling stage (Figure 3-15 to 3-17). However, it is recommended to further investigate this by correlating the thickness of the BBRS unit with the wireline data and 3-D time slices. (Hall and Trouillot, 2004)

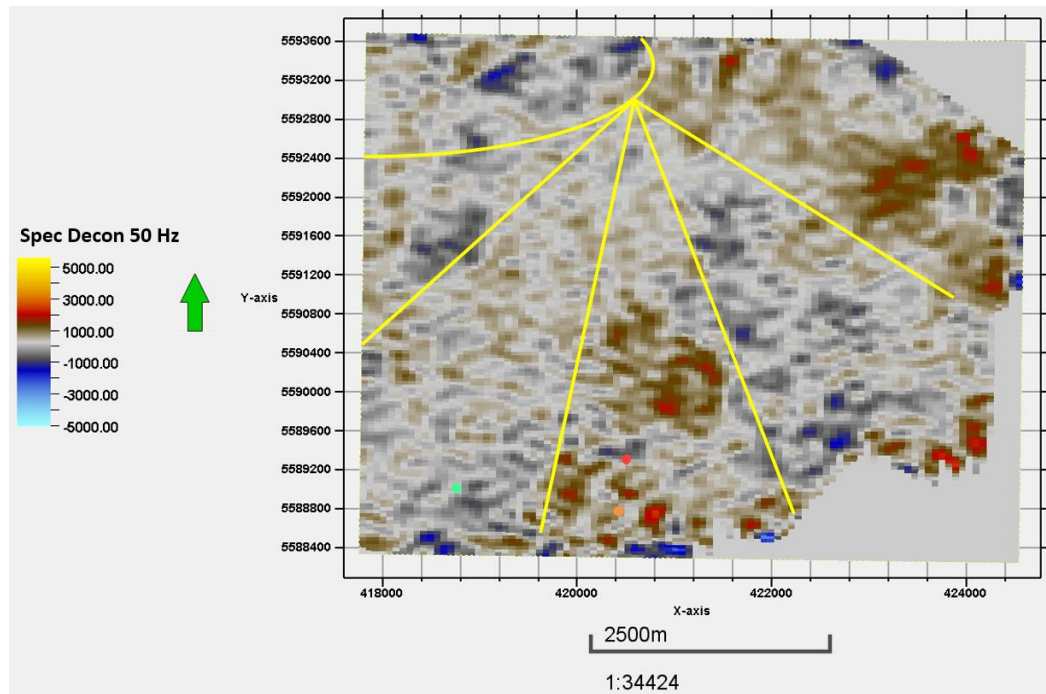


Figure 3-15. Spectral decomposition map at 50 Hz at a z-slice of 242 ms. The three wells 7-21 (green), 10-22 (red), and 7-22 (orange) are displayed in the SW corner.

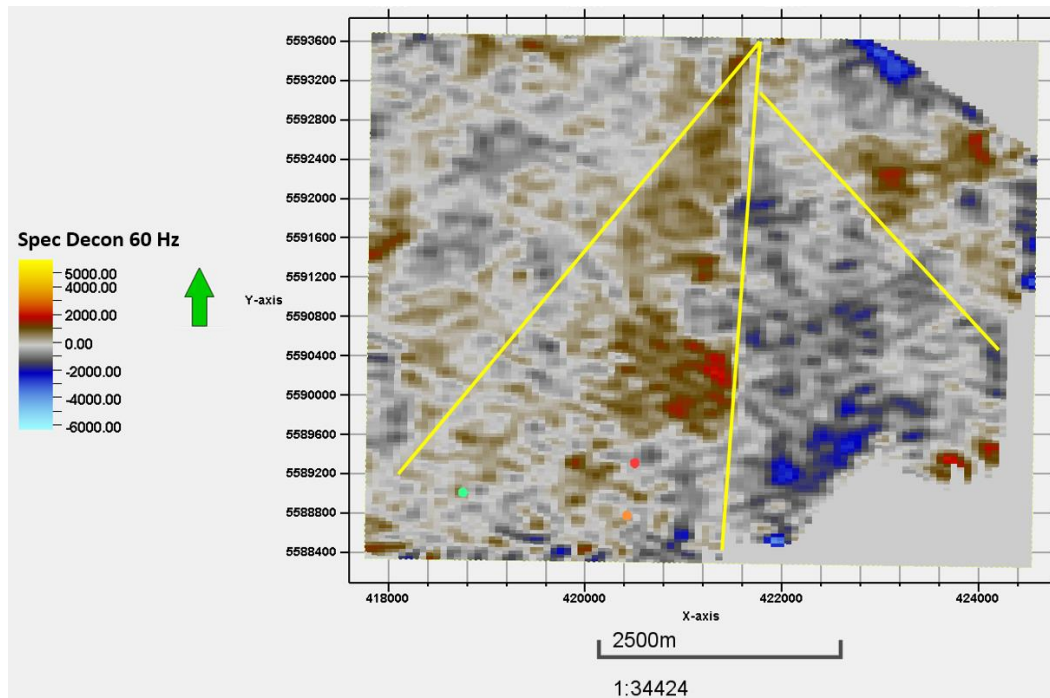


Figure 3-16. Spectral decomposition map at 60 Hz at a z-slice of 242 ms. The three wells 7-21 (green), 10-22 (red), and 7-22 (orange) are displayed in the SW corner.

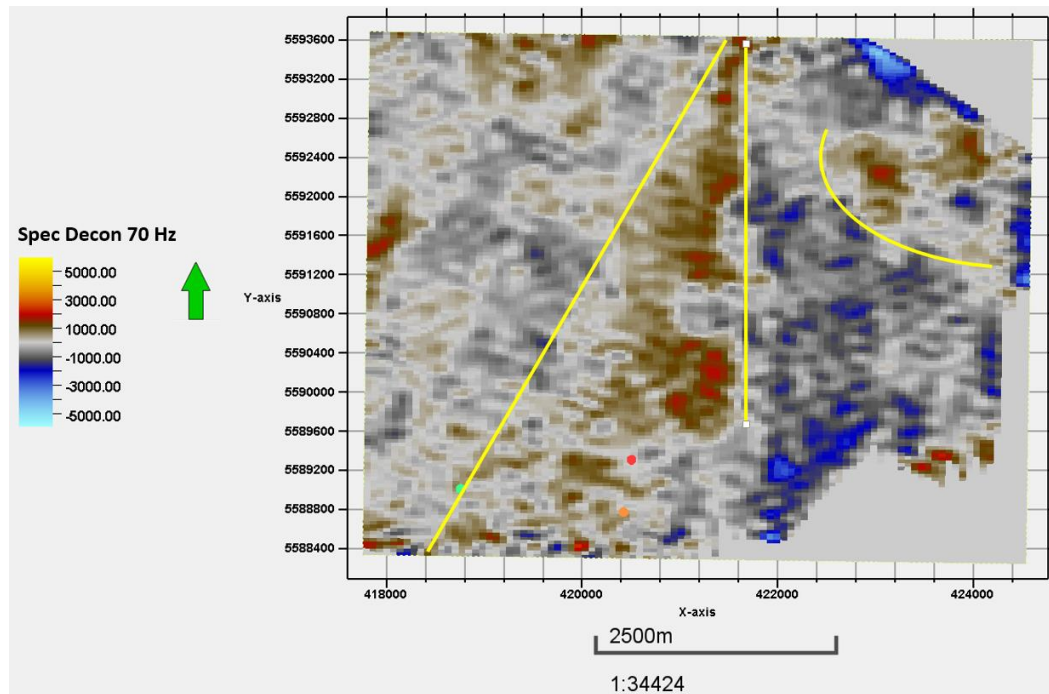


Figure 3-17. Spectral decomposition map at 70 Hz at a z-slice of 242 ms. The three wells 7-21 (green), 10-22 (red), and 7-22 (orange) are displayed in the SW corner.

In comparison to the attributes computed for target interval A at 240 – 245 ms, large depositional features that may affect facies and petrophysical modeling can be seen in the spectral decomposition map on a z-slice at 694 ms in Figure 3-18. This time slice corresponds to below the top of the Mannville Group. Had there been prominent features such as these in the target interval time slices, it could have been used as a co-kriging guide for populating the model with porosity and permeability to match the corresponding facies model.

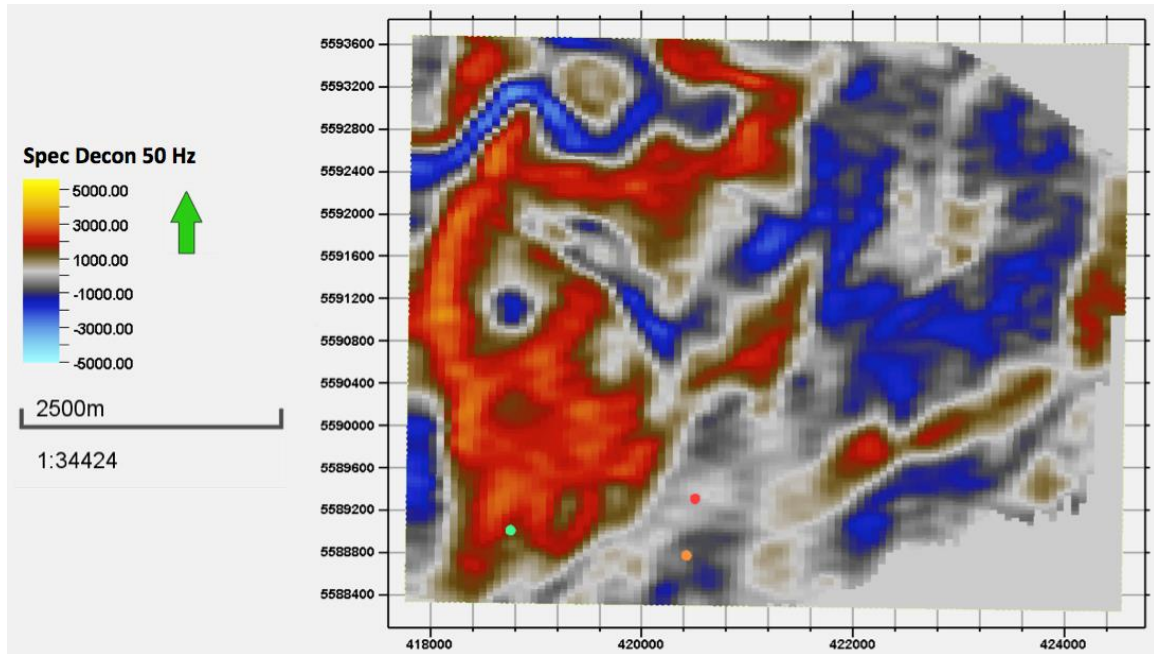


Figure 3-18. Spectral decomposition map of 50 Hz at a z-slice of 694 ms, displaying various sinusoidal structures in the NW. The three wells 7-21 (green), 10-22 (red), and 7-22 (orange) are displayed in the SW corner.

As seen in the computed seismic attributes, the lack of structure and directional trends that could have potentially aided in guiding the petrophysical model population do not exist at the target of interest. The depositional feature showing the deltaic lobes found in the spectral decomposition attribute did not correspond with any of the other attributes to enlist it of high significance (Abaco, 2015). Thus further seismic attribute work was terminated. The target and seal intervals confirm that there are no notable intra-formational micro-faults or joint systems that could lead to the presence of preferential conduit systems, thereby impacting the containment of an injected CO<sub>2</sub> volume until further proven.

### 3.2 Baseline characterization – geological

#### 3.2.1 Structural interpretation

Well top interpretation was completed on the wireline log suites available on the 88 wells in the model, where only 17 of the wells are within a 5 km radius from the main

well 10-22. The wireline data suite amongst wells generally included gamma ray, caliper, spontaneous potential, compressional sonic, shallow-deep resistivity, bulk density, density porosity, and neutron porosity logs. The interpretation on the log suite includes only formation tops, with the assumption the formation ends at the underlying formation top. A sample of the well top interpretation is demonstrated in Figure 3-19. Note that well top interpretation was completed prior to 3-D seismic volume interpretation, and thus once depth converted utilizing the well tie and velocity modeling process, both well top and seismic interpretation were integrated to form the model subsurface horizons.

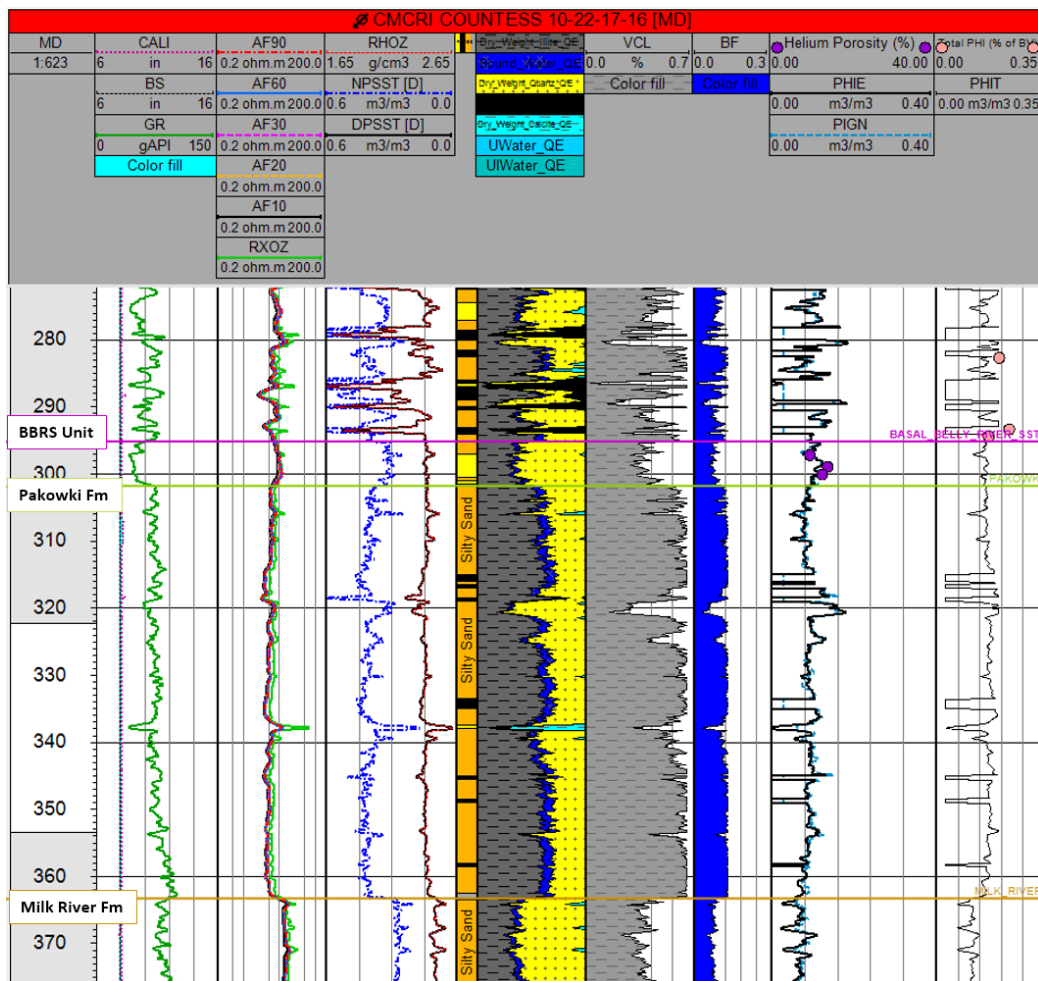


Figure 3-19. Sample well top interpretation on the 10-22 well, where the BBRs unit (pink), Pakowki Fm (green), and the Milk River Fm (orange) are shown. The last two columns show the PHIE and PHIT logs, where the core lab data is shown in purple (helium porosity) and in pink (PHIT).

Shallow wireline data above 220 m depth in all wells except the 10-22 well was unavailable or have skewed values as a result of being logged through casing. For the purpose of fluid-flow simulations, the top of formations above the BBRs unit were interpreted based on general findings of mapped bedrock geology by Shetsen (1987) and geological bedrock maps provided by Worley Parsons Komex (2008). The shallow formation tops interpreted through these findings include the Foremost, Oldman, and Bearpaw formations.

Identifying the lithology from the bulk density and gamma ray proved to be difficult. The gamma ray log in each well typically read low for the Cretaceous sediments, in that typically a textbook example of sandstone would display values less than 40 API (Rider and Kennedy, 2011). In the FRS area, sandstones were identified as 50 API or less, silty-sandstones within the range of 50 to 95 API, and values greater than 95 API were identified to be mudstones.

Furthermore, unstable borehole conditions were detected and identified by the caliper logs. The conditions appeared to not affect the compressional sonic logs, but did slightly impact the density log readings. Borehole washouts occurred within the sections with high clay or shale content, thus affecting how the padded density tool collected data in these areas (Ugborugbo and Rao, 2009). The lack of data being collected due to poor borehole wall contact resulted in low bulk density readings in some areas of the Foremost Formation. These have since been spliced and corrected for, as a result of affecting the total and effective porosity calculations that were heavily reliable on the bulk density.

Completion of formation top interpretation enabled the subsurface structure of the target and other subsurface formations to be visualized. Contoured surfaces that demonstrate the subsurface structure were generated through the interpolation of well locations with interpreted formation top depths. The surfaces are defined by elevation depth (m), with mean sea level as the datum ( $z=0$ ). Figure 3-20 displays the interval target A subsurface structural map completed through well top interpretation. The surfaces expand to fill the 5 km radius from the main FRS onsite injection well 10-22, utilizing the main interpretation completed on the 88 wells within the TWP 17. Some erratic behaviour such as surfaces crossing, pinching, or coning upward or downward was

due to given poorly interpreted system well tops. Individual attention was paid to these specific areas, and was corrected by identifying the well UWI attached to the poorly picked well top and was changed based on the available well data.

To minimize structural crossing and pinching of top/bottom surfaces, iso-points were computed between each using Equation 3.3 (Schlumberger Ltd., 2015).

$$SURFACE_B - SURFACE_A = ISOPOINTS \quad (3.3)$$

The output isopoints item of each zone give the values of minimum and maximum thickness. The maxima and minima of each formation were applied in a set of mechanical workflow equations (Zaluski, 2014) to honour the interpretation and to prevent surfaces from acting erratically. A general subset of these equations can be seen in Equations 3.4 to 3.7 (Zaluski, 2014).

$$Iso\_TopSurface = TopSurface - BottomSurface \quad (3.4)$$

$$Iso\_TopSurface = IF (TopSurface < Min\_Thickness, Min\_Thickness, Iso\_TopSurface) \quad (3.5)$$

$$BottomSurface = IF (BottomSurface > TopSurface - Min\_Thickness, TopSurface - Min\_Thickness, Thickness\_BottomSurface) \quad (3.6)$$

$$TopSurface = BottomSurface + Iso\_TopSurface \quad (3.7)$$

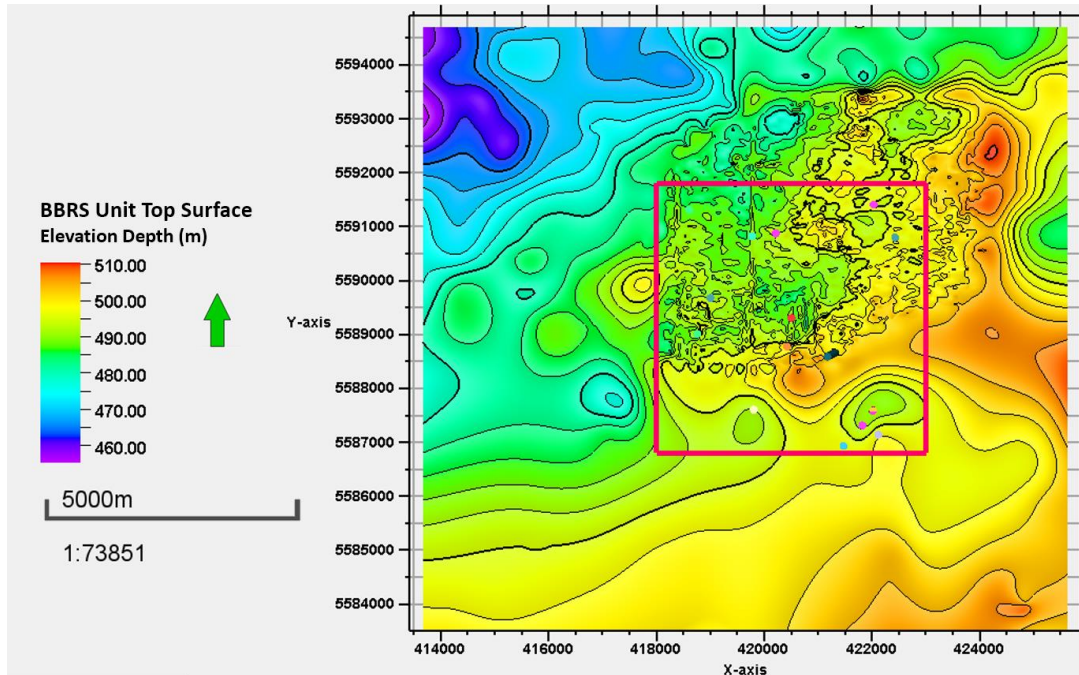


Figure 3-20. Subsurface structural map (above mean sea level) of the BBRS unit including interpretation from wireline and seismic data. The polygon represents the geomodel outline. The contours are every 3 m, every bold line occurs every 5<sup>th</sup> line.

Isopach maps were generated for the seal and target interval A units utilizing the iso-points that were generated for each zone to QC the data for the contoured surfaces. The difference in creating an isopach and a structural map is that the isopach is a map of contoured thickness for the specified zone. The Petrel interface asks for the z-thickness recalling the computed iso-points for each zone with differential ranges of maxima and minima. The structural maps are contoured as the elevation depth to which it is located in the subsurface. The isopach maps were computed in thickness (m) and can be seen in Figures 3-21 and 3-22.

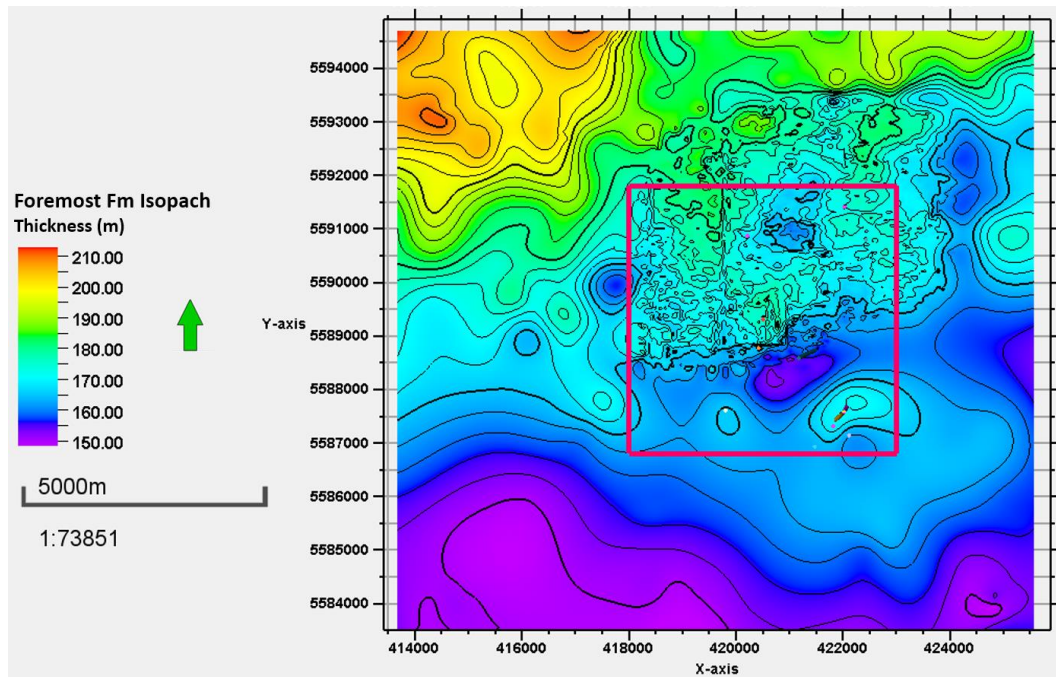


Figure 3-21. The isopach map of the Foremost Formation. The polygon outlines the 25 sq. km model region. The contours are every 3 m, every bold line occurs every 5<sup>th</sup> line.

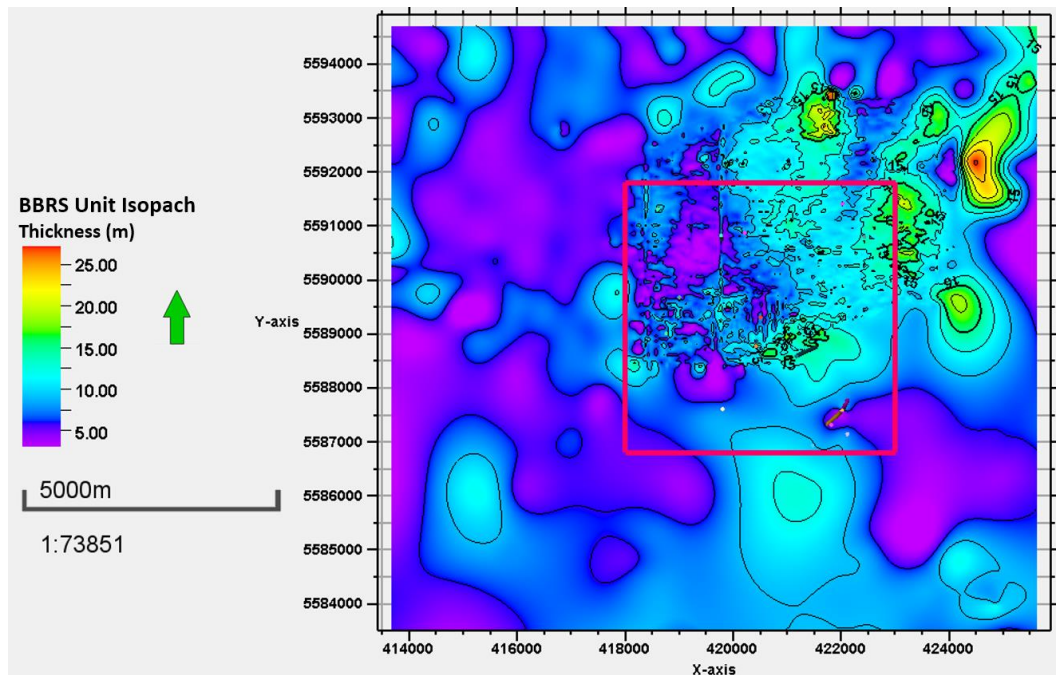


Figure 3-22. The isopach map of the BBRS unit. The polygon outlines the 25 sq. km model region. The contours are every 3 m, every bold line occurs every 5<sup>th</sup> line.

The average thicknesses of the BBRS unit and the Foremost Formation are 8 m and 167 m, respectively. The thickness maps were constructed to be greater than the model boundaries (5 km by 5 km polygon) to avoid edge effects. The maps demonstrate a general uniform thickness within the FRS area, with no pinch or cone structures at the well locations within the larger 25 sq. km area of the geomodel. Outside of the model boundary polygon, where wells do not exist, there are erroneous pinch-outs and topographic highs and lows shown by the common bulls-eye. This is caused by the lack of data control, as well data and seismic data was not present to rid of these effects and thus could not be removed. The lack of structure within the target and seal intervals is promising for executing a simple fluid-flow simulation on the geostatic model.

### ***3.2.2 Petrophysical methods***

#### **3.2.2.1 Porosity – total and effective**

Porosity and permeability are two key variables required for reservoir characterization and dynamic fluid-flow simulation. There are different definitions of effective and total porosity. Total porosity is defined as the total void space in a rock, including both interconnected and isolated pore spaces along with the volume of immobile clay bound water (Gubelin and Boyd, 1997). Effective porosity is defined as the interconnected pore spaces in a rock that enables fluid flow in a reservoir. There are two other definitions that will be used in this project when referring to effective porosity, known as PIGN and PIGE, calculated by Swager (2015) during the Elemental Log Analysis (ELAN). PIGN is defined as the total porosity without the volume of clay bound water, but includes capillary bound water. Whereas PIGE is defined as the connected pore spaces with the volume of capillary bound and clay bound water. These two effective porosity logs were computed only on the 10-22 well. (Swager, 2015)

The higher quality wireline and core data were only available for the 10-22 well, located at the center of the geostatic model. As for the remaining 87 wells, effective and total porosity were defined utilizing the minimal log suites available while remaining representative and comparable to the 10-22 data. As a result, total and effective porosity

calculations were approached in a manner that considers the clay content, as well as the bound and free fluids. The approach is outlined below and was derived by Swager (2015).

First, the clay volume ( $Volume\_Clay$ ) is scaled (Equation 3.8) using the neutron-porosity (NPSS) and density-porosity (DPSS) logs. This is to scale the amount of clay content in the stratigraphic column, as very rarely is there 60 – 70% volume of clay in any shale formation.

$$Volume\_Clay = 2.7(NPSS - DPSS) - 0.1 \quad (3.8)$$

The volume of clay (VCL) is limited to 60-70% (Equation 3.9), defining the minimum of clay content to be 2% in any given rock formation in the stratigraphic column.

$$VCL = \max(0.02, \min(0.65, Volume\_Clay)) \quad (3.9)$$

Next, the total porosity (PHIT) is calculated using the NPSS and DPSS logs (Equation 3.10). Due to the high clay content in the Cretaceous stratigraphy, the NPSS log lead to calculating erroneously high total porosities. As a result, the DPSS log was much more heavily weighted and is considered to be the most accurate and reliable log when borehole conditions are optimal (Rider and Kennedy, 2011).

$$PHIT = \left( \frac{0.1 * NPSS + 0.9 * DPSS}{1} \right) \quad (3.10)$$

The volumes of free fluid (FF) and bound fluid (BF) are required to calculate the effective porosity, as well as to compute the permeability utilizing the Timur-Coates free fluid model (Luthi, 2013), which will be discussed in the next subsection. The BF is calculated by multiplying the VCL with a scalar  $xx$  that gives  $PHIT \approx BF$  (Equation 3.11) in the zone with the highest clay content. The zone of the highest clay content was determined by the maximum separation of the DPSS and the NPSS curves. The scalar multiplier typically lies within the range of 0.15 – 0.25 (Swager, 2015), where the best match of PHIT and VXBW was with the  $xx$  equal to 0.2 in the Pakowki Formation. The BF was then limited (Equation 3.12) to be only 0.003 less than PHIT. Lastly, the FF is defined by subtracting the BF from the PHIT shown in Equation 3.13.

$$BF = xx * VCL \quad (3.11)$$

$$BF = \min(PHIT - 0.003, VXBW) \quad (3.12)$$

$$FF = PHIT - BF \quad (3.13)$$

When defined as the total pore spaces in the rock less the BF, the effective porosity (PHIE) is calculated in Equation 3.14,

$$PHIE = PHIT - BF. \quad (3.14)$$

It is typically found that the PHIE is lower than the PHIT in rock formations, as a result of not including the isolated voids and respective fluids in the calculations. However, the PHIE and PHIT both gave erroneously high values for the coal zones in the Foremost Formation, with porosities greater than 30%. The coal zones typically have a matrix density of 1200 kg/m<sup>3</sup>, which is much lower than the typical 2650 kg/m<sup>3</sup> grain density of a sandstone (Rider and Kennedy, 2011). As a consequence of this approach, facies modeling served as a method to identify, isolate, and re-assign reasonable porosity values based on numerous wireline log cut-offs.

Through observation, the PHIT values in the coal zones within the Foremost Formation exceeded 30% and appeared to be the highest porosity values in the stratigraphic column. The coal zones are known to have methane gas (CH<sub>4</sub>) and are water-saturated (Pedersen, 2014). Thus to limit the coals with the assumption of low relative permeability (Equation 3.15), it is shown that

$$PHIT = \text{if}(PHIT > 0.3, 0.03, PHIT), \quad (3.15)$$

where the coal beds are assumed to have 3% PHIT, relative to the other free and bound water and gas present in these zones.

Other lithologies that gave calculated PHIT values of 20% were deemed reasonable, but were also considered to be on the higher-end of the PHIT. Another challenge was found in some negative PHIT values, where the BF must have exceeded the PHIT in order to compute a negative value. To mitigate and limit negative and erroneously high PHIT values, Equations 3.16 and 3.17 display the syntax used,

$$PHIT = if(PHIT > 0.2, 0.2, PHIT) \quad (3.16)$$

$$PHIT = if(PHIT < 0, 0.001, PHIT) \quad (3.17)$$

where any values of PHIT greater than 20% remain at 20% and similarly any negative values of PHIT are eliminated and are re-assigned to a near-zero value.

For calculating the facies model, a simple lithology legend was used to only discriminate between coal, sandstone, silty-sand, and shale formations. Based on the limited logs available in the total 88 wells used, the lithology model cannot be complex. The characterization could be improved by careful QC of each log and repaired where possible, however this adds cost. The different facies are identified through a numerical code such that sand (0), coal (1), silty-sand (2), and shale (3) are written as their respective number in the following equations. To identify coal zones within the Foremost Formation, the bulk density (RHOB), compressional sonic (DT), NPSS, GR, and PHIT logs are used. Coal zones generally have a bulk density less than 2000 kg/m<sup>3</sup>, have characteristically higher NPSS values greater than 44%, and appear to have large transit time measurements greater than 130 μs/ft or 2345 m/s (Rider and Kennedy, 2011). If- statements were used to characterize the coals that had RHOB values less than 2000 kg/m<sup>3</sup>, NPSS values greater than 0.44, and DT values greater than 2345 m/s. The GR log was used to illuminate the shales, silty-sands, and sands for any values greater than 95 API, in between 50 – 90 API, and values less than 50 API, respectively. Where the PHIT log showed values greater than 30%, they were assigned coals and further limited down to 3%. The following Equations 3.18 to 3.25 demonstrate the identification of the coals and the other lithologies as described whilst using the facies numerical coding.

$$FACIES = if(RHOB < 2, 1, FACIES) \quad (3.18)$$

$$FACIES = if(NPSS > 0.44, 1, FACIES) \quad (3.19)$$

$$FACIES = if(FACIES = 1, 1, if(GR < 50, 0, FACIES)) \quad (3.20)$$

$$FACIES = if(FACIES = 1, 1, if(GR > 95, 3, FACIES)) \quad (3.21)$$

$$FACIES = if(FACIES = 1, 1, if(GR > 50, if(GR > 95, 2, FACIES), FACIES)) \quad (3.22)$$

$$FACIES = if(DT > 130, 1, FACIES) \quad (3.23)$$

$$FACIES = if(PHIT > 0.3, 1, FACIES) \quad (3.24)$$

$$FACIES = if(PHIT = 0.03, 1, FACIES) \quad (3.25)$$

Aside from the wireline data that have computed effective and total porosity logs, there was a total of three core measurement points in both the Foremost Formation and the BBRS unit from the 10-22 well analyzed by Schlumberger Reservoir Laboratories Canada. The Tight Rock Analysis (TRA) measured for total and effective porosity on three core samples located within the Foremost Formation. The Routine Core Analysis (RCA) measured the helium porosity on three core samples located within the BBRS unit.

The RCA method involved humidity drying the core in 40% relative humidity conditions in an oven at 60°C until the weights are stabilized. The helium porosity is measured using the CoreTest AP-608, a porosimeter-permeameter, and is based on the unsteady-state pressure fall-off method at confining pressures of 800 pounds per square inch (psi). (Schlumberger Reservoir Laboratories Canada, 2015)

The TRA method is a retort analysis of the core samples, and is performed on core biscuit samples. The porosity is calculated from a crushed portion of the core plug that is chosen to be representative of the sample. Once the chosen portion is crushed and sieved to the proper grain size, the sample is weighed and heated in a retort vessel to an initial temperature. The initial temperature stage acts to drive off the interstitial water, however once the water has been driven off, the vessel temperature is increased as a final

effort to remove any remaining fluids. (Schlumberger Reservoir Laboratories Canada, 2015)

The core measurement results from both the RCA and TRA methods can be seen in Table 3-6. The effective and total porosity values at these specific depths within the seal and target intervals were included in the porosity interpretation.

Table 3-6. Core lab measurement results from the RCA and TRA methods in the Foremost Formation and BBRS unit provided by Schlumberger Reservoir Laboratories Canada (2015).

	Sample	Depth (m)	Routine Core Analysis	Tight Rock Analysis	
			Helium Porosity (%)	Total Porosity (%)	Effective Porosity (%)
Foremost Formation	W3-1	282.65	-	20.22	11.95
	W4-1	293.34	-	23.43	12.35
	W4-2	294.37	-	16.87	10.11
BBRS unit	2	297.15	9.2	-	-
	3	298.93	13.5	-	-
	4	300.08	12.2	-	-

In comparison to the calculations completed from the wireline data for the total 88 wells, the total porosity from the TRA agreed well with the calculated PHIT log values within the Foremost Formation. Similarly, the measured effective porosity from the TRA was within range of the calculated PHIT and the PIGN log from the ELAN data within the Foremost Formation. The helium porosity from the RCA on the three cores within the BBRS unit measured very closely to the PIGN log from the ELAN data, but slightly higher than the calculated PHIE log. The calculated PHIE log had values up to 7%, which required PHIE to be recalculated with a new volume of BF. Once the core measurements

were plotted against the wireline data, the PIGN effective porosity calculated during the ELAN for 10-22 appeared to match the porosity measurements given by the core analyses. As a result, the PIGN effective porosity was set to remain as the PHIE log for the 10-22 well and the remaining 87 wells were recalculated (Equation 3.26) using a scalar multiplier  $xx$  of 0.13 (Zaluski, 2015), where

$$BF2 = xx * VCL. \quad (3.26)$$

The PHIE (Equation 3.27) was recalculated, subtracting the new bound fluid (BF2) from the original PHIT,

$$PHIE = PHIT - BF2, \quad (3.27)$$

which achieved the goal of producing a comparable log curve to the PIGN in the 10-22 well. The estimated mean effective porosity in the BBRS unit is 11%, which is comparable and within range of the helium porosity measurements. Figure 3-23 demonstrates the PIGN effective porosity plotted against the calculated PHIE and core lab measurement points in the Foremost Formation and BBRS unit. Note that this figure was captured after the PHIE log was calibrated to the core lab measurements.

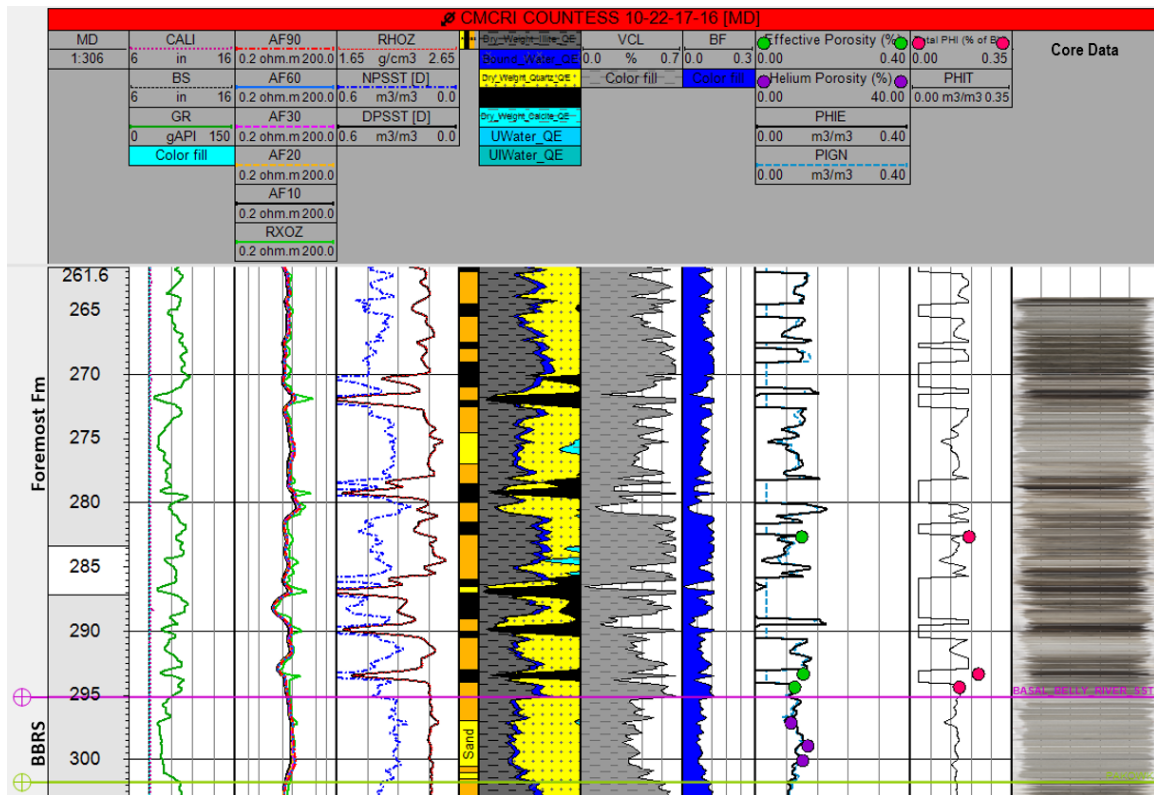


Figure 3-23. Well section window of the 10-22 well displaying the PIGN, PIGE, and the core lab measurement points within the Foremost Fm and BBRs unit. The purple dots representing the helium porosity measurements (RCA), the red dots representing the total porosity measurements (TRA), and the green dots representing the effective porosity measurements (TRA). Note that the log calibration took place before this figure was taken.

In comparison to the Peco and Pembina Fields in western Alberta where the BBRs unit is producing, the average porosity value for both fields is 8.5% (Meurant, 2011; Gardiner et al., 1990). Porosity values said to be typical of this unit range from 10 – 24%, averaging 18% in the Plains (Hamblin and Abrahamson, 1993). The calculated effective porosity values from the wireline data and the core lab measurements from the TRA and RCA analyses lie within the latter range. Gardiner et al. (1990) identified differences between the porosity measurements amongst the core and the wireline data to be attributed to authigenic clays. The authigenic clays are known to limit permeability at reservoir conditions at depth, but have the tendency to shrink whilst air-dried in the core

samples leading to overestimated porosity measurements (Gardiner et. al, 1990; Swager, 2015).

### 3.2.2.2 Permeability

Permeability ( $k$ ) as a rock property is dependent on the structural organization of individual grains such as packing, grain sorting, pore geometry, pore connectivity, as well as tortuosity. Mineralogy and grain size also affect permeability, especially when clay minerals are present. Clay minerals act to reduce permeability by clogging pore throats, where “kaolinite is less harmful than illite, which is less harmful than smectite” (Herron, 1987). Permeability is generally heterogeneous and anisotropic, and vertical permeability ( $k_v$ ) is typically lower in almost all laminated beds than horizontal permeability ( $k_h$ ).

From the wireline data available and the core lab measurements from the 10-22 well, primary intrinsic permeability was estimated on a meso to macro scale. Intrinsic permeability is defined as a function of the pore geometry, and connectivity of the pore spaces. Intrinsic permeability does not account for the movement of fluids or increased permeability attributed to fractures or faults that may act as alternative fluid pathways. The measurements from the core lab indicated secondary permeability from vertical and horizontal fractures within the core plugs, however these were not taken into consideration for modeling. For future recommendation, primary permeability, secondary permeability, as well as the vertical to horizontal relative permeability ( $k_v/k_h$ ) ratio should be incorporated into the geological model to enhance fluid-flow reservoir simulation results.

Following the free and bound fluid approach in calculating the effective porosity, intrinsic permeability ( $K_{INT}$ ) was approximated using an equation based from previous work of Timur (1968) and Coates and Dumanoir (1974). Equation 3.28 is known as the Timur-Coates free-fluid model, and calculates intrinsic permeability ( $k_{TIM}$ )

$$\kappa_{TIM} = a\phi^m \left( \frac{FFV}{BFV} \right)^n, \quad (3.28)$$

where  $\phi$  is the total porosity and involves the ratio of free-fluid volume to bound-fluid volume. The variables  $a$ ,  $m$ , and  $n$  are commonly  $10^4$ , 4, and 2, respectively (Allen et al., 2000). Utilizing Equation 3.29 with our syntax, the equation becomes

$$K\_INT = 1000(PHIT)^4 \left( \frac{FF}{BF} \right)^2, \quad (3.29)$$

where variables  $m$  and  $n$  remain at 4 and 2, respectively, and  $a$  has been modified to  $10^3$ . Due to the limited wireline data in the 87 wells, Combinable Magnetic Resonance (CMR) data was not used, however it is recommended if present to utilize CMR data to improve the porosity-permeability relationship with better FF and BF volume measurements. The K\_INT log produced reasonable values along the full stratigraphic column, however the coal zones proceeded to act erroneously with the high PHIT values. Amongst the other lithologies, it appeared that the permeability did not exceed 3 mD. To limit the coal permeability, Equation 3.30 demonstrates that if the wireline data detects a coal,

$$K\_INT = if(FACIES = 1, 0.001, K\_INT), \quad (3.30)$$

to limit the K\_INT to 0.001 mD. With the known presence of water and CH<sub>4</sub> gas, it was assumed that the relative permeability was very low but non-zero. Furthermore, where permeability values did not exist (NAN), another permeability (KINT\_GEO) was substituted. The KINT\_GEO is a permeability calculated in the ELAN dataset for the 10-22 well utilizing the Herron (1987) method. This method uses a “porosity and mineralogy model where each mineral in the ELAN model has a permeability factor” (Swager, 2015). The substitution using KINT\_GEO is seen in Equation 3.31 as

$$K\_INT = if(K\_INT = NAN, KINT\_GEO, K\_INT). \quad (3.31)$$

In addition to the porosity measurements discussed in the previous subsection, permeability was another parameter measured on the three core plugs within the Foremost Formation and BBRS unit. To recall, there were three core samples in the Foremost Formation measured for total and effective porosity using the TRA method,

and three core samples in the BBR unit measured for helium porosity using the RCA method.

The RCA method involved humidity drying the core in 40% relative humidity conditions in an oven at 60°C until the weights are stabilized (Schlumberger Reservoir Laboratories Canada, 2015). Nitrogen permeability was measured using the CoreTest AP-608 porosimeter-permeameter. The unsteady-state pressure fall-off method was used and set at a confining pressure of 800 psi or 5.52 MPa, identical to the measurement process of collecting the helium porosity data. The core sample is then exposed to a high-pressure nitrogen gas (N<sub>2</sub>) source released upstream, and the sample is monitored as the N<sub>2</sub> gas flows through the sample. The rate at which the pressure flowing through the sample reaches equilibrium with the downstream pressure is used to determine permeability (Nolen-Hoeksema, 2014). Nitrogen gas is generally preferred than air or helium (He) because it is an inert gas. Permeability that takes into account the Klinkenberg effect is known as the Klinkenberg permeability. The Klinkenberg effect is due to the slip flow of gas that occurs at the pore walls, and acts to enhance the gas flow rate when the pore sizes are very small due to the greater larger surface area available (Tanikawa and Shimamoto, 2006). Typically, gas permeability is larger than water permeability, and water permeability can be calculated from gas permeability provided the Klinkenberg correction is applied (Tanikawa and Shimamoto, 2006). Nitrogen gas is also chosen when measuring Klinkenberg permeability, because the gas slippage is less pronounced in comparison to Helium and air (Rushing et al., 2004). The measurements are quality controlled by using a check plug made of stainless steel of known permeability similar to the core plug permeability, and is checked every fifth core plug. (Schlumberger Reservoir Laboratories Canada, 2015)

The TRA method measured the pressure-decay matrix permeability on a specific weight fraction of the crushed and sieved sample at saturation conditions. Saturation conditions of a core plug are determined prior to further core analyses. The pressure-decay permeability is then defined as the permeability to gas, and is derived from data collected from a gas expansion measurement. This method suggests by crushing the core sample, it removes artefacts from the rock and provides greater access to pore spaces to

provide greater data accuracy – especially in mudstones and shales. (Schlumberger Reservoir Laboratories Canada, 2015)

The core measurement results from both the RCA and TRA methods can be seen in Table 3-7. The intrinsic permeability values at these specific depths within the seal and target intervals were included in the permeability interpretation.

Table 3-7. Core measurement results from the RCA and TRA methods in the Foremost Formation and BBRS unit provided by Schlumberger Reservoir Laboratories Canada (2015).

	Sample	Depth (m)	Routine Core Analysis		Tight Rock Analysis
			Nitrogen $k$ (mD)	Klinkenberg $k$ (mD)	Pressure-Decay $k$ (mD)
Foremost Formation	W3-1	282.65	-	-	0.000061
	W4-1	293.34	-	-	0.000150
	W4-2	294.37	-	-	0.000038
BBRS unit	2	297.15	0.466	0.365	-
	3	298.93	0.390	0.183	-
	4	300.08	1.21	0.738	-

From the TRA method, Sample W4-2 was interpreted to have too high of permeability to be accurately measured by the pressure-decay method. This sample was concluded to have reasonable total and effective porosities measured with this method, however the very low permeability suggests that the core sample has higher complexity that is beyond this method of measurement. Samples W3-1 and W4-1 also present very low permeabilities, much lower than values calculated in the K\_INT log. The samples used in the TRA method are crushed to rid of micro-fractures, however no other method of measurement was completed on these core samples for comparison. As a result, the measured core permeability in the Foremost Formation was not used to calibrate the calculated K\_INT log due to the scaling of this project, but shows promise in providing a

tight caprock interval with very low permeability overlying the BBRS unit. The nitrogen and Klinkenberg permeabilities were performed on the three core samples within the BBRS unit. No fractures were noted on the six core measurements in the target interval. Both the nitrogen and Klinkenberg permeabilities measured higher than the calculated K\_INT log. Thus, the six core measurements within the BBRS unit were used to obtain a best fit for the K\_INT log, and attempt to reach within an order of magnitude of the TRA permeability measurements (Swager, 2015).

The majority of the calculated permeability readings over the full stratigraphic column in the 10-22 well are less than 3 mD, other than the coal zones in the Foremost Formation which were re-assigned to 0.001 mD. From the core lab analyses, the permeability results from all core measurement locations are observed to generally occur below 1 mD. In order to honour the core lab analyses and scale back the estimated K\_INT log, Equation 3.32 was used,

$$K\_INT = \text{if}(K\_INT > 3, 3, K\_INT), \quad (3.32)$$

where any values greater than 3 mD are set to remain at 3 mD. As well, any estimated K\_INT values greater than 1 mD were scaled down by a factor of 0.25 (Equation 3.33),

$$K\_INT = \text{if}(K\_INT > 1, K\_INT * 0.25, K\_INT), \quad (3.33)$$

in order to have the K\_INT log tracing over the plotted core points in the 10-22 well. The mean estimated intrinsic permeability in the BBRS unit is 0.57 mD, which is comparable and within range of the core lab measurements. The calcite cement matrix in the BBRS unit appears to be limiting the primary intrinsic permeability, which could possibly contribute to the lower range of estimated permeability. Figure 3-24 displays the well section window of the 10-22 well with the Timur-Coates calculated permeability, the KINT\_GEO permeability log from the ELAN dataset, as well as the six core measurements superimposed on the well logs. Note that this figure was captured after the K\_INT was calibrated to the core lab measurements.

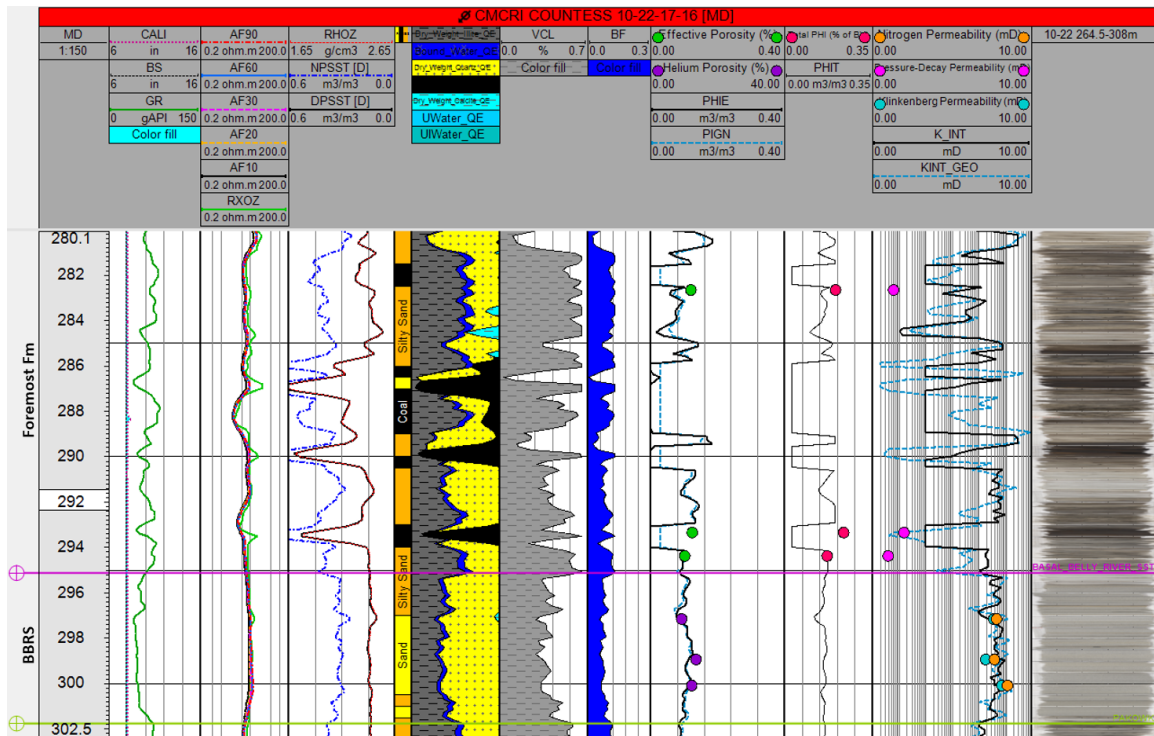


Figure 3-24. Well section window of the 10-22 well displaying the permeability in both the Foremost Fm and BBRs unit calculated using the Timur-Coates equation, the KINT\_GEO permeability from the ELAN dataset, as well as the plotted core lab measurements. The nitrogen (orange), pressure-decay (pink), and Klinkenberg (blue) permeability points are superimposed over the calculated well logs. Note that the log calibration took place before this figure was taken.

It is known that these Late Cretaceous sediments in eastern Alberta have not been buried to a great depth, and many of them remain unconsolidated with high pore-water volumes (Pedersen, 2014). The presence of the coal zones in the Foremost Formation demonstrated challenges while estimating the effective porosity and intrinsic permeability. Caution was taken through the re-assignment of lower total porosity and intrinsic permeability values, as less dense coals can be very porous but can act as impermeable barriers limiting vertical mobility of pore fluids and gases. Coal permeability is often determined by cleats, which are sets of joints that are perpendicular to the top and bottom of the coal seam where two sets of cleats develop an orthogonal pattern (Thomas, 2002). Cleats are natural fractures in coals, and act as conduits for the flow of fluids and gases. Numerical information of the coal zones within the Foremost

Formation are not available at present in the public domain (Beaton, 2003), but through observation of the core samples in the 10-22 well, the coals did not demonstrate any fractures or cleat networks. Aside from coal zones, the three core measurements from the TRA method demonstrated very low permeabilities which supply evidence that the Foremost Formation is capable of providing a tight seal as a caprock interval. The core measurements from within the BBRS unit demonstrate a semi-pervious reservoir interval, and suggests the lower permeability values may result in lower injectivity rates to avoid over-pressuring and fracturing the unit.

As a general rule, increasing effective porosity typically have higher permeability. Figure 3-25 shows this trend from the estimated effective porosity and intrinsic permeability in the BBRS unit. The cross-plot demonstrates increasing K\_INT with increasing PHIE, which is generally true in clastic sediments, however secondary porosity can occur at depth with increasing temperatures due to the geothermal gradient. The range of corresponding K\_INT and PHIE values displayed on the cross-plot demonstrates the model is honouring both wireline and core data inputs. The previous wireline conditioning where facies cut-offs were assigned appears to have successfully eliminated extreme outliers in the data. With access to a greater number of wells with core lab measurements, the PHIE – K\_INT relationship could be further refined.

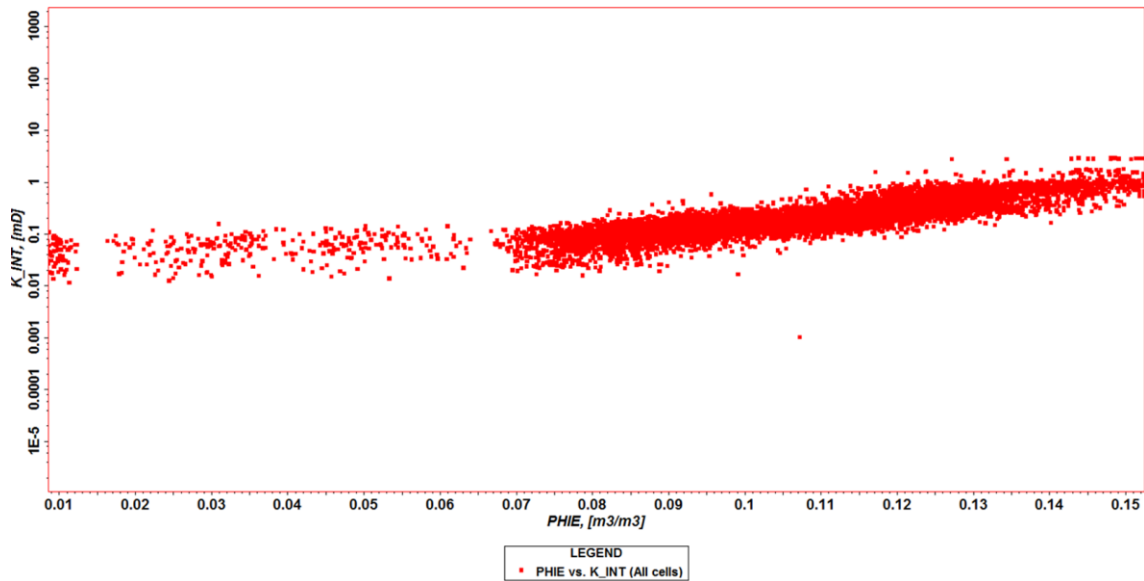


Figure 3-25. The relationship between the calculated effective porosity and intrinsic permeability for the BBRs unit.

From other oil and gas producing fields located within Alberta, the shoreface-related sandstone typical of the BBRs unit is known to have an average of 8 mD in the Plains (Hamblin and Abrahamson, 1993). Looking at specific fields such as the Pembina Field, the BBRs unit has been described to have fair permeability ranging from 1 – 15 mD (Meurant, 2011). Although, this is not a great analog to compare with as the BBRs unit in the Pembina Field has a different burial history than that in the Newell County area. Another study (Gardiner et al., 1990) plotted 47 core points of porosity and permeability, fitting a least-squares-fit straight line that indicated a core porosity of 8.5% to have permeability of 1 mD. In comparison to these producing fields, the porosity – permeability relationship leans towards the lower-end of fair to low permeability. This and the lack of hydrocarbons present is most likely the reason why the BBRs unit is not producing in this study area.

### 3.2.2.3 Log-to-core calibration

Log-to-core calibration aims to correlate the core permeability with the calculated well log intrinsic permeability, as downhole tools cannot directly measure this important

reservoir parameter. The vertical resolution differs between core plug measurements and a well log. Core plugs are discontinuous in nature, and specific locations are chosen within a reservoir and seal for laboratory analyses. Well logs are continuous in nature, and typically have a vertical resolution of 30 – 45 centimetres (cm) with measurements dependable on borehole conditions (Rider and Kennedy, 2011).

Calibration of wireline logs with available core data in a well enhances reservoir characterization by increasing data density and improving the geological and geophysical interpretation in the formation of interest. In this dataset, only the 10-22 well has core data available with porosity and permeability measurements completed and were used for log-to-core calibration.

The total and effective porosity measurements from the three core plugs located within the BBRs target interval were compared to the calculated PHIT and PHIE logs, respectively. The PIGN and the wireline PHIT log were comparable to the helium porosity measurements completed in the RCA and the total porosity measured in the TRA, respectively. Calibrating the calculated log data with core plug measurements is required when relying solely on density and neutron log data, where the matrix density is unknown (Swager, 2015). Thus, the PHIT log did not require calibration with the core total porosity measurements.

The PHIE log was calculated based on an approach that involved estimating the volumes of clay present, the bound fluid, and the free fluid derived by Swager (2015). Originally, the PHIE log overestimated the amount of BF, producing a suppressed estimation of PHIE for the entire stratigraphic column. A second iteration of PHIE was calculated using a lower amount of BF, which produced a similar log response as the calculated PIGN curve during the ELAN. This second iteration of PHIE and the PIGN curve are comparable to the effective porosity measurements completed through the RCA and TRA methods. A comparison with the CMR curve was also made between the core measurements and the calculated PHIE curve, which followed and agreed with the PHIE values (Swager, 2015). As a result, both the PHIE and PIGN logs did not require calibration with the core effective porosity measurements. However, the availability of

the core measurements proved to be an invaluable tool to compare values of both total and effective porosity in the target interval.

The permeability measurements performed on cores located within the Foremost Formation and BBRS unit from both the TRA and RCA methods were compared to the estimated intrinsic permeability log, calculated using the Timur-Coates equation (Luthi, 2013). A first pass of correlating the KINT\_GEO from the ELAN dataset to the calculated K\_INT was completed for the entire length of the 10-22 well. However, the K\_INT curve required a calibration step in order to honour the core-measured permeability in the BBRS unit. The K\_INT curve was re-adjusted and increased using a 10:1 scalar factor, attempting to reach an order of magnitude closer to the permeability measured in the RCA and TRA methods, but matching the target permeability as highest priority (Swager, 2015). The difference between the non-calibrated and the calibrated K\_INT curve, along with the plotted core points is shown in Figure 3-26.

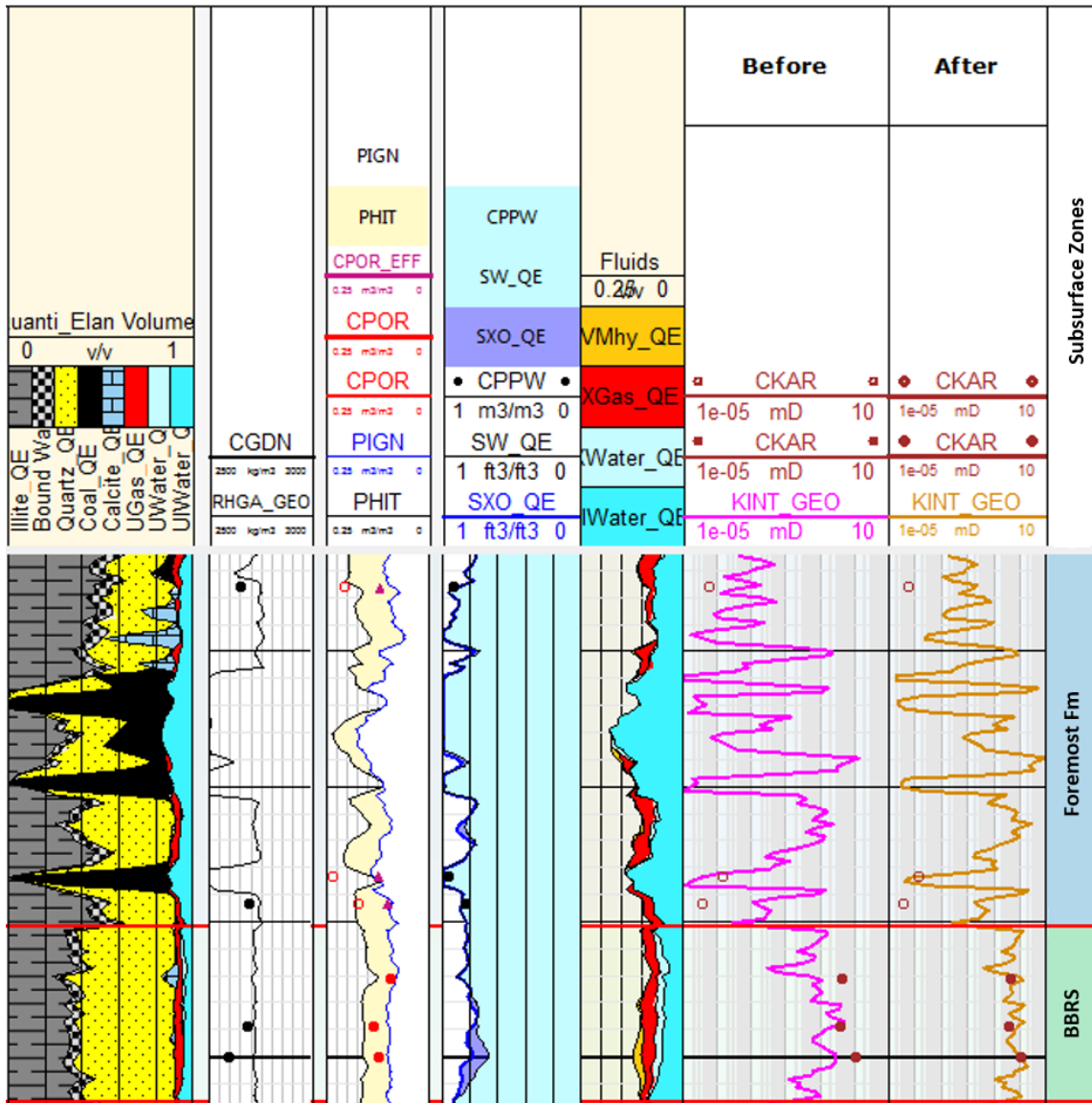


Figure 3-26. Before and after log-to-core calibration of K\_INT data for the 10-22 injector well, from Swager (2015).

It is not unusual for the calculated permeability to require calibration. The importance of obtaining core measurements is critical as a means of quality control and calibration. There can be differences with orders of magnitude between measured and estimated values, originating from the presence of micro-fractures, large authigenic clay volumes, as well as relative permeability effects if all parameters are not considered. Without core measurements, porosity and permeability may be under-reported and can

lead to imprecise representations or misinterpretation of a reservoir.

### ***3.2.3 Data analyses: Data transformation and variogram models***

Prior to petrophysical modeling and cell population, data analysis was completed for effective porosity and intrinsic permeability. Variogram statistics were assessed from the 88 wells that had the two main properties. The variogram tool is used to determine how spatially correlated a dataset may be, and provides estimations of unknown quantities in areas where data was not sampled. As a central tool of geostatistics, variograms provide randomness to a geological model with minimum and known variance quantities. The validity of a variogram model is largely dependent on the size of the dataset, where sample sizes in the range of 100 – 150 are adequate for analyses. Other factors that affect variograms include the lag interval and bin width, as well as the distribution, anisotropy, and any directional trends present in the data. (Oliver and Webster, 2015)

As a result of the FRS location and the size of the model, only 88 wells were capable of estimating effective porosity and intrinsic permeability based on the limited wireline suite available. According to the suggested range for adequate analyses by Oliver and Webster (2015), the data set is insufficient of providing a reliable variogram model to describe the spatial distribution and variation. However, the variogram tool was used in an attempt to describe any spatial distribution information present within the available data. The output of the variogram determined for each zone was used to guide the petrophysical modeling and cell population. The geostatic model has a total of 12 zones, and only the Foremost Formation, BBRS unit, and Pakowki Formation will be discussed in this section. The variogram model was chosen to remain constant across the three subsurface zones for simplicity (Zaluski and Lee, 2015).

Prior to computing the experimental variograms, the data was non-normal and required transformation. Based on the chosen method of model population, the Gaussian Random Function Simulation algorithm requires normality in the data set. For each subsurface zone, a specific Normal Score transformation was computed on the effective porosity and intrinsic permeability data. The curve is defined by the absolute maximum

and minimum of the input data set, and estimates the mean and standard deviation. These values are used to determine which larger or smaller values to suppress in order to create a distribution that is more symmetric.

In comparison to the input data distribution, the normal score transformation did increase the normality for the PHIE data in these three subsurface zones. As a result, the input and final output for data distribution is displayed in Figures 3-27 to 3-29 for the Foremost Formation (a, A), BBRS unit (b, B), and the Pakowki (c, C) Formation.

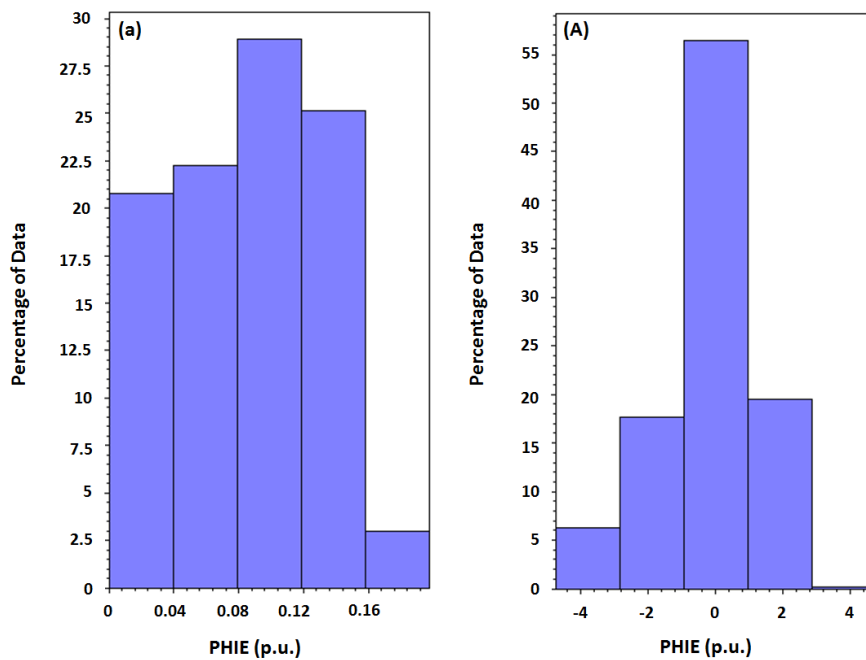


Figure 3-27. The input (a) and output (A) of a normal score transformation. The percentage of data represents the frequency of occurrence for PHIE values in the Foremost Formation.

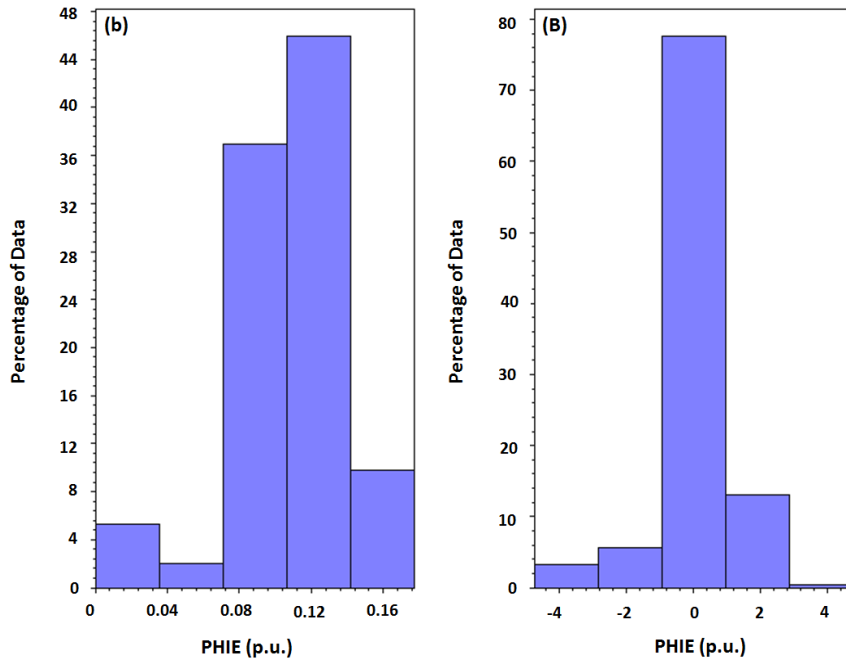


Figure 3-28. The input (b) and output (B) of a normal score transformation. The percentage of data represents the frequency of occurrence for PHIE values in the BBRs unit.

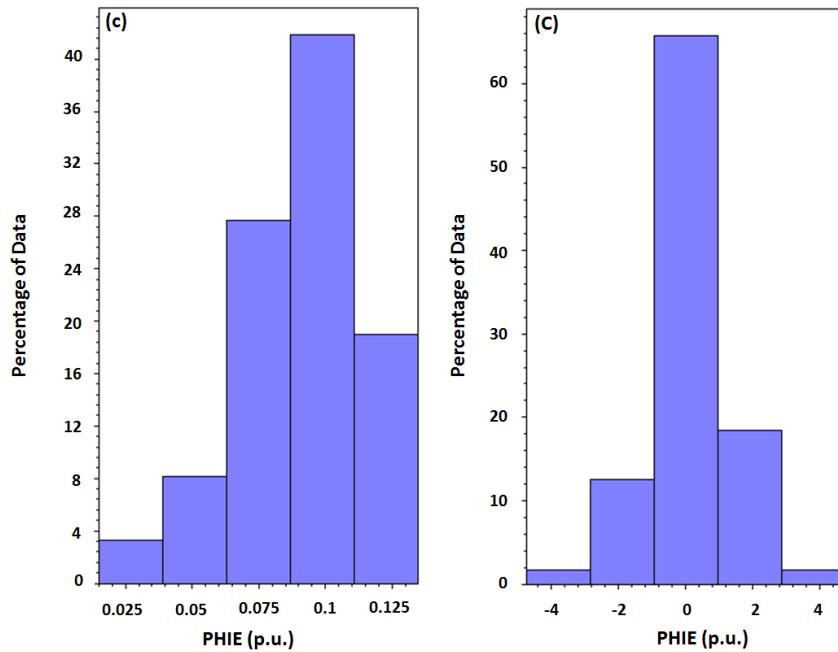


Figure 3-29. The input (c) and output (C) of a normal score transformation. The percentage of data represents the frequency of occurrence for PHIE values in the Pakowki Formation.

The data transformation displayed in a probability of occurrence for the Foremost Formation is shown in Figure 3-30. The resultant output demonstrates a mean PHIE of 8% with high volumes of low porosity. This is attributed to the coal zones that required their high PHIE values to be re-assigned to a lower PHIE value of 3%. The data transformation displayed in Figure 3-31 for the BBRs unit displays low normality, with a long left tail displaying low volumes of low effective porosity and the majority of the PHIE lies between 9 – 12%. The Pakowki Formation displayed the highest transformed normality in the PHIE data (Figure 3-32) amongst the three zones as the resultant output from the normal score transformation, showing slight dominance in the right-hand-side of the graph with a mean PHIE of 8%. Note that the data transformations do not ensure a high normality, but instead attempt to attain a quasi-normal distribution.

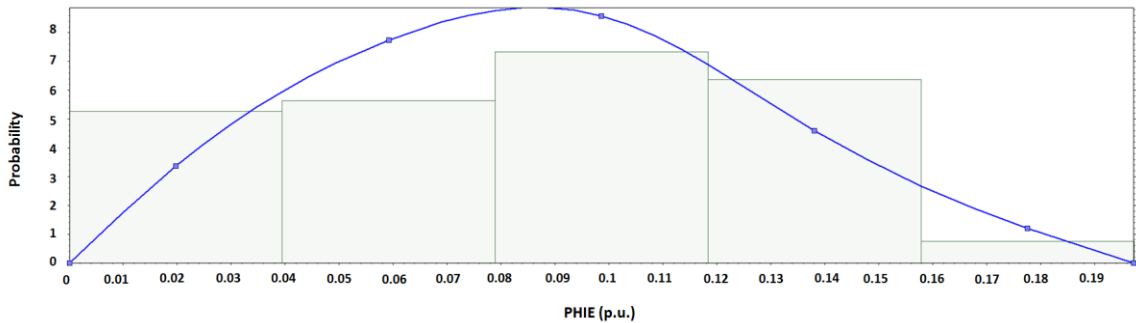


Figure 3-30. Resultant output of the normal score transformation on the PHIE data for the Foremost Formation, displaying the probability of occurrence for the modeled PHIE data range.

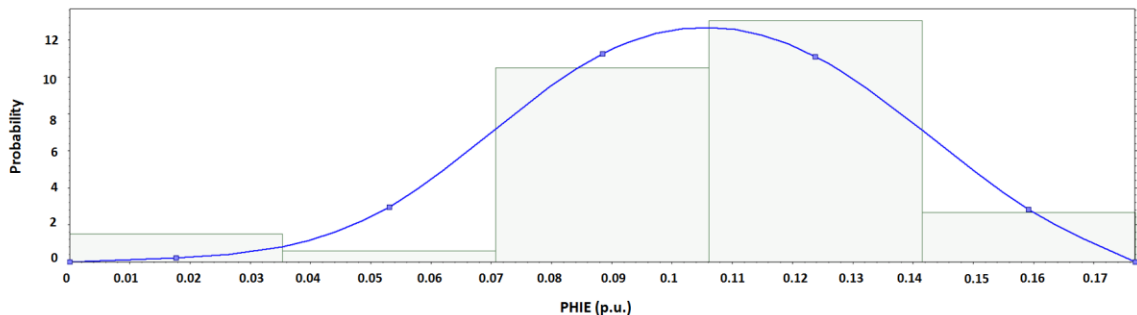


Figure 3-31. Resultant output of the normal score transformation on the PHIE data for the BBRs unit, displaying the probability of occurrence for the modeled PHIE data range.

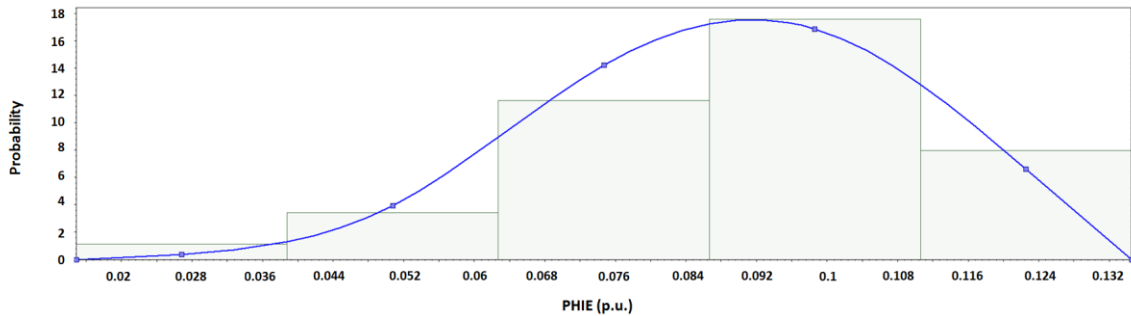


Figure 3-32. Resultant output of the normal score transformation on the PHIE data for the Pakowki Formation, displaying the probability of occurrence for the modeled PHIE data range.

Following the data transformations, the experimental variograms were computed. The vertical, major, and minor directions define the range of the variogram model. The range is the distance between two points which data can be correlated, where a larger range indicates greater continuity and less heterogeneity (Schlumberger Ltd., 2015). The vertical variogram relates to the stratigraphic component, where the thickness of the target interval of interest should limit the vertical range. The major and minor direction range is related to the lateral continuity of strata, where the minor direction is typically less than and perpendicular to the major direction range. The zone of data correlation is specified based on the search radius, azimuth, number of lags, and lag distance. Table 3-8 outlines the parameters used to obtain the experimental variogram data for the interpretation of the variogram model.

Table 3-8. Search cone parameters to bin and prepare the well log PHIE and K\_INT data for the variogram experimental model fit.

Direction	Azimuth (°)	Number of Lags	Lag Distance (m)	Search Radius (m)
Vertical	N/A	7	0.5	3.5
Major	150	9	300	2700
Minor	60	9	300	2700

The azimuth of the major and minor range direction determines which wells will be within lateral reach to be used for data correlation. The number of lags and specified

lag distance determine the search radius of the search cone. As a general rule, the search radius should be approximately half the length of the model grid. The model boundary is 5 km by 5 km, thus just over half (2500 m) was used. A lag is defined as the distance between a data pair for which the experimental variogram is calculated (PNNL, 2015). The lag distance and the number of lags determine the maximum distance between a data pair is correlated (PNNL, 2015). The lag settings are important for binning the experimental variogram data. The goal of setting the search cone parameters is to obtain as many data pairs as possible to be represented in any one variogram point. With more data pairs, the data set is better represented. However, the lag distance may be wider which results in less structure for the first few points of the variogram. Table 3-9 outlines the variogram model parameters that were used for all three subsurface zones for the PHIE and K\_INT data.

Table 3-9. The variogram model fitting parameters used for the PHIE and K\_INT data for all 88 wells in the FRS study.

<b>Parameter</b>	<b>Variogram Model Fit</b>
Regression curve type	Exponential
Sill	1
Major range	1500 m
Minor range	1500 m
Vertical range	1.25 m

In the 10-22 injector well, the target interval has a thickness of 7 m, and a mean thickness of 8 m over the 25 sq. km. region of the model. To capture any vertical heterogeneity present within the unit, the vertical range was set to 1.25 m. Knowledge of the homogenous horizontal strata over the FRS region, the major and minor directional range was set to 1500 m. The nugget was set to zero, as a non-zero nugget implies the “nugget effect”, where high discontinuity and randomness are present at samples with zero distance between them. The exponential model was attempted to fit the data (Figure 3-33 to 3-35), with knowledge of the pitfalls when completing variogram analyses on small datasets.

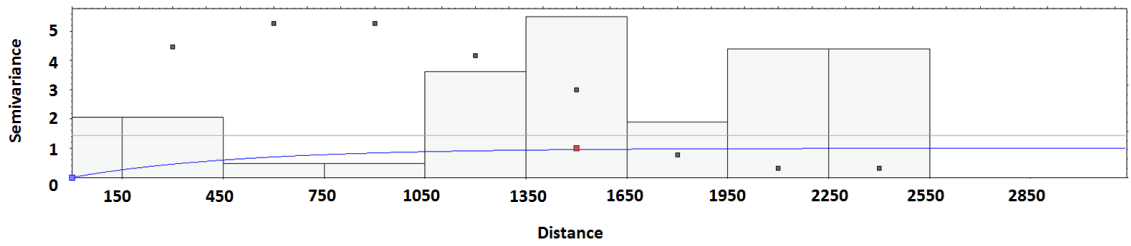


Figure 3-33. The major directional range in distance (m) with an exponential model variogram attempting to fit the PHIE data.

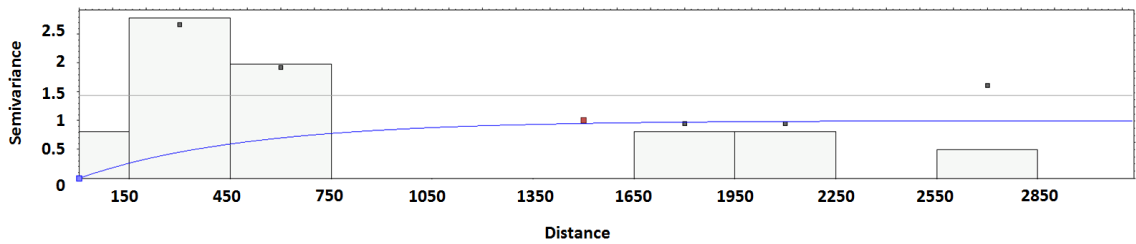


Figure 3-34. The minor directional range in distance (m) with an exponential variogram model attempting to fit the PHIE data.

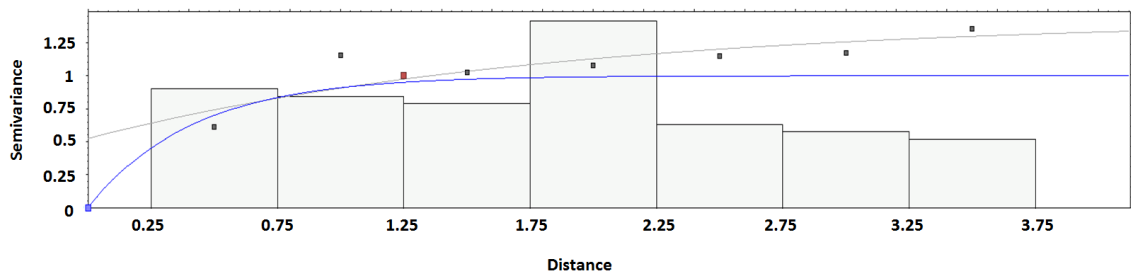


Figure 3-35. The vertical directional range in distance (m) with an exponential variogram model attempting to fit the PHIE data.

The variogram data for PHIE demonstrates sparse and random points, thus proving difficult to fit the exponential model to the data. The sill represents the variance of the underlying population, and is approached by the semi-variogram over the range. The sill value represents the variance of the variables, to which past the range, the data becomes uncorrelated. The sill was interpreted to be 1, and this value is set for the vertical, major, and minor direction variograms. A sill of 1 is typical of normalized data distribution. As a result of a small sample size, the sill does not appear to be reached over

the set range of 1500 m. The experimental variogram data for PHIE appear randomized and would require more than one simple variogram model type to fit the data. Other than the lack of data quantity to fit a proper variogram model, two additional explanations to the variance appearing in the data could be attributed to stratification or layering in the formations, as well as between-well differences in the averaged PHIE or K\_INT values. The degree of normality after the data transformations completed prior to the variography results were low, which could also add to a poor variogram model fit. Although the exponential model fit is poor on the semi-variograms in the vertical, major, and minor directions, the variogram settings were still utilized in the petrophysical modeling to guide the cell population of both PHIE and K\_INT properties. Thus, to enhance the variography results, a larger sample size is required to better understand the spatial distribution of the PHIE and K\_INT data in the wells.

### **3.3 Model geometry definition – gridding and layering**

The model volume is defined by the number of cells in the I-direction, J-direction, and the number of assigned grid layers ( $nI \times nJ \times nGridLayers$ ). The dimensions of the defined volume are  $197 \times 198 \times 1557$ , resulting in a total of 60 million 3-D cells. The model grid increment in the x-, y-, and average z-direction along the vertical pillar is 25 m, 25 m, and 0.77 m, respectively. Due to the lack of heterogeneity in structure in the region, a vertical pillar gridding method was chosen. The geometry of the model is simple, reflecting the structural low relief of the Plains and thus no fault model was required.

The structural framework of the model grid is dependent on the defined subsurface horizons, which were constructed utilizing the interpretation and interpolation of geological markers identified as formation tops on wireline logs, as well as those identified in the seismic volumes. The 5 km by 5 km surface boundary centered at the main 10-22 well was used to create both the 3-D grid and the subsurface horizons. The model is composed of 13 horizons, with a total of 12 zones. The number of grid layers defined within each horizon interval/zone enables the user to identify units of importance, and those of less importance by increasing the layer height at which the geological

properties were averaged. The cells within each grid layer were programmed to build from the bottom upwards. Rather than following the topographic character of the region, it appeared to be geologically sound to follow the underlying surface to eliminate any misleading artefacts such as erosional weathering that could affect the structure of the horizon surfaces.

For the FRS case, grid layers in the overlying and underlying seal and target intervals were assigned a height of 0.5 m, and those of non-important units were assigned a height of 5 m to avoid long computational runs for both property population and reservoir simulations. In the target intervals where the dynamic flow simulations will take place, it was important to define a finer-scaled grid layer height in order to monitor how the CO<sub>2</sub> plume will behave based on a well-represented property population. It will become important to identify and characterize any vertical fluid movement into the seal intervals based on the assigned petrophysical properties. For example, if the cell height were 5 m in the Foremost Formation, this would negate the efforts in re-assigning the coal zones a low PHIT of 3%. The cells would average over a 5 m vertical interval, resulting in a PHIE value higher than 3%, which may promote fluid flow into the seal interval during dynamic flow simulations. In the horizon intervals of low importance, larger-scaled grid layer heights are appropriate because the averaged properties will not affect the simulation and thus effort must be focused in the areas greatest of concern. Table 3-10 lists the layered zones for each horizon with the assigned grid layer height in the model.

Table 3-10. Layered zones with the assigned cell thickness size for the FRS geomodel.

<b>Zone Interval</b>	<b>Layering of Zones</b>	<b>Grid Layer Height (m)</b>
Overburden	Follow Base Surface	0.5
Bearpaw	Follow Base Surface	0.5
Oldman	Follow Base Surface	0.5
Foremost	Follow Base Surface	0.5

BBRS	Follow Base Surface	0.5
Pakowki	Follow Base Surface	0.5
Milk River	Follow Base Surface	5
Colorado	Follow Base Surface	0.5
Medicine Hat	Follow Base Surface	0.5
Second White Specks	Follow Base Surface	5
Base Fish Scales	Follow Base Surface	5
Bow Island	Follow Base Surface	5

The orientation of a model is often dominated by the flow of groundwater in shallower target intervals, and is often recommended by the reservoir engineer to apply the directional trend as it will have an effect on the behaviour of the CO<sub>2</sub> injection both in real-time and fluid simulation (Lee, 2014). For the FRS model, the measured orientation for groundwater flow in the Foremost Formation is northward (Worley Parsons Komex, 2008) and thus the model is oriented N – S.

### ***3.3.1 Upscaling and property generation***

Model cell population requires the two main petrophysical parameters, PHIE and K\_INT, to be upscaled into model properties. Upscaling these wireline logs computes the average of the curve over the 3-D grid layer height. In this case for the target and seal intervals, the values for PHIE and K\_INT were computed over a 0.5 m vertical interval. In the units of low importance, the values for these two wireline logs were averaged over 5 m. Once the wireline logs were transformed into properties through upscaling, 3-D cell population was completed for the entire 5 km by 5 km model volume.

The inputs for upscaling into the defined model grid are the PHIE and K\_INT wireline curves, producing the output of two properties scaled over the assigned 3-D grid layer height for the Foremost Formation and the BBRS unit (Figure 3-36). The averaging

method used is arithmetic, where the sample selection treats the wireline log as points. The minimum default number of points in a cell is three, and no zone correction was applied or required. This ensures that all sample values within each cell are used for averaging without being weighted. Where the curve is undefined or lacks data, the cell will remain undefined. This sample selection method uses the neighbouring cell method. This method determines which grid cells are penetrated by well paths, and will average the curve values from all cells adjacent to the upscaled cell. The arithmetic neighbouring cell method is typically recommended when upscaling wireline logs that are regularly sampled and continuous in nature. (Schlumberger Ltd., 2015)

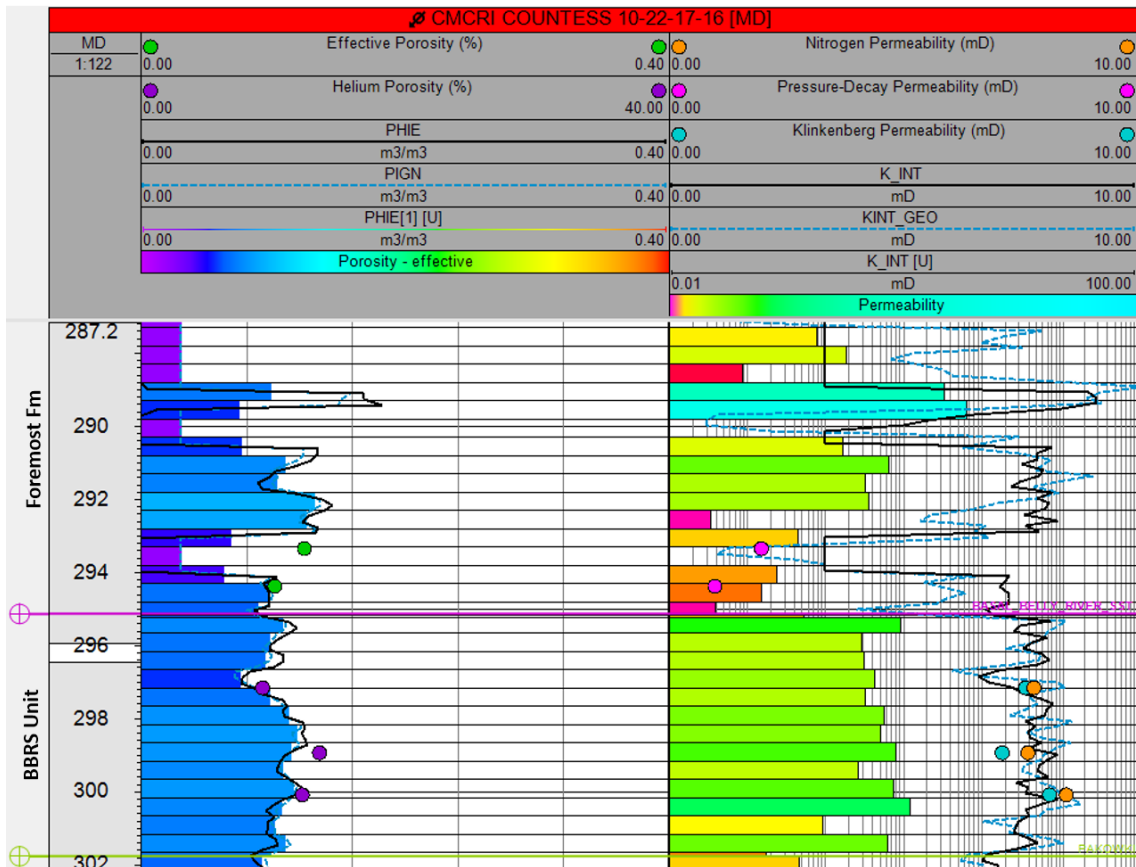


Figure 3-36. The upscaled PHIE and K\_INT curves displayed as blocked columns in a well section window for the 10-22 injector well within the BBS unit and the Foremost Formation.

The upscaled PHIE and K\_INT properties are displayed, and are mostly agreeable to their respective wireline curves. It appears in some cells that the properties are either under or over-estimated by the arithmetic averaging method in comparison to the log curves. This could be attributed to the neighbouring cells next to the grid cells that are penetrated with the 10-22 well path. Another possible reason could be that the log is under-sampled with three points over a 0.5 m grid layer height, and could be improved by increasing the sample point rate.

### ***3.3.2 Model population: Gaussian random function simulation algorithm***

The model was populated with PHIE and K\_INT property values by utilizing the Gaussian Random Function Simulation (GRFS) algorithm. It is considered to be a conditional simulation algorithm that incorporates both kriging and unconditional simulation (Schlumberger Ltd., 2015). Under the assumption that the data have a normal distribution, the Gaussian Geostatistical Simulation (GGS) algorithm is more advantageous than kriging. The algorithm is stationary in that over the spatial domain of the input data, the values for the mean, variance, and spatial structure do not change. Kriging produces a smoothed output because it is based on a local average, whereas the GGS inserts the local variability in the data that is lost. The conditional simulation portion of the algorithm then honours the input data and is able to model the expected variability in property distributions. The unconditional simulation portion of the algorithm does not replicate the data's mean, variance, or semi-variogram, and thus does not honour the input data. The difference between the two simulations is where the modeled data is placed on the cell grid. Variation in the sample location might occur because the modeled values are placed at the grid cell center and thus might not be in the exact location of the input sampled data point. Whereas in the unconditional simulation, a prediction map of the modeled property may display areas of high and low effective porosity values, but not in the location of where they exist in the input data. (Goovaerts, 1997)

The algorithm is parallelized, allowing for fast computation time for multiple model iterations. As well, a co-kriging option is available within the algorithm function

itself. This option can be used if there is a known geological feature with specified properties, and can be co-kriged into the simulation to honour that data. (Schlumberger Ltd., 2015)

The properties, upscaled cells, and original curves of PHIE and K\_INT can be compared to determine if the populated model honours the original distribution of the input data. In Figure 3-37, the histogram of the first realization iteration of PHIE for the BBRS unit is shown with the property (purple), upscaled cells (green), and the original log curves (red).

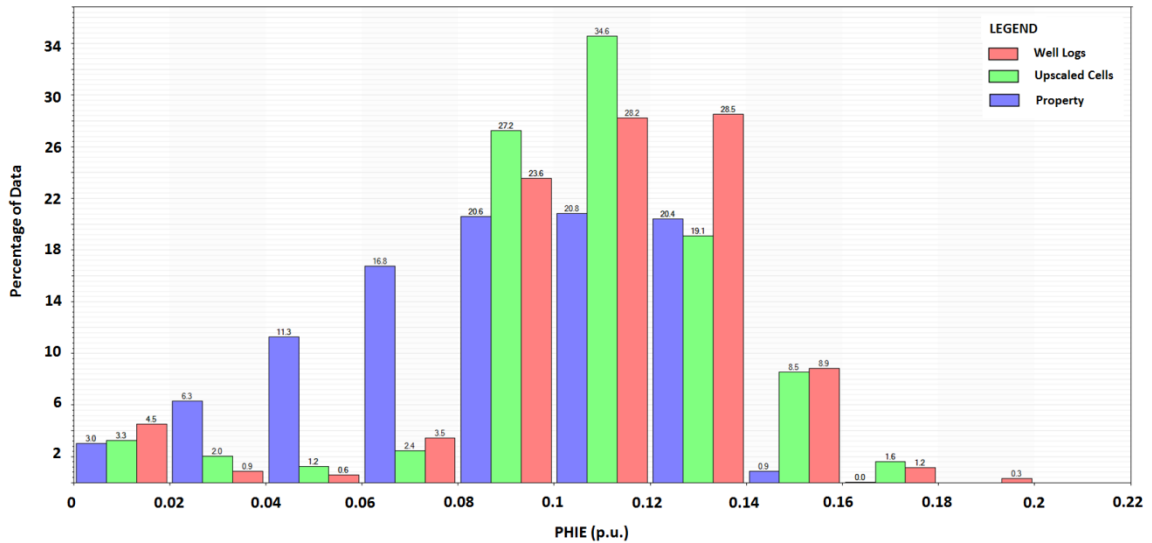


Figure 3-37. PHIE histogram for the BBRS unit, displaying how the data is represented in the well logs (red), upscaled cells (green), and modeled property (purple) in the 3-D model.

The graph demonstrates a front-loaded but generally normally distributed PHIE data from all three inputs. The upscaled cells appear to give a good representation of the original log curves. The property appears to represent the lower values of PHIE fairly well, but towards the mean value of 11% demonstrates the majority of the subsurface zone is populated with PHIE values of 9 – 12% as a result of the GRFS algorithm. The distribution of the three data inputs is expected to change slightly for each realization the PHIE model is run.

The histogram for the first realization iteration of K\_INT for the BBRS unit is shown in Figure 3-38. The property (purple), upscaled cells (green), and the original log curves (red) are shown to determine if the populated K\_INT model honours the distribution of the input data.

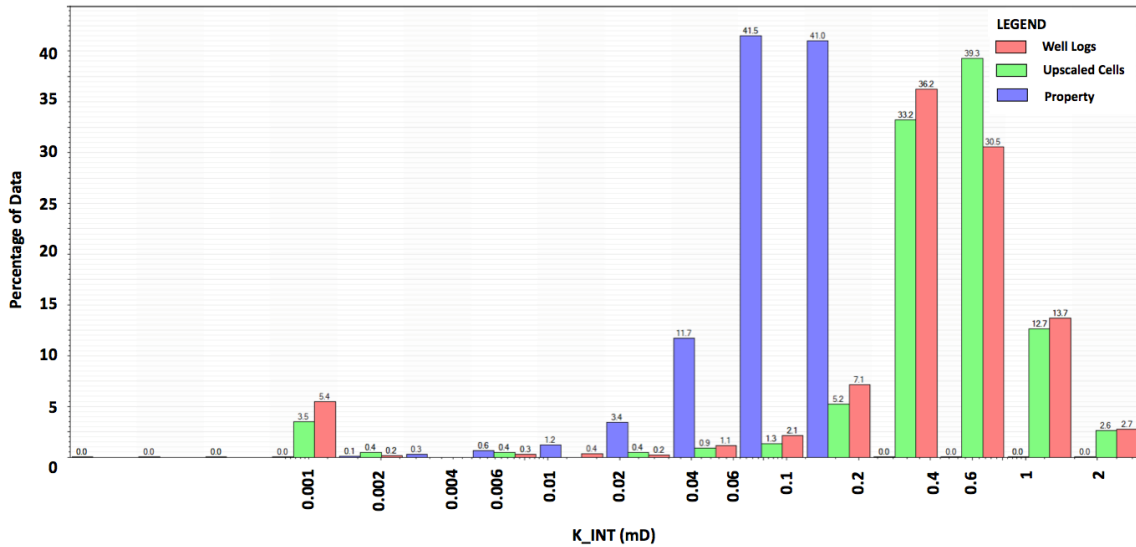


Figure 3-38. K\_INT histogram for the BBRS unit, displaying how the data is represented in the well logs (red), upscaled cells (green), and modeled property (purple) in the 3-D model.

The graph demonstrates a non-normal distribution of the K\_INT data, and demonstrates that modeled K\_INT populated 100% of the 3-D model with values ranging from 0 to 0.01. The upscaled cells show a good representation of the well logs, however it appears this does not transfer when modeled. This is believed to be caused by the 10-22 well that had the permeability data from the core lab measurements biasing the modeled K\_INT values to be very low. As well, the type of averaging method selected for upscaling the well logs into the model cells has an effect on how well the data is represented once modeled. Similar to the PHIE data, the distribution of the three data inputs is expected to change slightly for each realization the K\_INT model is run.

The populated geomodel with the PHIE and K\_INT property in the first three zones, including the Foremost Formation, BBRS unit, and Pakowki Formation are

displayed in Figures 3-39 and 3-40. The mean PHIE and K\_INT modeled values for the BBRS unit was 11% and 0.57 mD, respectively.

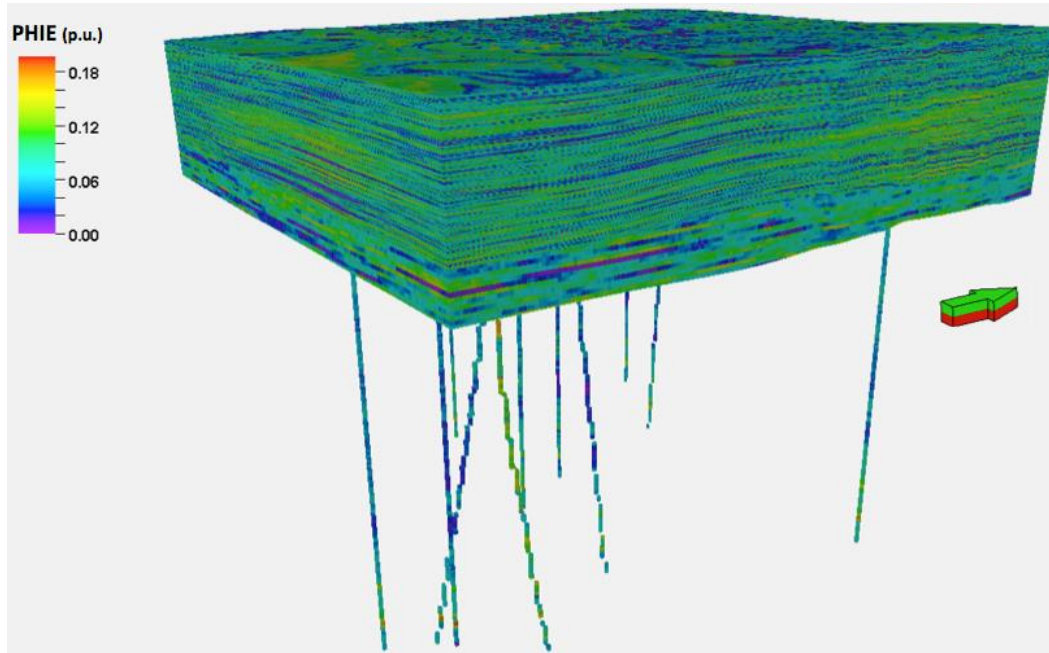


Figure 3-39. The 25 sq. km FRS model populated with PHIE in the Foremost Fm, BBRS unit, and Pakowki Fm. Wells below the model section display the upscaled cells.

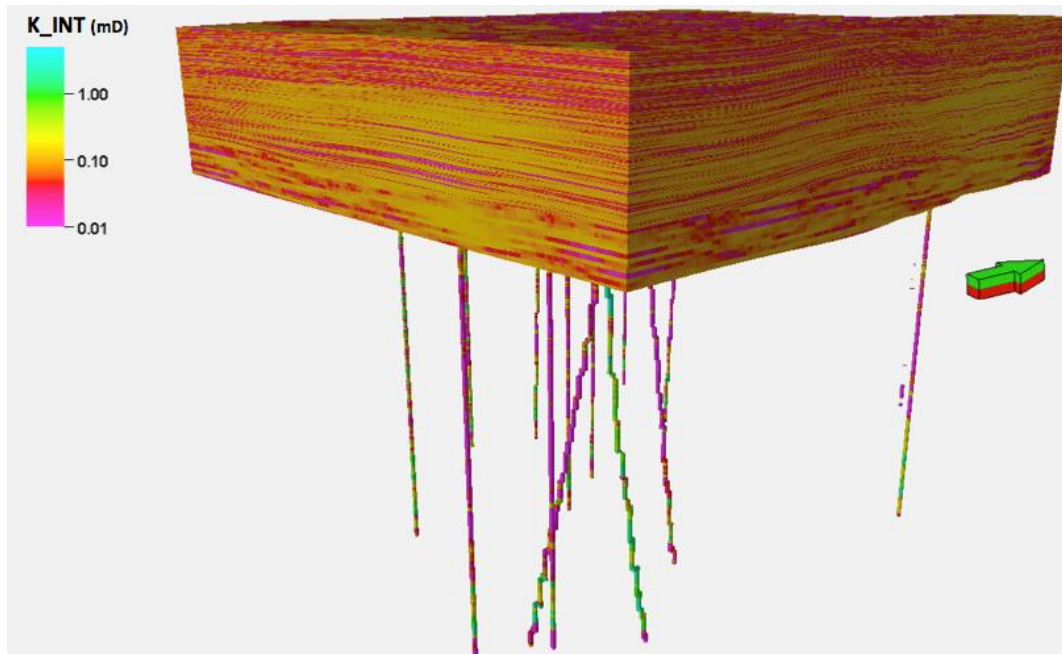


Figure 3-40. The 25 sq. km FRS model populated with K\_INT in the Foremost Fm, BBRS unit, and Pakowki Fm. Wells below the model section display the upscaled cells.

## 3.4 Discussion

### 3.4.1 Sources of uncertainty in static geological models

Models are tools to approximate reality and can be conceptual, mathematical, or a combination of the two (Meunier et al., 2013). In part of risk assessment and management, geological reservoir modeling is a vehicle used to highlight these risks and quantify uncertainty (Fichtl et al., 2013; Bentley, 2013). Understanding the sources of uncertainty and the associated risks aid in decision-making processes for the development, exploration, and production of a target interval.

The modern-day advancements in technology have supported the increase in size of geological and simulation models. Often the number of realizations iterated by these models aids in expressing and defining the uncertainty in the data, where higher number of realizations is preferred. The common size and complexity of geological models have become great, to which the handling capability of both the software and hardware are being challenged. The quality and accuracy of a geomodel should not be defined by its size or complexity, as best practices of geomodeling are continuously redefined with the technology advancements. (Bentley, 2013; Stunell, 2013)

Sources of uncertainty are scattered throughout the modeling process, from the data input to the a priori geological knowledge, assumptions, and thought processes of the geomodeler. Sources of uncertainty can be static or dynamic, where the latter is associated with fluid-flow simulations and is typically analyzed by a reservoir engineer. Data quality is a major source of uncertainty, and has led to poor reservoir performance predictions (Fichtl et al., 2013). Skorstad and Leahy (2013) state truthfully that it is a mistake to consider acquired field data to be 100% accurate, whether the data be wireline logs, seismic reflection data, or core measurements. The lack of precise data or well control (wireline and core data) increases static uncertainty, as these data inputs provide excellent but finite deterministic control on both stratigraphic and depositional model frameworks (Cox et al., 2013; Meunier et al., 2013). When considering wellbore position and associated uncertainty, understanding the well path and drilled trajectory is critical. In addition to the subsurface position and location of the wellbore, uncertainty lies in the

assumption that wireline logging tools are calibrated and used with standardized QC operating procedures (Skinner, 2013). Best Practices of wireline logging may not always be performed and can lead to poor borehole measurements. An example includes lowering logging tools too quickly, leading to poor borehole conditions or mismatched depth-to-log measurements that require post-processing QC efforts.

The lack of imprecise data such as seismic reflection data can also increase static uncertainty. A common pitfall to geomodelers is to assume the seismic data is solely sufficient in producing a structural model (Skorstad and Leahy, 2013). Although seismic data provides constraints on a larger scale for gross structural and stratigraphic frameworks, the understanding of a depositional framework is poorly defined without the refinement of well data (Cox et al., 2013). Höcker (2013) noted that uncertainties associated with subsurface depth and structures have the longest track record of applying stochastic methods to quantify uncertainty. Velocity modeling for model depth conversion is also defined as a source of uncertainty. The quality of the seismic volume affects the horizon picking uncertainty, which affects the TWT input for computing interval velocity. The quality of the sonic logs and access to check-shot data affects the quality and validity of a well-to-seismic tie. Estimated interval velocities can be erroneous with stretch-squeeze adjustments, which results in affecting the TDR as seen in this FRS model. Integration of velocity information can be useful for estimating realistic ranges. However, velocity models with high complexity or velocities conflicting with geomechanical and lithological trends can produce velocity-related depth errors (Höcker, 2013).

Combining the knowledge of known static and dynamic sources of uncertainty can raise the awareness of the geomodeler, affecting the workflows used through the duration of model construction. Geological and geophysical interpretation can be completed with greater understanding and knowledge of datasets if uncertainties are exposed and highlighted (Bond, 2013). The predication capability of the geomodel may be limited by unknown sources of uncertainty, which cannot be accounted for (Meunier et al., 2013). If constructing a model in a previously developed field, history matching of data and uncertainty analyses can be utilized as a basis for geological knowledge and

comparison. Increasing data density and integrating multiple data sets, reduces the risk of producing radical errors in a geomodel (Meunier et al., 2013). Communication of uncertainty amongst industry professionals in the field to the boardroom is critical when advancing the development of the model, and making business decisions based on the results produced by a static or dynamic geomodel.

For this geostatic model, a P10-50-90 framework was used to quantify the uncertainty. This method produces equi-probable outcomes of the effective porosity and intrinsic permeability over a number of realizations, and analyzed for the total pore volume distribution.

### ***3.4.2 P10-50-90 Statistical analyses***

As described by Mao-Jones (2012), “uncertainty should be modeled with probability distributions (a range of possibilities combined with probabilities assigned to each of those possibilities).” In order to communicate the uncertainty that is within the property model, the P10-50-90 framework was used. It refers to the data ranges between the 10<sup>th</sup>, 50<sup>th</sup>, and 90<sup>th</sup> percentiles. The P10 is typically referred to as the conservative outlook or the “lowest value that the expert thinks that the uncertain variable could be” (Mao-Jones, 2012). The P50 is typically referred to as the typical or “most likely value” (Mao-Jones, 2012). Lastly, the P90 is often referred to as the most optimistic, or the “highest values that the expert thinks the variable could be” (Mao-Jones, 2012). Any data points that lie before the P10 and after the P90 are very unlikely scenarios (Zaluski, 2014).

As a result of constructing a geomodel with over 60 million 3-D cells, a 1 km by 1 km volume clip of the BBRS unit centered at the main 10-22 well was used. The base of the Foremost Formation and the top of the Pakowki Formation defines the vertical extent of the volume clip. A workflow was constructed to model the PHIE for 40 iterations. Due to the capacity of computation power, there was a limitation on the number of iterations that could be run. It is understood that the greater number of model iterations will produce a data distribution closer to a normal score. As well, the static uncertainty is better defined with a large number of model realizations. Once the total effective pore

volumes were modeled, a total of 22 bins were used to organize the data by frequency and range and plotted to view the distribution for the BBRs unit (Figure 3-41).

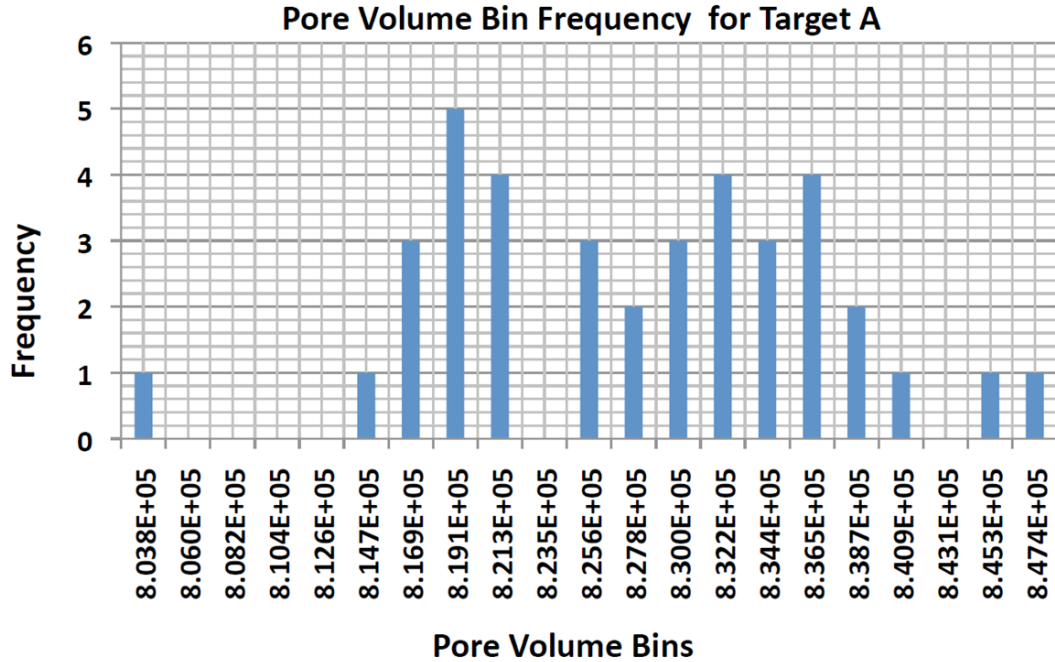


Figure 3-41. Assigned pore volume bins based on pore volume sum data. The plot displays the occurrence frequency for the BBRs unit in a 1 km by 1 km clipped volume centered on the main 10-22 injector well in the FRS model.

In Figure 3-42, the P10-50-90 percentiles are labelled on the graph identifying the ranges of data for the PHIE in the BBRs unit. To obtain the corresponding K<sub>INT</sub> volume with respect to the P10-50-90 percentiles, the petrophysical modeling for K<sub>INT</sub> was re-run utilizing the collocated co-kriging method. The GRFS algorithm computed the K<sub>INT</sub> for the BBRs unit while using a constant coefficient of 0.7 with respect to each respective P10-50-90 PHIE volume. For each P10-50-90 percentile, there is a corresponding realization number to each. These three realizations of PHIE and corresponding K<sub>INT</sub> volumes of the target interval were used in the dynamic fluid-flow simulation for CO<sub>2</sub> injection.

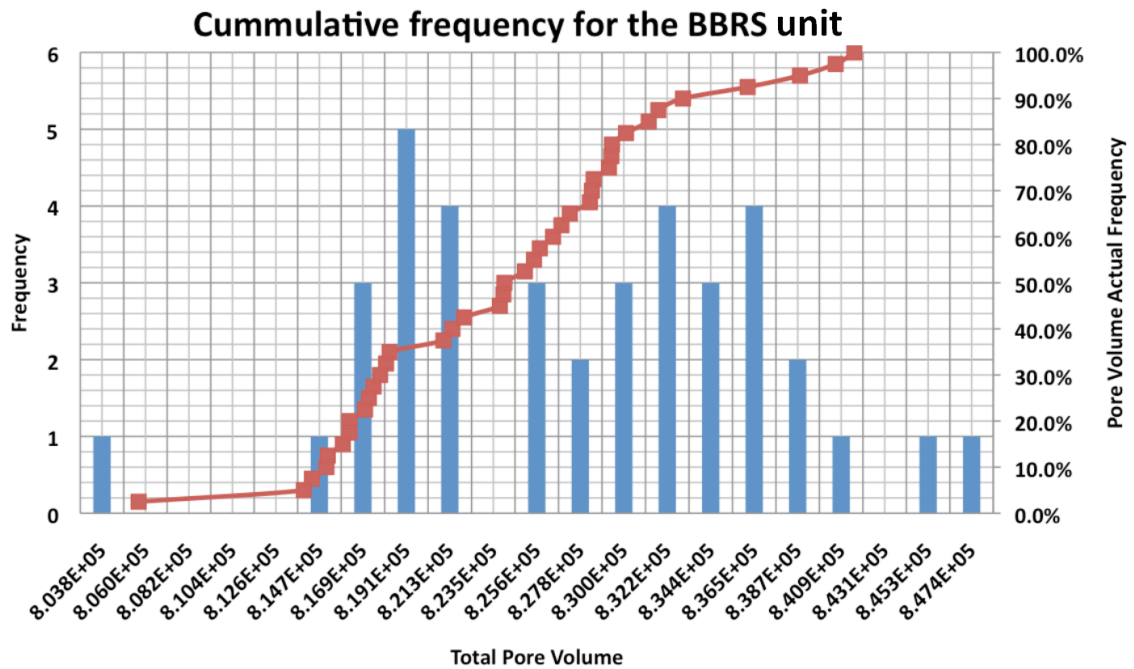


Figure 3-42. Total effective pore volume data for the BBRS unit in the 1 km by 1 km clipped volume. The occurrence frequency and pore volume actual frequency are shown to demonstrate the corresponding P10-50-90 percentile case ranking.

Although the P50 ranking provides a typical case, as displaying the majority of the data resides above and below the 10% and 90% percentile cases, respectively, a greater number of iterations is suggested to provide a better representation of the property variability modeled in the PHIE and K\_INT data. Not only will a larger number of modeled iterations provide a greater understanding of the modeled properties, but the normality in the data distribution is believed to increase.

## Chapter Four: **Dynamic Fluid-Flow Simulation**

### **4.1 Simulation input parameters**

The primary goal of advancing the static model for dynamic fluid-flow simulations was to obtain a prediction of an injection test for the CO<sub>2</sub> plume migration and distribution in the BBRS unit. The dynamic modeling work involves testing of multiple injection scenarios. For the initial model, a single well injection at the 10-22 well located at the center of the model was used with injection rates up to 1000 t/CO<sub>2</sub> per year over five years.

The 5 km by 5 km model volume with the P10-50-90 PHIE and respective K\_INT properties was the main input for fluid-flow simulation. The dynamic model was clipped to 4925 m by 4975 m and is composed of the Foremost Formation, BBRS unit, and Pakowki Formation. Note that these three zones are critical for fluid-flow simulations, as they represent the seal, target, and underlying seal zones. The static model was constructed with over 60 million 3-D cells, which required the model grid to be upscaled in order for the simulator to utilize the model input. A tartan grid configuration aided in upscaling the model and the number of cells (n) and smallest 3-D cell sizes around the injector well are listed in Table 4-1. Note the cell size in the z-direction is listed for the vertical cell heights in the BBRS unit.

Table 4-1. Number and size of cells used for upscaling the FRS geomodel with a tartan grid configuration.

<b>X</b>		<b>Y</b>		<b>Z</b>	
<b>nX</b>	125	<b>nY</b>	127	<b>nZ</b>	69
<b>Cell size</b>	8.4 m	<b>Cell size</b>	8.4 m	<b>Cell size</b>	0.5 m

From 60 million 3-D cells, the upscaling process decreased this number to just over 1 million 3-D cells in the model (nX, nY, nZ) defined by (125, 127, 69). Figure 4-1 displays the upscaled tartan grid in plan view of the dynamic geomodel domain. The

model grid size was constructed to be 5 km by 5 km, however it is believed with the constant cell sizes in the static model affected the upscaling completed in the dynamic model and resulted in the 4925 m by 4975 m dimension.

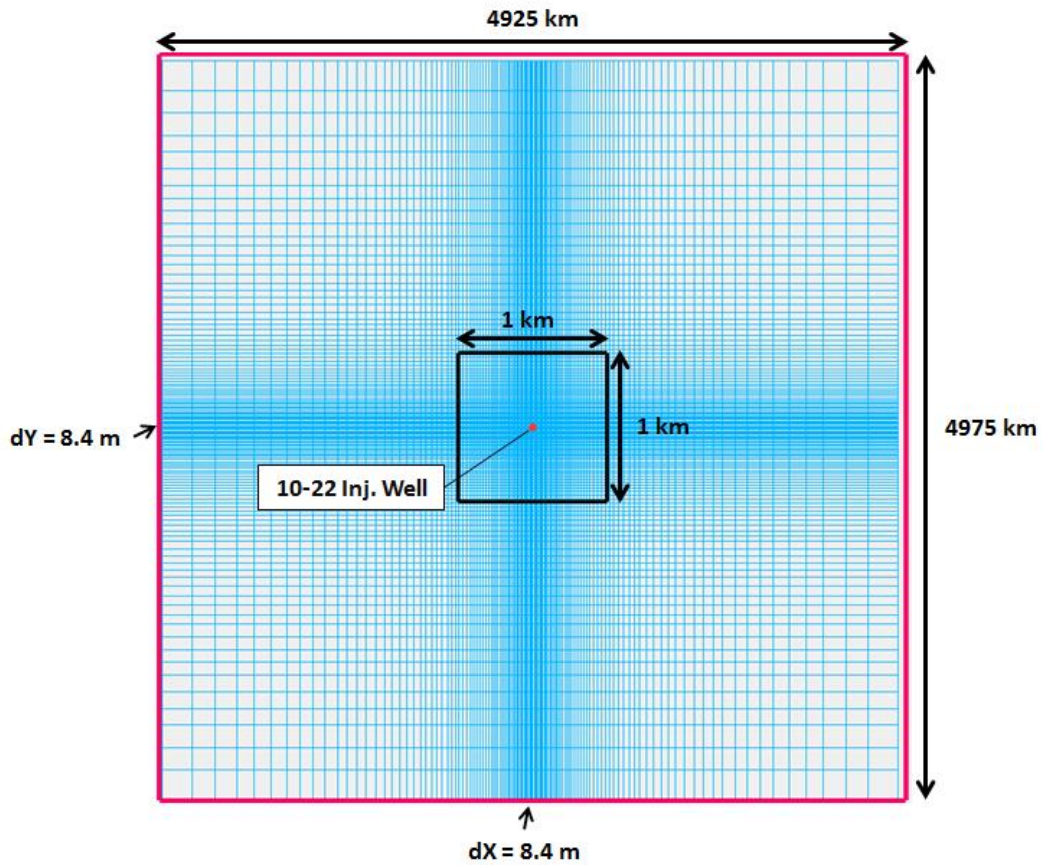


Figure 4-1. The tartan grid used to upscale the static geomodel. Finer cell sizes (8.4 x 8.4 x 0.5 m) are located closer to the 10-22 injector well. Modified from Lee (2015).

Additional layers in the z-direction were added at the base of the Foremost Formation to add resolution, and incorporate the lower  $K_{INT}$  values of 0.001 mD within the coal zones directly above the BBRS unit. The vertical component of cell size plays a critical role to highlight the limiting vertical permeability. With cell sizes too large, the low relative permeability of the coals and other tight zones remain unseen, as it becomes averaged over a larger vertical upscaled cell. Figure 4-2 demonstrates the thinner layers at

the base of the Foremost Formation, directly above the BBRs unit.

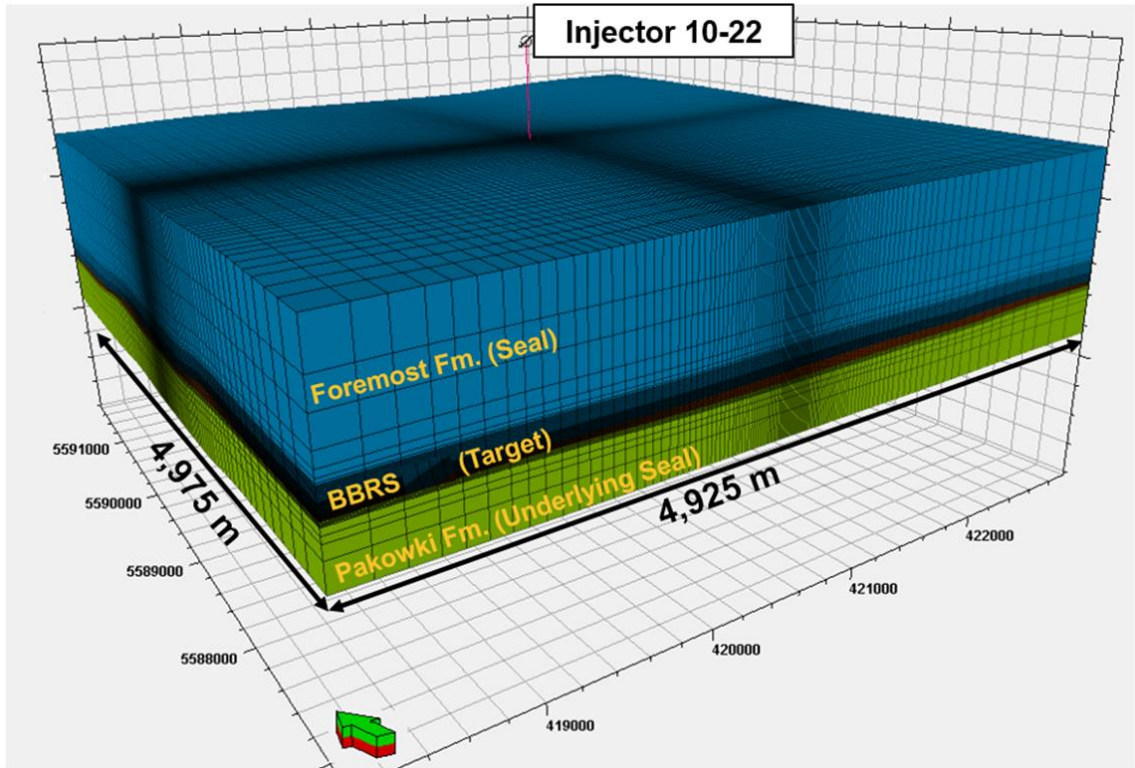


Figure 4-2. Upscaled 3-D grid of the dynamic model demonstrating the tartan grid configuration used. The three zones consisting of the Foremost Fm, BBRs unit, and Pakowki Fm are labelled. Figure modified from Lee (2015) with a Vertical Exaggeration (V.E.) of 5.

The reservoir simulation parameters used on the dynamic model are listed in Table 4-2. The reference datum pressure was estimated using the hydrostatic gradient. The hydrostatic pressure gradient for freshwater is 9.8 MPa/km (Pohl, 2011), thus the pressure at 300 m depth was calculated to be 2.94 MPa. The reservoir temperature was estimated from a single point at target interval depth (300 m) from the Array Dielectric Tool (ADT) log. The salinity of formation water is known to be brackish, ranging from 1,000 – 3,500 ppm as determined by a Worley Parsons Komex (2008) report completed in the Newell County region. Rock compressibility was calculated by Goodarzi (2015) using the Geertsma (1957) method. The calculation is based on three core lab measurements within the BBRs unit that include grain density, bulk density, and total

porosity. To avoid pressure build up, pressure breach, or fracturing the reservoir or borehole during injection, the maximum allowable bottom hole pressure (BHP) is a parameter used as a guideline to mitigate this risk. The maximum BHP is considered to be 90% of the lithostatic pressure at reservoir depth needed to fracture the rock. Considering the lithostatic pressure gradient is 24.5 MPa/km (Karner, 2005), at 300 m depth the maximum BHP was calculated to be 6.615 MPa. Of the flow parameters, the ratio of vertical to horizontal intrinsic permeability was estimated to be 0.1, which assumes fluids will primarily flow horizontally (Lee, 2015).

Table 4-2. Reservoir simulation parameters used on the dynamic model for CO<sub>2</sub> injection. Modified from Lee (2015).

Parameter	Value
Pressure (reference datum) at 300 m depth	2.94 MPa
Reservoir temperature (isothermal)	20°C
Salinity	1,000 ppm
Rock compressibility (3 samples ~300 m)	4.18 E-04 (1/bar)
Maximum allowable BHP at 300 m depth	6.615 MPa
$\kappa_v/\kappa_h$	0.1
CO <sub>2</sub> -water relative permeability	$S_{wmin}=0.5, \kappa_{rCO2}=0.5$ (end-point gas $\kappa_r$ )

The CO<sub>2</sub>-water relative permeability ( $\kappa_{rCO2}$ ) denoting the irreducible water saturation ( $S_{wint}$ ) was estimated using the Brooks-Corey approximation (Brooks and Corey, 1964; Lee, 2015). This widely accepted model is used for a gas-oil-water system to calculate relative permeability using capillary pressure data (Li and Horne, 2006). From Figure 4-3 constructed by Lee (2015), the minimum water saturation ( $S_{wmin}$ ) and critical water saturation ( $S_{wcr}$ ) are set to 0.5. The maximum water saturation ( $S_{wmax}$ ) and the water relative permeability at maximum water saturation ( $\kappa_{rw}$ ) are set to 1. Thus from the graph, when the  $S_{wmin}$  is 0.5, the relative permeability of CO<sub>2</sub> to water/brine ( $\kappa_{rCO2}$ ) is 0.5.

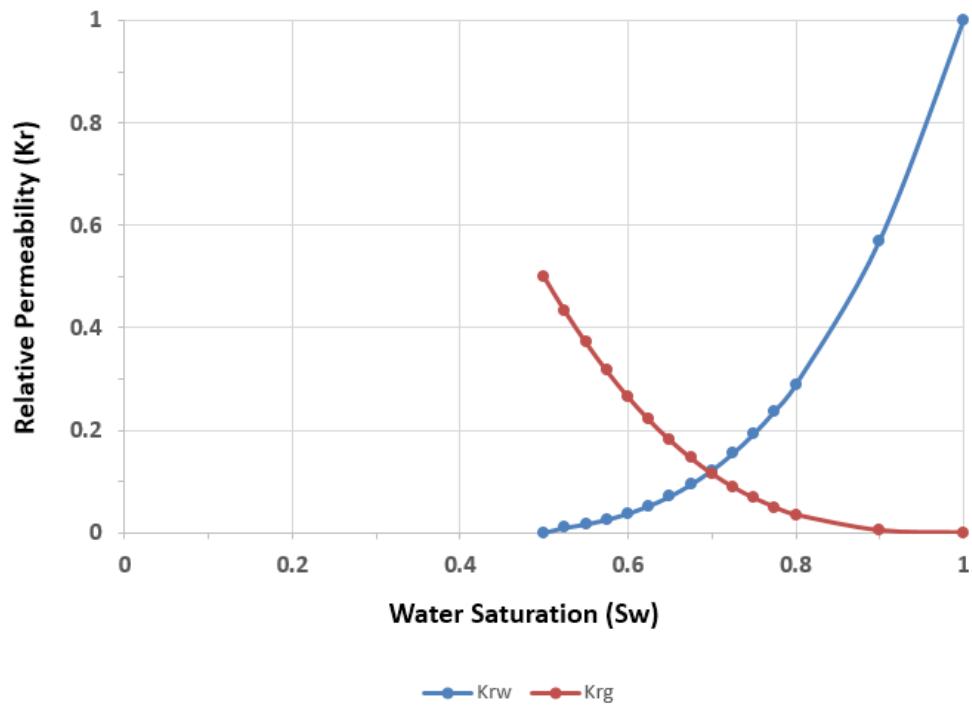


Figure 4-3. A Brooks-Corey model modification by Lee (2015) to approximate relative permeability of CO<sub>2</sub> to water saturation.

The inputs for the dynamic model domain include the three geological realizations of PHIE and K\_INT that correspond to the approximated P10-50-90 percentiles of the static model data. The dynamic model assumes 100% water saturation and does not consider geochemical or compositional changes of phases. The dynamic model does however consider CO<sub>2</sub> gas dissolution into the formation water in the pore spaces. The initial simulation scenarios intended to have continuous injection period, totalling 1000 t/CO<sub>2</sub> per year over a five-year period. However, the dynamic model parameters are subject to the maximum allowable BHP in the target interval. During the simulation process, the maximum allowable BHP was being exceeded and creating unstable scenarios as the model was unable to reach convergence. The simulation scenarios have been modified to reflect modified multiple monthly injections with shut-in periods, to allow the formation and borehole pressure to disperse before further injection commences. Table 4-3 denotes the five-year injection plan used for the three dynamic

model simulation scenarios created by Lee (2015).

Table 4-3. The modified five-year injection plan used for the three dynamic model simulation scenarios.

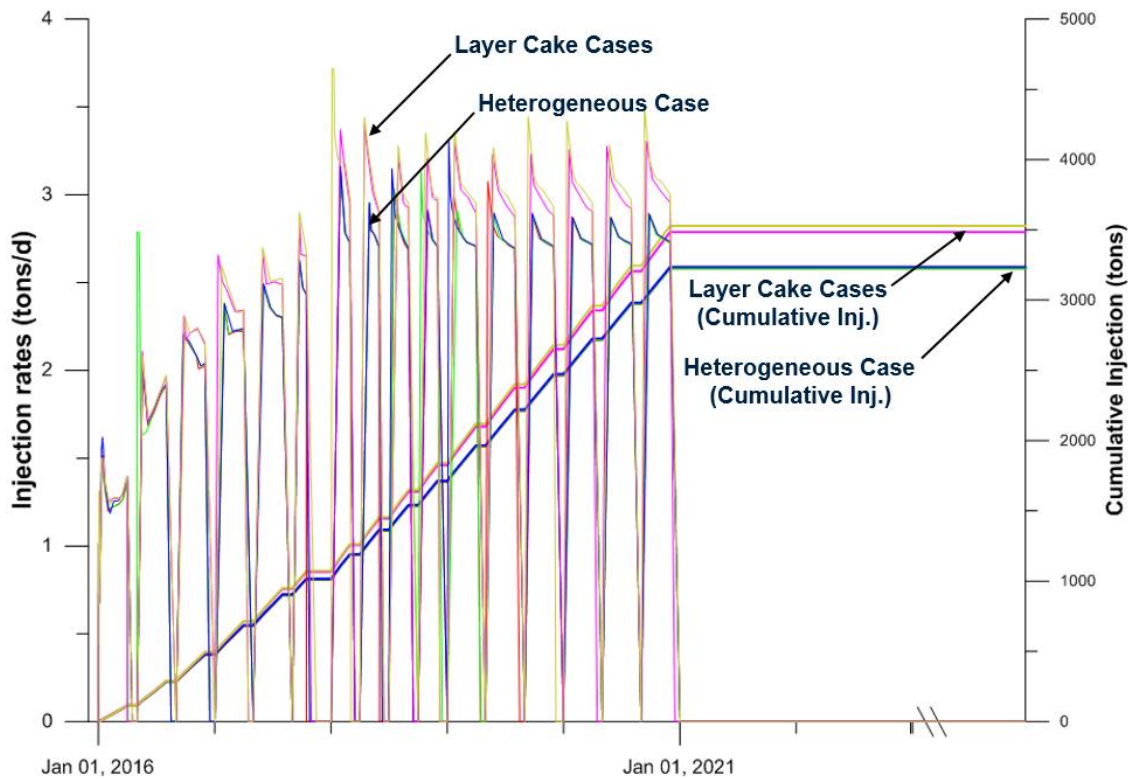
<b>Date</b>	<b>Injection Period</b>	<b>Shut-in Period</b>
January 1, 2016 – October 14, 2017	3 months	1 month
October 15 – December 31, 2017	-	2.5 months
January 1 – December 31, 2018	2 months	1 month
January 1, 2019 – November 30, 2020	3 months	1 month

The boundary conditions for the reservoir assumed infinite-acting conditions at the lateral boundaries of the dynamic geomodel. This was completed by applying a pore volume multiplier of  $10^6$ , creating an artificial boundary and making the lateral extent of the model expansive. By assuming an infinitely large aquifer volume, the artificial boundary acts as a pressure sink after CO<sub>2</sub> injection and mediates the dissipating pressure. Thus, the simulation of injections are completed in the dynamic model domain and beyond to avoid artificial pressure build-up. The Oldman and Milk River formations act as the dynamic model vertical bounds, where no-flow boundaries were assumed. No-flow boundaries act as perfect seals, such that no flow of injected CO<sub>2</sub> crosses the boundary. It is possible that pressure build-up may occur at these no-flow boundaries, if present. (Lee, 2015)

## 4.2 Simulation results

The simulated scenarios for the P10-50-90 case of the 5 km by 5 km geodynamic model are considered to be preliminary findings and are referred to as the heterogeneous case. High levels of uncertainty still remain in the geostatic property model itself, reservoir pressure, fracture pressure, capillary pressure, vertical and horizontal permeability ratio, and the gas-water relative permeability (Lee, 2015).

Another set of 1 km by 1 km layer cake models have been produced and created solely on the basis of the 10-22 well. These two layer cake models also have P10-50-90 scenarios for PHIE and K\_INT. The average permeability amongst the three models changes. A higher average K\_INT in the BBRS unit in the P50 case of 0.62 mD was found for the layer cake models, in comparison to the 0.47 mD of the larger heterogeneous case. The layer cake models lack complexity, and assume a single connectivity where an entire subsurface layer is assigned a K\_INT value without changing from cell to cell. Whereas the heterogeneous case changes from cell to cell, and has various K\_INT inputs from surrounding wells as assigned by the zones variogram values. Figure 4-4 displays the dynamic simulation results for the injected CO<sub>2</sub> into the BBRS unit for the full lifetime period of the project, for the full 5 km by 5 km heterogeneous model as well as the layer-cake models.



### Legend

— Inj Rate, P90	— Cumulative Inj, P90
— Inj Rate, P50	— Cumulative Inj, P50
— Inj Rate, P10	— Cumulative Inj, P10
— Inj Rate, Layer Cake w/ Structural Variations	— Cumulative Inj, Layer Cake w/ Structural Variations
— Inj Rate, Layer Cake	— Cumulative Inj, Layer Cake

Figure 4-4. Simulated CO<sub>2</sub> injection into the BBRs unit over a five-year period constrained by the maximum allowable BHP. Figure taken by Lee (2015).

The higher average K<sub>INT</sub> value of 0.62 mD in the layer cake cases demonstrate increased injection rates, leading to a greater overall cumulative injection of CO<sub>2</sub> into the target interval. The gap between the monthly injections are represented as the shut-in periods, where injection ceases to allow the formation pressure to dissipate and the plume to move away from the borehole. The shape of the graph during injection period is representative of a pressure differential ( $\Delta p$ ) in the reservoir. After a shut-in period, the

pressure in the reservoir is lowered. The next injection period then experiences a  $\Delta p$ , with low formation pressure and then higher pressures from the injection of CO<sub>2</sub>. As observed from the graph, the higher the  $\Delta p$  allows for greater injectivity rates of CO<sub>2</sub> and are marked by the peaks at the beginning of each monthly injection period. As injection proceeds,  $\Delta p$  decreases as a result of the formation pressure rising and is depicted by the decreasing injection rates that follow the initial peak of the monthly injection period. For the heterogeneous and layer cake models, the P90 case for displays higher injection rates than the P50 case, which is always greater than the P10 case, as expected.

The initial target of injecting 1000 t/CO<sub>2</sub> per year was not met, as a result of the BHP limitations. If injection rates exceed the critical BHP parameters, the BBRS unit would be at risk for induced fracturing to occur and affect not only the target storage capacity, but potentially breach the caprock integrity too. The simulation results show that with an approximate 1.78 t/CO<sub>2</sub> per day for a year would only give a total of approximately 650 t/CO<sub>2</sub> per year, without exceeding the maximum allowable BHP. Given the injectivity rates of the BBRS unit, the reservoir will see approximately 3250 t/CO<sub>2</sub> over the five-year injection period. Though the injection rates for both the heterogeneous and layer cake models do appear to gradually increase over time and reach a plateau. This is caused by the CO<sub>2</sub> gas-water saturation effect or the relative permeability hysteresis, where the  $\kappa_{rCO_2}$  increases over time as a result of the decreasing water saturation (Bachu and Bennion, 2008). Initially, the simulation scenarios begin with a  $S_w$  of 1 and a CO<sub>2</sub> gas saturation ( $S_{gCO_2}$ ) of zero as injection has not commenced. Comparing initial injection periods to later periods of injection, the injection rates of CO<sub>2</sub> appear to increase. For example, from Figure 4-4 the initial injection rate begins at 1.25 t CO<sub>2</sub>/day and increases to approximately 2.75 t CO<sub>2</sub>/day over a two year period. The increased injectivity demonstrates this effect, where greater CO<sub>2</sub> saturations increase the  $\kappa_{rCO_2}$ . Another factor to consider is that gas compressibility is much greater than formation water. As well, the CO<sub>2</sub> gas is compositionally changing the system as it dissolves into the formation water. The simulated scenarios do not take into account further complexity of reservoir changes, such as chemical dissolution or precipitation of minerals within the rock. For all P10-50-90 cases, the injectivity remains steady after a

period of time, depicting greater CO<sub>2</sub> saturation levels in the BBRS unit. This plateau also represents the formation reaching the 90% of lithostatic pressure, as to not fracture the reservoir and maintain integrity for both the target and seal intervals. Following the plateau of increased injection rates per day, the simulated monthly CO<sub>2</sub> injections cease. A ten-year post-injection period is modeled to determine the saturation percentage of CO<sub>2</sub> in the target and seal intervals. Further results for the layer cake cases will not be discussed, and further simulation results reported focus on the 5 km by 5 km heterogeneous case.

Amongst the three P10-50-90 PHIE and K\_INT cases, there were no significant variations in the simulation results for the heterogeneous geodynamic model. The 3-D cross-sectional view of the plume distribution for one year into injection period for the P50 case appears to be asymmetrical, and is shown in Figure 4-5. The plume shape is mainly driven by the  $\kappa_v/\kappa_h$  ratio and buoyancy of the CO<sub>2</sub> gas. The injected CO<sub>2</sub> plume appears to be mainly contained within the BBRS unit, and extends approximately 50 m away from the 10-22 injector well. The CO<sub>2</sub> gas saturation remains the highest near the well at 0.45 and dissipates outwards to 0.30. Note that the  $S_{gCO_2}$  property is calculated to be unitless, and represents the volume of gas to the volume of pore void.

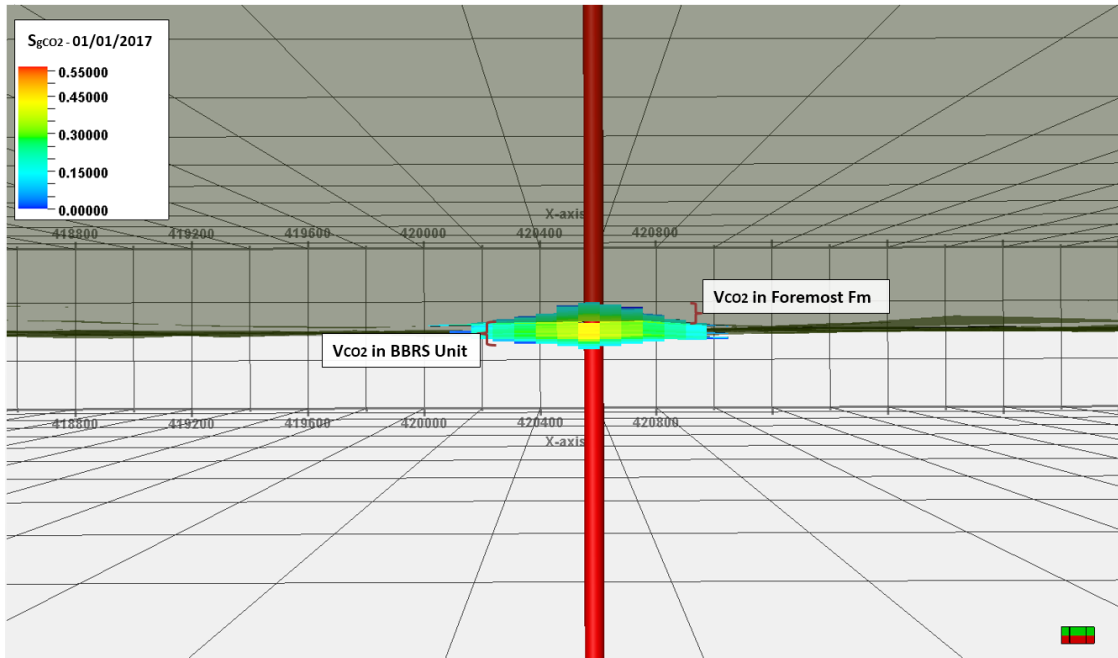


Figure 4-5. 3-D cross-section displaying the gas saturation and distribution of the injected CO<sub>2</sub> plume one-year into the injection period for the P50 case in the heterogeneous geodynamic model with V.E. of 1.

The 3-D plume distribution for five years into injection period for the P50 case is shown in Figure 4-6. The plume has a greater horizontal distribution, as it expands laterally within the BBRs unit. The injected CO<sub>2</sub> plume appears to still be mainly contained within the BBRs unit, with minor vertical migration of approximately 10 m into the Foremost Formation. The CO<sub>2</sub> gas saturation decreases radially away from the well, remaining the highest at 0.50 near the injector and decreases to 0.40 at approximately 50 m and down to 0.20 at 100 m from the well.

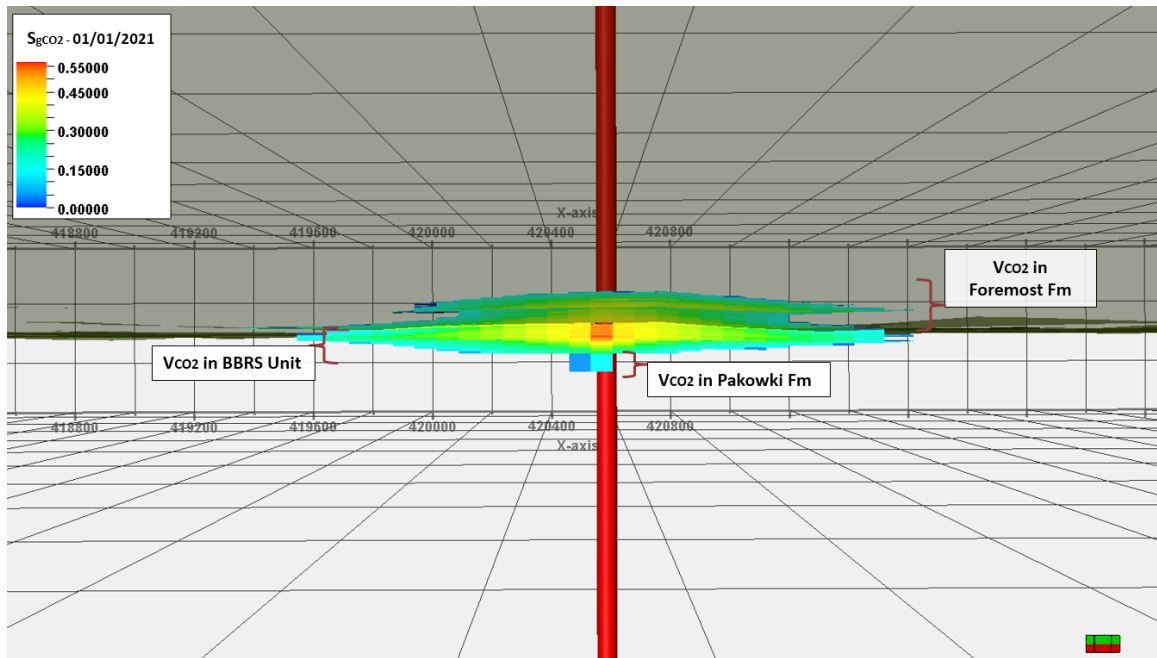


Figure 4-6. 3-D cross-section displaying the distribution of the injected CO<sub>2</sub> plume five years into the injection period for the P50 case in the heterogeneous dynamic model with V.E. of 1.

The 3-D plume distribution for the one-year post-injection period for the P50 case is shown in Figure 4-7. The plume is laterally extensive, as it has expanded and saturated the BBRs unit but also demonstrates a greater volume of CO<sub>2</sub> that has migrated vertically into the Foremost Formation. The top of the plume displays a flat appearance, which is interpreted to be caused by an impermeable coal zone. The coal zone disables further vertical migration, and causing the plume to spread laterally to account for the CO<sub>2</sub> volume. The vertical extent of the CO<sub>2</sub> plume that has moved into the Foremost Formation is estimated at 15 m. The plume edge remains extended at approximately 125 m away from the 10-22 injector well in the E-W direction. Similarly to the plume evolution during the injection period, the CO<sub>2</sub> gas saturation radially decreases away from the well. The highest CO<sub>2</sub> gas saturation at the 10-22 well is 0.50, and decreases to 0.40 at approximately 50 m, and decreases further to 0.20 at 100 m from the well.

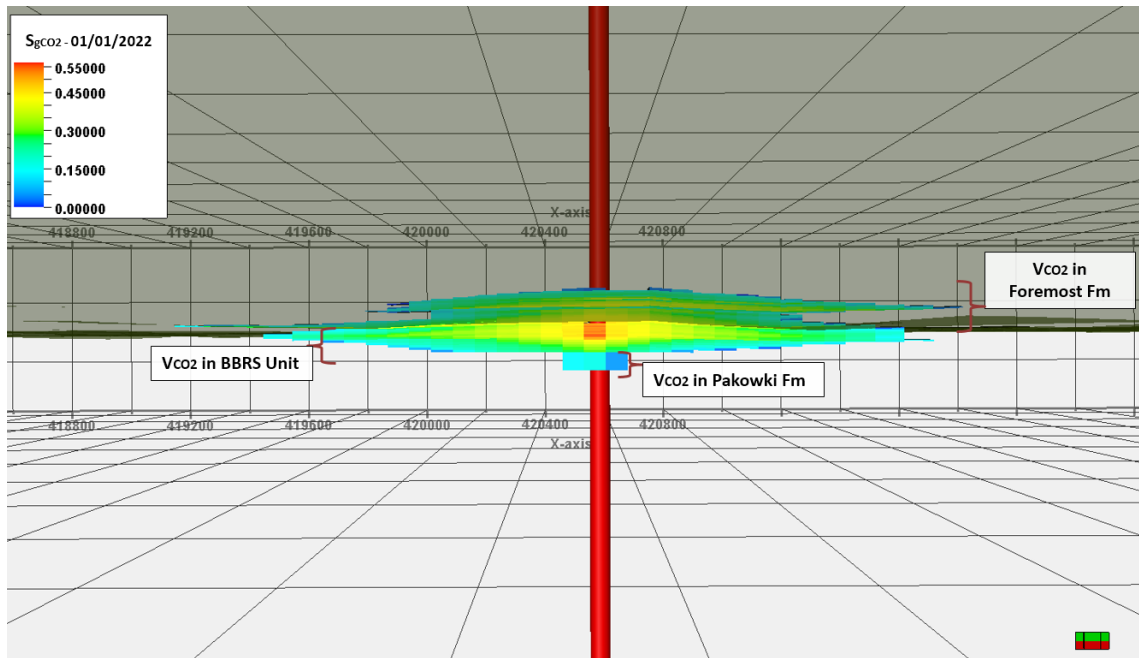


Figure 4-7. 3-D cross-section display of the distribution of the injected CO<sub>2</sub> plume 1 year post-injection for the P50 case in the heterogeneous geodynamic model with V.E. of 1.

The 3-D plume distribution for the ten-year post-injection period for the P50 case is shown in Figure 4-8. The plume has further extended laterally both in the BBRs unit and Foremost Formation, reaching approximately 175 m away from the 10-22 well. Building from the one-year post-injection simulation results, a greater volume of CO<sub>2</sub> has migrated vertically into the Foremost Formation reaching a total of 20 m from the top of the BBRs unit. The top of the plume continues to display a flat appearance, with minor coning as a result of buoyancy. Over ten-years, CO<sub>2</sub> gas saturation remains similar to the one-year post injection simulation results in that the highest CO<sub>2</sub> gas saturation occurs at the 10-22 injector well in the BBRs unit. The gas saturation decreases radially away from the well, where the highest CO<sub>2</sub> gas saturation is 0.50, decreasing to 0.40 at approximately 20 m, 0.35 to 0.30 at a distance of 80 m away, and down to 0.20 at over 100 m away from the injector well. The gas saturation behaves similarly in the vertical direction, where 0.50 remains at a distance of 10 m, dissipating to 0.20 over a shorter distance as a result of the low  $\kappa_v/\kappa_h$  ratio of 0.1. The low  $\kappa_v/\kappa_h$  ratio allows for greater expansion of the CO<sub>2</sub> in the horizontal direction with respect to the permeability property

K\_INT values. The low permeabilities of the coals, limited at 0.001 mD, reflect that the CO<sub>2</sub> plume is unable to grow vertically and thus vertically dissipates at a faster rate over a shorter given distance.

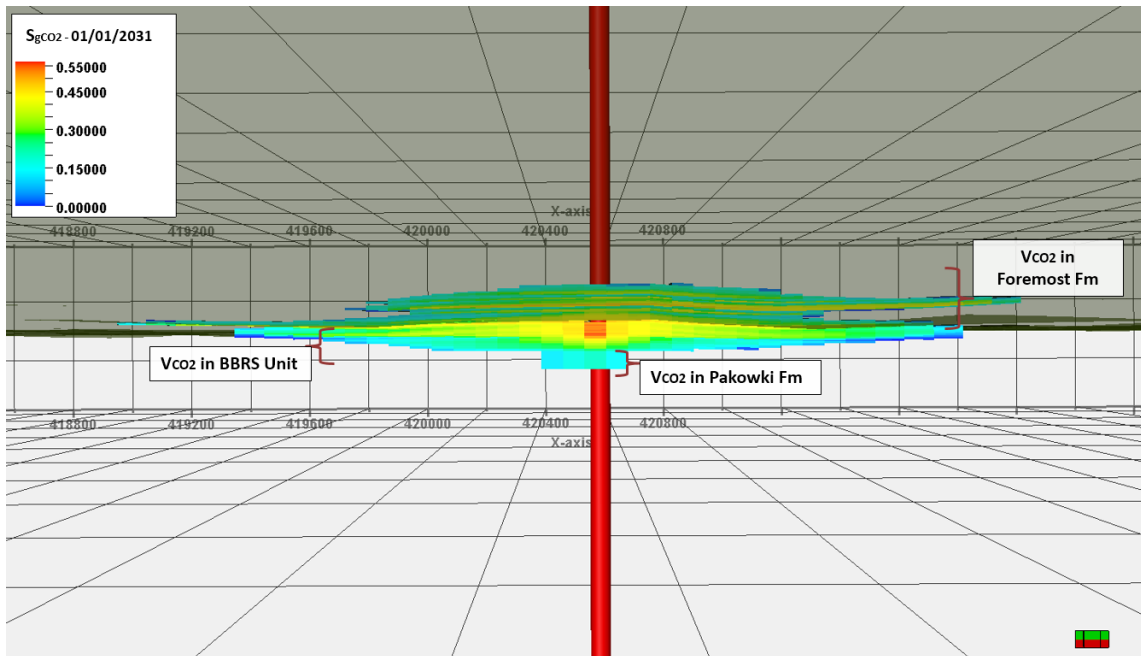


Figure 4-8. 3-D cross-section display of the distribution of the injected CO<sub>2</sub> plume 10 years post-injection for the P50 case in the heterogeneous geodynamic model with V.E. of 1.

The four cases described above can be more easily observed in 2-D (Figure 4-9). The CO<sub>2</sub> gas saturation profile is displayed in the E-W direction for the (A) one-year during injection, (B) five-years during injection, (C) one-year post-injection, and (D) ten-years post-injection periods.

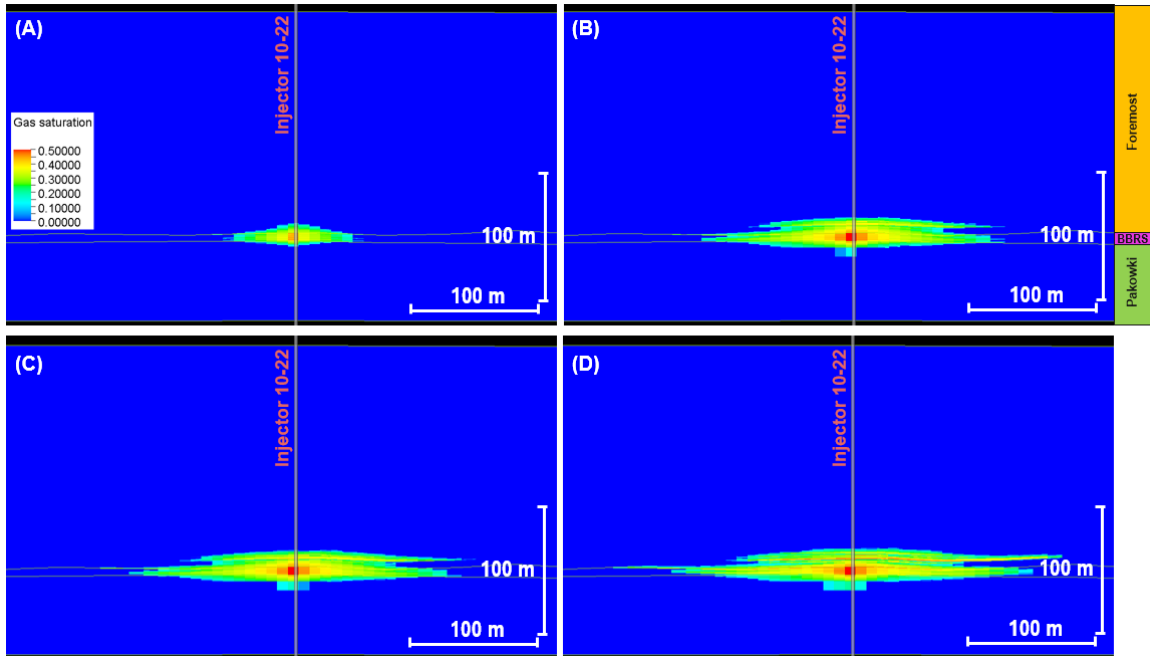


Figure 4-9. CO<sub>2</sub> saturation profile along the E-W direction for the P50 case of the heterogeneous geodynamic model. (A) After one-year during the injection period, (B) after five-years during the injection period, (C) one-year post-injection period, and (D) ten-years post-injection period. Figures taken and modified from Lee (2015).

The lateral and vertical extent of the CO<sub>2</sub> plume from the preliminary simulated scenarios does not show immediate concern for the plume rising above the base of groundwater protection at 301 m depth. The 5 km by 5 km heterogeneous geodynamic model including input from 88 wells was able to contain the CO<sub>2</sub> plume within 175 m from the 10-22 well. Looking at the plume distribution in plan view (Figure 4-10), the evolution consistently demonstrated a radially enlarged diamond-shaped plume. It is believed that the diamond-shape plume is an artefact of the tartan gridding used to upscale the static geomodel (Lee, 2015). To reduce this effect, further work has been completed on the layer cake cases to utilize constant cell sizing, but this is not explored within this thesis.

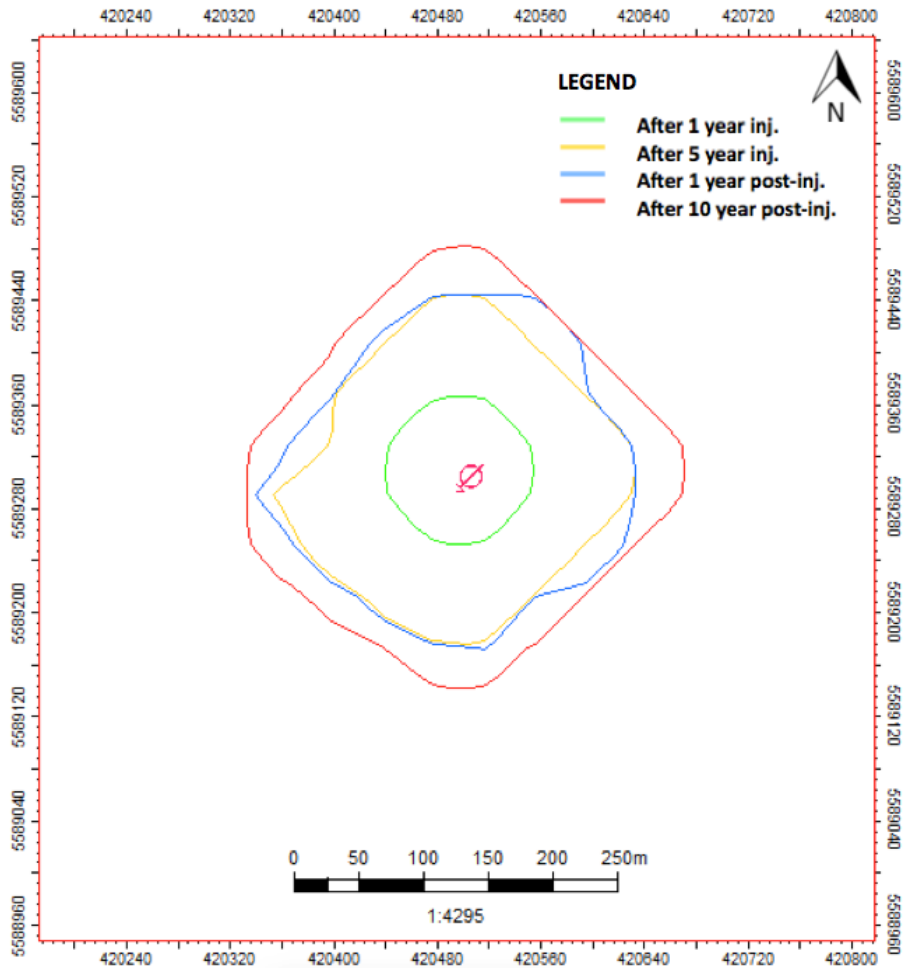


Figure 4-10. Plan view of the simulated scenarios for the P50 case of the heterogeneous geodynamic model, depicting the CO<sub>2</sub> plume edges. Figure taken and modified from Lee (2015).

The pressure plume as a result of the CO<sub>2</sub> injections is an important factor when considering both reservoir and caprock integrity, as well as remaining within the pressure threshold and maximum BHP to mitigate potential fracture/fault associated risks. Figure 4-11 shows the pressure plume build-up, as subtracting the dynamic model original pressure prior to injection and those after (A) one-year of injection, (B) five-years of injection, (C) one-year post-injection, (D) five-years post-injection, and (E) ten-years post-injection period.

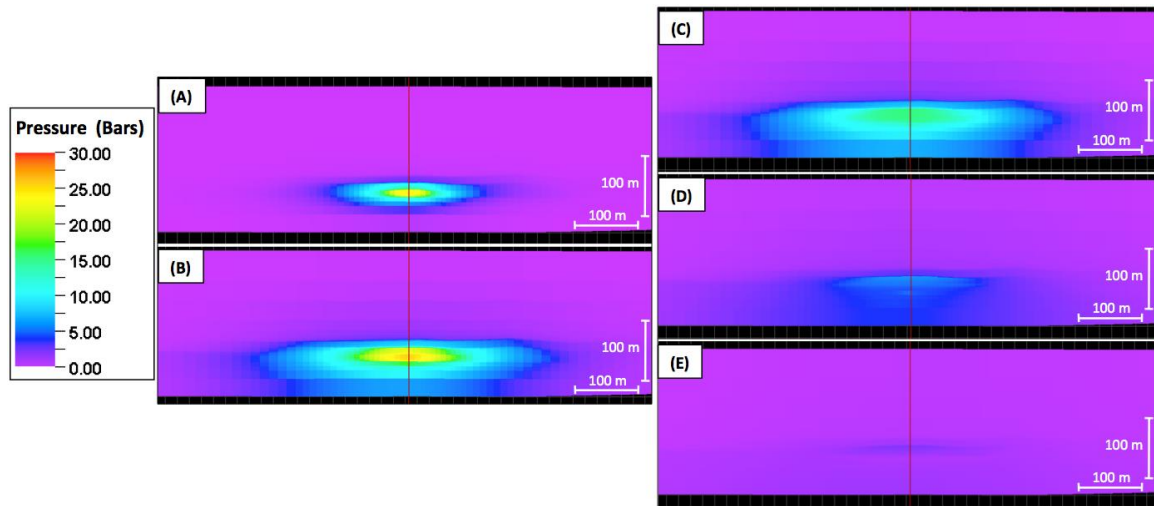


Figure 4-11. The pressure plume build-up sequence developed in the dynamic geomodel after (A) one-year of injection, (B) five-years of injection, (C) one-year post-injection, (D) five-years post-injection, and (E) ten-years post-injection period. The main injector well 10-22 is displayed in red running through each sub-figure. Note 1 bar = 0.1 MPa.

The maximum pressure build-up occurs after (B) five years of CO<sub>2</sub> injection, building up to pressures of 3.675 MPa and decreases radially out to 2.5 MPa, 1.0 MPa, and finally 0.5 MPa to 0 MPa. The 0 MPa does not represent no pressure is present, but that there is no calculated difference between the pressures prior to and after injection in this area. The pressure build-up quickly dissipates after (D) five years post-injection period. Note that below the BBRs injection zone in the geomodel, the pressure appears to be greater. Although the petrophysical properties, including the effective porosity and intrinsic permeability, are very similar throughout the model – the distance to the model edge boundary is much shorter to the bottom of the Pakowki Formation than to the top of the Foremost Formation. At ten years post-injection period (E), the pressure within the reservoir dissipates to approximately 0.5 MPa and should reach the static pressure environment prior to injection activity. The pressure data of the top and bottom seals, as well as within the reservoir, should be improved upon with knowledge of injectivity data and pressure testing at the injection well. With consideration of the maximum allowable BHP in the reservoir, the pressure differential plumes displayed over time demonstrate that the model simulates pressures much lower than 6.615 MPa. This is a good indicator

that the modified CO<sub>2</sub> injection plan and with the knowledge of the current petrophysical properties, the initial dynamic fluid flow simulations do not propose risks of breaching the caprock and reservoir integrity.

The dynamic simulation results of the geomodel illuminate containment of the total injection of approximately 3250 t of CO<sub>2</sub> over a five-year intermittent period. The P10-50-90 K\_INT and PHIE properties show only small changes in the plume distribution and injection rates between the three cases. The BBRS unit as the target interval appears to be an ideal reservoir with good porosity, but a target with greater permeability would allow for greater injectivity. The Foremost Formation as a seal is complex, with numerous interbedded zones varying from siltstone, shale, sandstones to coal. The coal zone that lays directly above the target interval, known as the McKay coal zone, appears to support the integrity of the seal interval. The low relative permeability and low effective porosity prove to hinder vertical migration of the CO<sub>2</sub> plume.

After one-year post-injection, the simulated plume is laterally extensive and expands to a total diameter of 250 m and expands 15 m above the BBRS unit. A CO<sub>2</sub> plume of this size should be able to be detected with basic MMV technologies, such as the downhole logging suite, pressure monitoring, chemical tracers, and 4-D reflection seismology. Further simulation scenarios will be tested on the layer cake models and analyzed, in order to account for the uncertainties that exist in both the geostatic and geodynamic models. Both models at the layer cake and heterogeneous scale will be improved with more field data measurements. These heterogeneous simulation results mark the preliminary commencement of moving towards obtaining an injection license, and have proved to be an educational experience.

## Chapter Five: **Discussion and Conclusions**

### **5.1 Discussion of uncertainties**

As a result of modeling in both the static and dynamic realm, the remaining uncertainties have been illuminated and place limitations on the confidence of target characterization and the fluid-flow simulation results. Within the static domain, uncertainties still exist within the quality of data used. This includes field acquisition parameters, tool calibration, precision of well bore trajectory, as well as editing logs to rid of erroneous spikes such as poor borehole contact or cycle skipping on the compressional sonic log tool. It is also important to note that interpretation on both well log data, core plug data, and seismic reflection volumes will differ from interpreter to interpreter. Although minor seismic attribute work was completed, further investigation is required to delineate intra-formational fractures or faults that may act as fluid pathways and promote leakage of the injected CO<sub>2</sub> gas. The identified depositional trend found from the spectral decomposition attribute could be used to guide the petrophysical model population with respect to the effective porosity and intrinsic permeability values for the BBRS unit.

Limited numerical data was available to quantify the permeability of the two coal zones within the Foremost Formation, attributing to uncertainty of how the two zones will behave if the CO<sub>2</sub> gas migrates vertically into them. The static geomodel aimed to characterize the coals with low relative intrinsic permeability, assuming high water saturation, methane content, and low permeability values found within the literature. But perhaps a greater understanding of the coal zones and the extent of the CO<sub>2</sub> plume if a range of intrinsic permeability values was modeled.

Lastly, one of the most important parameters that remains undefined is the ratio of vertical and horizontal permeability in both the target and seal A intervals. The core plug measurements and calculated well log data accounts for an isotropic, omni-directional intrinsic permeability in the static geomodel. Horizontal permeability can be measured through core plug measurements and pump tests across the FRS site, however it is the vertical permeability that encompasses the highest uncertainty. Vertical permeability is a

critical reservoir parameter, and is essential to understanding and quantifying the behaviour of the injected CO<sub>2</sub> volume. The geomodel populated the 3-D cells based on the calculated intrinsic permeability. However in the dynamic realm, a low vertical to horizontal intrinsic permeability ratio of 0.1 was used, assuming most lateral flow to occur along bedding planes. A range of vertical to horizontal intrinsic permeability ratios should be modeled to obtain a greater understanding of the best and worst case scenarios of the CO<sub>2</sub> plume, and what technologies would be best to include in the MMV plan for the FRS site.

Within the dynamic realm, uncertainties still exist in defining the fracture and capillary pressure of the target and seal A intervals. These two reservoir parameters effect the integrity of both intervals, injectivity of the reservoir, as well as the dominant trapping mechanism of which the injected CO<sub>2</sub> volume will adapt over time. The capillary and fracture pressures were estimated, however with acquiring more data from either formation pressure tests or core plug measurements could aid in quantifying or provide a range of pressures to then incorporate into modeling the fluid-flow simulations.

The CO<sub>2</sub>-water relative permeability was also estimated using a Brooks-Corey approximation for dynamic modeling. Although it is known that the relative permeability is greater with increasing concentration of a given phase, no quantifiable value was measured. This parameter effects both the total volume of CO<sub>2</sub> that can be injected into the target interval with respect to water saturation, as well as the saturation of CO<sub>2</sub> that can be reached and limits the confidence placed on the modeled scenarios.

Similarly, the injectivity of target A was unknown during the dynamic modeling process. Without knowing the injectivity, limitations and uncertainty is placed on the injection rates and injection pressures to use, which ultimately affects the estimation and confidence level in quantifying the total CO<sub>2</sub> volume to be injected over a five-year span.

The uncertainties that remain within the static and dynamic geomodels have been discussed and now revealed, where specific areas of improvement are required to better characterize the target and seal intervals of the geomodel. By modeling a range of reservoir parameters to give a best and worst case scenario of how the injected CO<sub>2</sub> plume will behave, this will contribute a greater understanding of the modeling process

instead of decisions being made based on one modeled scenario. This will provide a better understanding into not only the reservoir and caprock properties, but which MMV technologies could perform best for a range of scenarios to mitigate risks to maintain health and safety for the general public and surrounding environment.

## **5.2 Conclusions**

As part of the initialization phase of exploring potential reservoir targets for CO<sub>2</sub> injection, integration of geological, geophysical, and engineering data is critical for thorough characterization of a subsurface formation. As the main objective of this thesis, a 25 sq. km static geomodel geostatic was developed for the Field Research Station located in Newell County, SE Alberta. A summary of the completed work in part of the model construction, as well as preliminary petrophysical and fluid-flow simulation results are outlined below:

- Existing but limited wireline and 3-D seismic reflection data was used to interpret the subsurface horizons to a depth of 700 m. Subsurface horizons were interpreted on the wireline logs using mostly sonic, bulk density, gamma ray, and resistivity logs. Minor structural interpretation was completed using the geological information provided in the limited wireline log suite of the total 88 wells. Logs were edited to get rid of cycle skipping and erroneous spikes caused by poor borehole conditions.
- A regional and a localized 3-D seismic survey were used in geophysical interpretation, providing the major structural grid for the 3-D model. The SEG convention was used, where peaks and troughs were identified as an increase and decrease in acoustic impedance, respectively. Minor phase differences are present between the two seismic volumes, resulting in a mistie computation in two places of the seismic survey to reduce interpretation artefacts caused by the differences in horizon times.
- Both isopach and isochron maps were created using the difference of surface thicknesses computed between two sequential surfaces. The BBRs unit and

Foremost Formation demonstrated mean consistent thicknesses of 8 m and 167 m, respectively, throughout the study area.

- A primary and secondary target was outlined, however focus on further characterization was maintained on the primary target and seal known as the BBRS unit and Foremost Formation, respectively.
- Three wells (0-22, 7-22, and 7-21) were used for the well tie process. The lack of checkshot data required the TDR to be determined through a sonic calibration process. Minor stretch-squeeze adjustments resulted in erroneous interval velocities during the construction of the velocity model for volume depth conversion.
- Seismic depth conversion was based on the TDR developed through the well tie process with a simple velocity model, where interval velocities were computed based on the TDR from each well. The velocity modeling process utilizes the TDR from each well and the TWT at each subsurface horizon to pull the surfaces into the depth domain. Most interval velocities proved to be within range of velocities found in the literature for sandstone and shale formations. Some erroneous velocities were found in intervals at greater depths (600 m), much below the target interval of interest and thus were not reviewed further. The depth conversion proved to be effective, with well top interpretation based on the wireline data matching with the geophysical horizon interpretation both in time and depth.
- No channels or major fracturing or faulting was detected through extensive seismic attribute work completed both in the reservoir and seal intervals.
- The two main geological properties that were focused on to populate the 3-D model that were chosen include effective porosity and intrinsic permeability. A free-fluid approach was used in part of the petrophysical work to compute porosity, and was used in the Timur-Coates model to further compute intrinsic permeability.
- Log-to-core calibration was completed on the effective porosity and intrinsic permeability of all wells to ensure the six core data points with lab results were

honoured in the model volume. A 10:1 scalar factor was used to increase the calculated log of intrinsic permeability to match the lab measurements representative of the core in the BBRS unit.

- Statistical analyses were completed on the limited quantity of well data surrounding the study area. Variogram analyses were completed on the effective porosity and intrinsic permeability data to aid in guiding the model population. As a result of only having 88 wells, the variogram model proved to be difficult to model covariance between locations with data present. Under the assumption that the data was normally distributed, the sill was set to 1 with large major and minor ranges set to 1500 m, as the geological data appeared to remain consistent over the 1 km by 1 km region about the 10-22 well.
- The model population was completed using a Gaussian Random Function Simulation algorithm, where the input data is honoured with an element of randomness. When populating the intrinsic permeability volume, a correlation factor of 0.7 was used for kriging the data to the respective effective permeability model iteration.
- The BBRS unit yielded a mean porosity and intrinsic permeability of 11% and 0.57 mD, respectively. The permeability is relatively low and may limit the injectivity rate of CO<sub>2</sub> into the target reservoir.
- The Foremost Formation is a complex seal, containing numerous layers of interbedded shale, silty-sands, sand, and coal intervals. The coal seams directly overlying the target interval are continuous, with no apparent cleat systems and have low relative permeability due to the high water saturation and CH<sub>4</sub> concentrations in the pore spaces. These are suggested to be the first line of defence for preventing vertical migration of the injected CO<sub>2</sub> volume.
- To gain a better understanding of the uncertainty within the data, a P10-50-90 framework was used to characterize the conservative, typical, and optimistic ranges within the distribution of the effective porosity data in each target and seal interval. The attributed pore volume assigned to each percentile was used to calculate the respective intrinsic permeability cases. These three PHIE and K\_INT

model scenarios were further used in the fluid-flow simulation for the CO<sub>2</sub> injection.

- The static geomodel input was upscaled using a tartan gridding system to reduce the number of 3-D cells for the fluid-flow simulator. Model input parameters including maximum allowable BHP, salinity, rock compressibility, water saturation, and CO<sub>2</sub>-water relative permeability were calculated and used for the dynamic fluid-flow simulations.
- Dynamic simulation was completed on the P10-50-90 static cases for multiple injection scenarios, totalling approximately 650 t/CO<sub>2</sub>, per year for a five-year period. There were no significantly noted variations in the simulation results between the three static cases. The evolution of the CO<sub>2</sub> plume was observed at one-year during injection and five-years during injection, as well as the one-year and ten-year mark for the post-injection period. The final ten-year post-injection result simulated a laterally extensive plume, expanding to 350 m in diameter with 20 m of vertical migration above the BBRS unit for the P50 case.
- The maximum pressure plume differential simulated over the duration of the injection period demonstrates a 3.675 MPa pressure build-up. This build-up quickly dissipates over the ten-year post-injection period, and does not pose risk to breaching the maximum allowable BHP at 6.615 MPa.
- The thin target interval proves to be a great reservoir, and the seal interval demonstrates containment and conformance over a ten-year post-injection period.
- Static and dynamic uncertainties remain in estimating the reservoir pressure, fracture pressure, capillary pressure, as well as the gas-water relative permeability.
- This preliminary work of the geomodel and fluid-flow simulations will serve as a step towards obtaining the injection license as part of Directive 051 from the Alberta Energy Regulator.

### 5.3 Recommendations for future work

This thesis mainly focused on the construction of the regional geomodel consisting of two main petrophysical properties as the input for the fluid-flow simulations. Some recommendations to further characterize both the geological and geophysical input include:

- Thoroughly editing and completing further petrophysical analyses on all 88 wells in the project. This would have a great effect on the fluid characterization in the target interval, as well as the velocity modeling for depth conversion through the well tie process.
- Investigate the reservoir pressure regime and potential upward propagation effects of intra-formational fault and fracture systems potentially imposed by the Wabamun salt dissolution features below the Mannville Group.
- Perform further detailed analyses on intra-formational micro-fractures using FMI and core lab analyses to assess CO<sub>2</sub> plume flow predictions.
- Further define the uncertainties of the model both in a static and dynamic domain, where statistical analyses could quantify the model predictions.
- Complete further variography analyses on the data on all scales, including the wireline data, core data, and the two 3-D seismic volumes.
- Re-run the fluid-flow simulation scenarios with injectivity information input at the injector well 10-22, once injectivity tests have been run.
- Re-run the fluid-flow simulation scenarios with consideration of a non-open boundary condition to aid in visualizing the differences that occur with regards to the CO<sub>2</sub> plume edges and distribution.
- Compare and contrast the fluid-flow simulation results with the geomechanical simulations completed.
- Perform a seismic inversion to aid in visualizing the simulated CO<sub>2</sub> plume not only in a geological sense of pressure, but how the rock properties are changing and compare with the geomechanical simulation results.

## References

- Abaco, C. (2015). Personal Communication. Senior Geophysicist, Husky Energy, Calgary, Alberta, Canada.
- Abbas, M.Y. (2009). Incorporating seismic attribute variation into the pre-well placement workflow: A case study from Ness County, Kansas, USA (Master's Thesis). Department of Geology, College of Arts and Sciences, Kansas State University.
- Alberta Energy. (2013). Carbon Capture & Storage Summary Report of the Regulatory Framework Assessment. Electricity and Alternative Energy and Carbon Capture and Storage Division, Alberta Energy, pp. 86, 91, 92, 111.
- Allen, D., Bedford, J., Castelijns, K., Fairhurst, D., Gubelin, G., Heaton, N., Minh, C.C., Norville, M.A., Seim, M.R., Pritchard, T., and Ramamoorthy, R. (2000). Trends in NMR Logging. *Oilfield Review*, Autumn 2000. Retrieved from [https://www.slb.com/~media/Files/resources/oilfield\\_review/ors00/aut00/p2\\_19.pdf](https://www.slb.com/~media/Files/resources/oilfield_review/ors00/aut00/p2_19.pdf).
- Alshuhail, A. (2011). CO<sub>2</sub> Sequestration Site Characterization and Time-lapse Monitoring Using Reflection Seismic Methods. Doctoral Dissertation submitted to the Department of Geoscience, CREWES, University of Calgary, Calgary, Alberta, Canada.
- Anees, M. (2013). Seismic Attribute Analysis for Reservoir Characterization. KOCHI, 10<sup>th</sup> Biennial International Conference & Exposition, pp. 119. Retrieved from [http://www.spgindia.org/10\\_biennial\\_form/P119.pdf](http://www.spgindia.org/10_biennial_form/P119.pdf).
- Bachu, S. (2002). Sequestration of CO<sub>2</sub> in Geological Media Criteria and Approach for Site Selection in Response to Climate Change. *Energy Conversion and Management*, 43, pp. 87-102.
- Bachu, S. and Bennion, B. (2008). Effects of in-situ conditions on relative permeability characteristics of CO<sub>2</sub>-brine systems. *Environ Geol*, 54(8), pp. 1707-1722.
- Bacon, M., Simm, R., Redshaw, T. (2007). *3-D Seismic Interpretation*. Cambridge University Press.
- Barnes, A. (2006). Too many seismic attributes? *CSEG Recorder*, 31(3). Retrieved from <http://csegrecorder.com/articles/view/too-many-seismic-attributes>.
- Beaton, A. (2003). Coal-Bearing Formations and Coalbed-Methane Potential in the Alberta Plains and Foothills. Alberta Energy and Utilities Board/Alberta Geological Survey. *CSEG Recorder*, 28(9). Retrieved from

<http://csegrecorder.com/articles/view/coal-bearing-formations-and-coalbed-methane-potential-in-the-alberta-plains>.

- Beaton, A. (2003). Production Potential of Coalbed Methane Resources in Alberta. Alberta Energy and Utilities Board, EUB/AGS Earth Sciences Report 2003-03.
- Bentley, M. (2013). Modeling for Comfort. AGR TRACS Training. Capturing Uncertainty in Geomodels: Best Practices and Pitfalls. Abstract Book.
- Bond, C.E. (2013). Methods to Minimize and Capture Uncertainty during Model Creation. Capturing Uncertainty in Geomodels: Best Practices and Pitfalls. Abstract Book, December 11-12, 2013. Geology and Petroleum Geology, Kings College, University of Aberdeen, AB24 3UE.
- Bourbié, T. and Coussy, O. (1987). Chapter 5: Results and Mechanisms. Acoustics of Porous Media. Editions Technip. IPN: 9782710805168. Pp. 240. Retrieved from <https://books.google.ca/books?id=2ozNKWDUXU4C>.
- Brooks, R.H. and Corey, T. (1964). Hydraulic Properties of Porous Media. Colorado State University, *Hydrology Papers*, 3, pp. 1-24.
- Calvert, J.G. (2009). Glossary of atmospheric chemistry terms (Recommendations 1990). *Pure and Applied Chemistry (PAC)*, 62(11), 2167–2219. Retrieved from <http://goldbook.iupac.org/S06036.html>.
- CCP (CO<sub>2</sub> Capture Project). (2015). CO<sub>2</sub> Trapping Mechanisms. Retrieved from [http://www.co2captureproject.org/co2\\_trapping.html](http://www.co2captureproject.org/co2_trapping.html).
- CCSNetwork. (2012). Knowledge Sharing in MVA/MMV in CCS Demonstration Projects and Large Scale CO<sub>2</sub> Injection Tests: Workshop Summary. A report for the European CCS Demonstration Project Network. CCSNetwork.edu, Mobile, Alabama.
- CSLF (Carbon Sequestration Leadership Forum). (2013). 2013 Annual Report by the CSLF Task Force on Reviewing Best Practices and Standards for Geologic Storage and Monitoring of CO<sub>2</sub>. Initial Compilation of Standards, Best Practices and Guidelines for CO<sub>2</sub> Storage and Monitoring. Retrieved from [http://www.cslforum.org/publications/documents/ReviewingBestPracticesStandards\\_2013Report.pdf](http://www.cslforum.org/publications/documents/ReviewingBestPracticesStandards_2013Report.pdf).
- Chadwick, R.A., Arts, R., Bernstone, C., May, F., Thibeau, S., and Zweigel, P. (2008). Best practice for the storage of CO<sub>2</sub> in saline aquifers. British Geological Survey, NERC, Keyworth, Nottingham: British Geological Survey Occasional Publication No. 14. Retrieved from <http://core.ac.uk/download/pdf/63085.pdf>.

- Chopra, S. (2002). Coherence Cube and beyond. *First Break*, 20(1), pp. 27-33.
- Chopra, S. and Marfurt, K.J. (2007). Seismic Attributes for Prospect Identification and Reservoir Characterization. SEG Books, Issue 11 of Geophysical development series, ISBN 9781560801412. Retrieved from <https://books.google.ca/books?id=dP2iACuzq34C>. Pp. 208-210.
- Christopher, J., Yurkowski, M., Nicolas, M., and Bamburak, J. (2006). The Cenomanian-Santonian Colorado formations of eastern southern Saskatchewan and southwestern Manitoba; in Gilboy, C.F. and Whittaker, S.G. (eds.), Saskatchewan and Northern Plains Oil & Gas Symposium 2006, Saskatchewan Geological Society Special Publication 19, pp. 299-318. Retrieved from [http://www.gov.mb.ca/iem/petroleum/pubcat/Christopher\\_et\\_al.pdf](http://www.gov.mb.ca/iem/petroleum/pubcat/Christopher_et_al.pdf).
- Coates, G.R. and Dumanoir, J.L. (1974). A new approach to improved log-derived permeability. *The Log Analyst*, pp. 17.
- Cox, D.J., Cottam, M.A., Carruthers, R.A., Laws, E., and Nash, T. (2013). Capturing Stratigraphic and Depositional Framework Uncertainty in Inter-Well Areas: An Example from the Magnus Field, Northern North Sea, UK. Capturing Uncertainty in Geomodels: Best Practices and Pitfalls. Abstract Book, December 11-12, 2013. BP Exploration Operating Company Limited, 1-4 Wellheads Avenue, Dyce, Aberdeen, AB21 7PB.
- Cummings, S., Enick, R., Rogers, S., Heenan, R., and Eastoe, J. (2012). Amphiphiles for supercritical CO<sub>2</sub>. *Biochimie*, 94(10), pp. 94-100.
- Hansell, D.A. and Carlson, C.A. (2013). Localized refractory dissolved organic carbon sinks in the deep ocean. *Global Biogeochemical Cycles*, 27(3), pp. 705-710. DOI: 10.1002/gbc.20067
- Environment Canada. (2015). Global Greenhouse Gas Emissions. Environmental Indicators, Air and Climate Indicators. Government of Alberta. Retrieved from <http://www.ec.gc.ca/indicateurs-indicators/default.asp?lang=en&n=54C061B5-1>.
- Environment Canada. (2015). Drivers and Impacts of Greenhouse Gas Emissions. Environmental Indicators, Air and Climate Indicators. Government of Alberta. Retrieved from <http://www.ec.gc.ca/indicateurs-indicators/default.asp?lang=En&n=D4C4DBAB-1>.
- Etris, E.L., Crabtree, N.J., and Dewar, J. (2002). True Depth Conversion: More Than a Pretty Picture. *CSEG Recorder*, 26(9). Retrieved from <http://csegrecorder.com/articles/view/true-depth-conversion-more-than-a-pretty-picture>.

- Fichtl, P., Hirst, P., and Kaesbach, I. (2013). From subsurface uncertainty assessment to risk management: How to make best use of our static reservoir models. *Capturing Uncertainty in Geomodels: Best Practices and Pitfalls*. Abstract Book, December 11-12, 2013. BP Exploration Operating Company Limited, Chertsey Road, Sunbury-on-Thames, TW16 7LN.
- Gardiner, S., Thomas, D.V., Bowering, E.D., and McMinn, L.S. (1990). A Braided Fluvial Reservoir, Peco Field, Alberta, Canada. *Casebooks in Earth Science Sandstone Petroleum Reservoirs*, New York, New York: Springer-Verlag New York Inc, pp. 45-46.
- Geertsma, J. (1957). The effect of fluid pressure decline on volumetric changes of porous rock. Society of Petroleum Engineers, published in *Petroleum Transactions, AIME, 210*, pp. 331-340.
- Goodarzi, S. (2015). Personal Communication. Reservoir-Geomechanics Engineer, Taurus Reservoir Solutions Ltd., 1015-4<sup>th</sup> Street SW, Calgary, Alberta, Canada T2R 1J4.
- Google Maps. (2016). Accessed January 2016 online from © Google Maps 2016.
- Goovaerts, P. (1997). *Geostatistics for Natural Resource Evaluation*. Oxford University Press, New York, pp. 369-376.
- Gordon, J. (2000). Stratigraphy and Sedimentology of the Foremost Formation in Southeastern Alberta and Southwestern Saskatchewan. Master's Thesis of Applied Sciences, University of Regina, Saskatchewan.
- Gubelin, G. and Boyd, A. (1997). Total Porosity and Bound-Fluid Measurements from an NMR Tool. *Journal of Petroleum Technology, 49(7)*, pp.718.
- Hall, M. and Trouillot, E. (2004). Predicting stratigraphy with spectral decomposition. 2004 CSEG National Convention. Retrieved from [http://cseg.ca/assets/files/resources/abstracts/2004/046S0131-Hall\\_M\\_Trouillot\\_Modelling\\_Spectral\\_Decomposition.pdf](http://cseg.ca/assets/files/resources/abstracts/2004/046S0131-Hall_M_Trouillot_Modelling_Spectral_Decomposition.pdf).
- Hamblin, A.P. and Abrahamson, B. (1993). Offlapping progradational cycles and gas pool distribution in the Upper Cretaceous "Basal Belly River" sandstones, Judith River Group, Southern and Central Alberta. Geological Survey of Canada, Natural Resources Canada, Open File 2672, pp. 10.
- Hamblin, A.P. and Abrahamson, B.W. (1996). Stratigraphic architecture of "Basal Belly River" cycles, Foremost Formation, Belly River Group, subsurface of southern Alberta and southwestern Saskatchewan. *Bulletin of Canadian Petroleum Geology, 44(4)*, pp. 654-673.

- Hamblin, A.P. (1997). Regional Distribution and Dispersal of the Dinosaur Park Formation, Belly River Group, Surface and Subsurface of Southern Alberta. *Bulletin of Canadian Petroleum Geology*, 45(3), pp. 377-399.
- Hamblin, A.P. and Lee, P.J. (1995). Assessment of Upper Cretaceous-Tertiary gas resources, post-Colorado strata, WCSB, Interior Plains. Geological Survey of Canada, Open File 2058, pp. 335-336.
- Hamblin, A.P. and Lee, P.J. (1997). Upper Cretaceous, post-Colorado gas resources of the Western Canada Sedimentary Basin, Interior Plains. Geological Survey of Canada, Bulletin 518, pp. 88.
- Herron, M.M. (1987). Estimating the Intrinsic Permeability of Clastic Sediments from Geochemical Data. Society of Petrophysicists and Well-Log Analysts, Twenty-Eighth Annual Logging Symposium. pp. 1-23.
- Höcker, C. (2013). Structural uncertainty – Real or caused by flaws in analysis and modeling? Capturing Independent geoscience advisor, consulting with Nexen Petroleum U.K. and Baker Hughes. Uncertainty in Geomodels: Best Practices and Pitfalls. Abstract Book, December 11-12, 2013.
- Hovorka, S.D., Choi, J.-W., Meckel, T.A, Trevino, R.H., Zeng, H., Kordi, M., Wang, F.P. (2008): Comparing carbon sequestration in an oil reservoir to sequestration in a brine formation- field study: presented at the 9th International Conference on Greenhouse Gas Control Technologies (GHGT-9), Washington, D.C., November 16-20, 2008. GCCC Digital Publication #08-03 D.
- IPCC. (2005). IPCC Special Report on Carbon Dioxide Capture and Storage. Prepared by Working Group III of the Intergovernmental Panel on Climate Change. (B. Metz, O. Davidson, H. de Coninck, M. Loos, & L. Meyer, Eds.) Cambridge, United Kingdom and New York, NY, USA: Cambridge University Press.
- Karner, S.L. (2005). Stimulation techniques used in enhanced geothermal systems: Perspectives from geomechanics and rock physics. Stanford Geothermal Workshop, HDR/EGS Session, Stanford University, Stanford, California, SGP-TR-176. Retrieved from <http://www.geothermal-energy.org/pdf/IGAstandard/SGW/2005/karner.pdf>.
- La Croix, A.D., Gingras, M.K., Pemberton, S.G., Mendoza, C.A., MacEachern, J.A., and Lemiski, R.T. (2013). Biogenically enhanced reservoir properties in the Medicine Hat gas field, Alberta, Canada. *Marine and Petroleum Geology*, 43, pp. 464-477.
- Lawton, D.C. (2013). Geoscience Field Research Station Proposal Summary. CMC Research Institutes, University of Calgary, Calgary, Alberta, Canada.

- Lawton, D.C., Adamson, R., and Osadetz, K. (2014). CMC Research Institutes: Containment and Monitoring Institute (CaMI) [PowerPoint slides]. Retrieved from Dr. D.C. Lawton.
- Leckie, D.A., Bhattacharya, J.P., Bloch, J., Gilboy, C.F., and Norris, B. (1994). Chapter 20 – Cretaceous Colorado / Alberta Group of the Western Canada Sedimentary Basin. Alberta Geological Survey. Obtained online on April 15, 2014 from [http://www.ag.gov.ab.ca/publications/SPE/PDF/SPE\\_004/low\\_res/chapter\\_20.pdf](http://www.ag.gov.ab.ca/publications/SPE/PDF/SPE_004/low_res/chapter_20.pdf).
- Leckie, D.A. and Smith, D.G. (1992). Regional Setting, Evolution, and Depositional Cycles of the Western Canada Foreland Basin: Chapter 1. AAPG Special Volume 55: Foreland Basins and Fold Belts, pp. 9-46.
- Lee, S.Y. (2014-15). Personal Communication. Principal Reservoir Engineer, Carbon Services. Schlumberger Canada Limited, 200 125-9<sup>th</sup> Avenue SE, Calgary, Alberta, T2G0P6.
- Li, K. and Horne, R.N. (2006). Comparison of methods to calculate relative permeability from capillary pressure in consolidated water-wet porous media. American Geophysical Union, *Water Resources Research*, 42, W06405, DOI: 10.1029/2005WR004482.
- Li, H., Jakobsen, J.P., Wilhelmsen, O., and Yan, J. (2011). PVT<sub>xy</sub> properties of CO<sub>2</sub> mixtures relevant for CO<sub>2</sub> capture, transport, and storage: Review of available experimental data and theoretical models. *Applied Energy*, 88, pp. 3567-3579
- Luthi, S.M. (2013). Geological Well Logs: Their use in reservoir modeling. Springer Science & Business Media, pp. 178.
- Mao-Jones, J. (2012). Decision & Risk Analysis. The Merrick Consultancy. Retrieved from <http://www.merrick.com/merrickandcompany/media/Resources/Energy/Whitepapers/Merrick-Decision-Risk-Analysis-White-Paper.pdf?ext=.pdf>.
- Marfurt, K.J., Kirilin, R.L., Farmer, S.L., and Bahorich, M.S. (1998). 3-D seismic attributes using a semblance-based coherency algorithm. *Geophysics*, 63(4), pp. 1150-1165.
- McNeil, D.H. and Caldwell, W.G.E. (1981). Cretaceous Rocks and their foraminifera in the Manitoba Escarpment. Geological Association of Canada, Special Paper 21, pp. 439.

- McPherson, B.J. (2012). CO<sub>2</sub> Trapping Mechanisms. University of Utah, CVEEN 7920 – Carbon Capture and Storage. Retrieved from [http://training.swpartnership.org/CCSclass/CCS\\_Module\\_files/CO2trapping\\_mechanisms\\_2012.pdf](http://training.swpartnership.org/CCSclass/CCS_Module_files/CO2trapping_mechanisms_2012.pdf).
- Meunier, R., Chautru, J.M., Jeannée, N. (2013). Model-derived uncertainties or uncertainty about models? Geovariations, France. Capturing Uncertainty in Geomodels: Best Practices and Pitfalls. Abstract Book, December 11-12, 2013.
- Meurant, G. (2011). Belly River Pool, Pembina Oil Field, Alberta. Geomorphology of oil and gas fields in sandstone bodies. Developments in Petroleum Science 4. Amsterdam, The Netherlands: Elsevier Scientific Publishing Company, pp. 129-131.
- Munõz, A. and Hale, D. (2012). Automatically tying well logs to seismic data. Center for Wave Phenomena Report #725, Colorado School of Mines, Golden, Colorado. Retrieved from <http://www.cwp.mines.edu/Documents/cwpreports/CWP725.pdf>.
- NRCAN (Natural Resources of Canada). (2014). Lithological Units: Bearpaw Formation. Retrieved from <http://weblex.nrcan.gc.ca/html/000000/GSCC00053000966.html>.
- NRCAN (Natural Resources of Canada). (2014). Lithological Units: Foremost Formation. Retrieved from <http://weblex.nrcan.gc.ca/html/005000/GSCC00053005119.html>.
- NRCAN (Natural Resources of Canada). (2014). Lithological Units: Oldman Formation. Retrieved from <http://weblex.nrcan.gc.ca/html/011000/GSCC00053011229.html>.
- Nauriyal, A.K., Sarkar, A.K., and Kamat, V.V. (2010). Identification of discontinuities by attribute analysis and planning of wells for basement exploitation – A case study in Mumbai High Field. 8<sup>th</sup> Biennial International Conference & Exposition on Petroleum Geophysics, HYPERABAD 2010, pp. 258. Retrieved from <http://www.spgindia.org/2010/258.pdf>.
- Nelson, C.R., Evans, J.M., Sorensen, J.A., Steadman, E.N., and Harju, J.A. (2005). Factors affecting the potential for CO<sub>2</sub> leakage from geologic sinks. Plains CO<sub>2</sub> Reduction (PCOR) Partnership, Energy and Environmental Research Center. Retrieved from <http://www.undeerc.org/pcor/newsandpubs/pdf/FactorsAffectingPotential.pdf>.
- Newmark, R.L., Friendmann, S.J., and Carroll, S.A. (2010). Water Challenges for Geologic Carbon Capture and Sequestration. *Environmental Management*, 45(4), pp. 651-661.

- Nielsen, K.S. and Schröder-Adams, C.J. (1999). Upper Colorado Group lithology and wire line log correlation in southwestern Saskatchewan. In Summary of Investigations 1998, Saskatchewan Geological Survey, Saskatchewan Energy Mines, miscellaneous Report 98-4, pp. 79-84.
- Nielsen, K.S., Schröder-Adams, C.J., and Leckie, D.A. (2003). A new stratigraphic framework for the Upper Colorado Group (Cretaceous) in southern Alberta and southwestern Saskatchewan, Canada. *Bulletin of Canadian Petroleum Geology*, 51(3), pp. 204-246.
- Nielsen, K.S., Schröder-Adams, C.J., Leckie, D.A., Haggart, J.W., and Elberdak, K. (2008). Turonian to Santonian paleoenvironmental changes in the Cretaceous Western Interior Sea: The Carlile and Niobrara formations in Southern Alberta and Southwestern Saskatchewan, Canada. *Palaeogeography, Palaeoclimatology, Palaeoecology*, 270, pp. 64-91.
- Nolen-Hoeksema, R. (2014). Flow Through Pores. *Oilfield Review* 2014, 26(3). Retrieved from [http://www.slb.com/news/inside\\_news/2015/~/\\_media/Files/resources/oilfield\\_review/ors14/aut14/define\\_perm.ashx](http://www.slb.com/news/inside_news/2015/~/_media/Files/resources/oilfield_review/ors14/aut14/define_perm.ashx).
- Oliver, M.A. and Webster, R. (2015). Basic Steps in Geostatistics: The Variogram and Kriging. Springer International Publishing, ed. 1, SpringerBriefs in Agriculture, DOI: 10.1007/978-3-319-15865-5.
- PNNL (Pacific Northwest National Laboratory). (2015). Kriging Variogram. U.S. Department of Energy. Retrieved from [http://vsp.pnnl.gov/help/Vsample/Kriging\\_Variogram.htm](http://vsp.pnnl.gov/help/Vsample/Kriging_Variogram.htm).
- Pedersen, P.K. (2013-16). Personal Communication. Associate Professor, Department of Geoscience. University of Calgary, 2500 University Dr. NW, Calgary, Alberta, T2N 1N4.
- Pohl, W.L. (2011). Chapter 7: Petroleum and Natural Gas Deposits. *Economic Geology: Principles and Practice*. West Sussex, UK: John Wiley and Sons Ltd., pp. 561.
- Rider, M. and Kennedy, M. (2011). *The Geological Interpretation of Well Logs*. 3<sup>rd</sup> Edition, published by Rider-French Consulting Ltd., pp.132.
- Robinson, C.C. (2008). A multidisciplinary approach to evaluating shale gas potential in a biogenic gas system; the upper Colorado Group shales in southeastern Alberta. Master's Thesis, University of Calgary, Calgary, Alberta, Canada.
- Rushing, J.A., Newsham, K.E., Lasswell, P.M., Cox, J.C., and Blasingame, T.A. (2004). Klinkenberg-Corrected Permeability Measurements in Tight Gas Sands: Steady-

- State Versus Unsteady-State Techniques. Society of Petroleum Engineers Inc, paper #89867, pp. 1-11.
- Russell, L.S. and Landes, R.W. (1940). Geology of the southern Alberta Plains. Geological Survey of Canada, Memoir 221, pp. 223.
- Sbar, M. (2014). An interview with Marc Sbar: Pre-stack is the way to go. CSEG Recorder, 39(2). Retrieved from <http://csegrecorder.com/interviews/view/interview-with-marc-sbar>.
- Schröder-Adams, C.J., Adams, P.J., Leckie, D.A., Bloch, J., Craig, J., and Seif El-Dein A.S. (1997). Upper Cretaceous Medicine Hat Formation and First White Speckled Shale in southeastern Alberta: evidence for localized shallow water deposition. *Bulletin of Canadian Petroleum Geology*, 45(3), pp. 356-376
- Schlumberger Ltd. (2015). Petrel E&P Platform Help File. License used in the Department of Geosciences, University of Calgary, 844 Campus Place NW, Calgary, Alberta, T2N 1N4.
- Schlumberger Reservoir Laboratories Canada. (2015). Final Core Analysis Report. Prepared for CMC Research Institutes, Inc for Countess 10-22-17-16W4, License: AB0474436, SRL Project Number: 20150033, August 2015.
- Shetsen, I. (1987). Quaternary Geology, Southern Alberta. Alberta Research Council. Map 207.
- Shouldice, J.R. (1979). Nature and potential of Belly River gas sand traps and reservoirs in western Canada. *Bulletin of Canadian Petroleum Geology*, 27, pp. 229-241.
- Skinner, G. (2013). Wellbore position uncertainty: a primer for Geomodellers. Baker Hughes. Capturing Uncertainty in Geomodels: Best Practices and Pitfalls. Abstract Book, December 11-12, 2013.
- Skorstad, A. and Leahy, G. (2013). Propagating Uncertainties through Disciplines – Avoiding Local Optimizations on Wrong Assumptions. Roxar Software Solutions. Capturing Uncertainty in Geomodels: Best Practices and Pitfalls. Abstract Book, December 11-12, 2013.
- Stunell, M. (2013). Integration Matters – The challenge of adopting technology for effective subsurface uncertainty assessments. Reservoir Engineering Technical Consultant, Schlumberger Information Solutions. Capturing Uncertainty in Geomodels: Best Practices and Pitfalls. Abstract Book, December 11-12, 2013.

- Subrahmanyam, D. and Rao, P.H. (2008). Seismic Attributes – A review. 7<sup>th</sup> International Conference & Exposition on Petroleum Geophysics, HYDERABAD 2008. Retrieved from <http://www.spgindia.org/2008/398.pdf>.
- Swager, L. (2014-5). Personal Communication. Senior Petrophysicist, Carbon Services. Schlumberger Limited, 1875 Lawrence St Ste 500, Denver, CO 80202.
- Tanikawa, W. and Shimamoto, T. (2006). Klinkenberg effect for gas permeability and its comparison to water permeability for porous sedimentary rocks. *Hydrology and Earth System Sciences Discussions*, 3, pp. 1315-1338. Retrieved from <http://www.hydrol-earth-syst-sci-discuss.net/3/1315/2006/hessd-3-1315-2006-print.pdf>.
- Taylor, S.E. (2011). Shale Gas Potential of the Late Cretaceous Upper Colorado Group; Bigstick Pool, Southeastern Alberta and Southwestern Saskatchewan. Doctoral dissertation submitted to the Department of Geoscience, University of Calgary, Calgary, Alberta, Canada.
- Thomas, L. (2002). Coal Geology. John Wiley & Sons. Retrieved from [http://books.google.ca/books?id=4oYWx90ybY8C&printsec=frontcover&source=gbs\\_ge\\_summary\\_r&cad=0#v=onepage&q&f=false](http://books.google.ca/books?id=4oYWx90ybY8C&printsec=frontcover&source=gbs_ge_summary_r&cad=0#v=onepage&q&f=false).
- Timur, A. (1968). An investigation of permeability, porosity, and residual water saturation relationship for sandstone reservoirs. *The Log Analyst*, 9(4), pp. 8.
- Trautz, R.C., Pugh, J.D., Varadharajan, C., Zheng, L., Bianchi, M., Nico, P.S., Spycher, N.F., Newell, D.L., Esposito, R.A., Wu, Y., Dafflon, B., Hubbard, S.S., and Birkholzer, J.T. (2012). Effect of Dissolved CO<sub>2</sub> on a Shallow Groundwater System: A Controlled Release Field Experiment. American Chemical Society. *Environmental Science and Technology*, 47, pp. 298-305.
- Ugborugbo, O. and Rao, T. (2009). Impact of Borehole Washout on Acoustic Logs and Well-to-Seismic Ties. Society of Petroleum Engineers Inc. DOI: 10.2118/128346-MS
- Webb, A.C., Schröder-Adams, C.J., and Pedersen, P.K. (2005). Regional subsurface correlation of Albian sequences north of the Peace River in NE British Columbia: northward extent of sandstones of the Falher and Notikewin members along the eastern flank of the foredeep. *Bulletin of Canadian Petroleum Geology*, 53, pp. 165-188.
- Worley Parsons Komex. (2008). Regional Groundwater Resource Assessment for the County of Newell No. 4. Resources and Energy, Environment & Water Resources. County of Newell and AAFC-PFRA, pp. 1-105.

Zaluski, W. (2013-15). Personal Communication. Senior Geologist, Carbon Services. Schlumberger Canada Limited, 200 125-9<sup>th</sup> Avenue SE, Calgary, Alberta, T2G0P6.

Zaluski, W. and Lee, S.Y. (2015). Personal Communication. Schlumberger Ltd., Carbon Services.

Zhang, D. and Song, J. (2014). Mechanisms for geological carbon sequestration. Mechanics for the World: Proceedings of the 23<sup>rd</sup> International Congress of Theoretical and Applied Mechanics, ICTAM2012. *Procedia IUTAM*, 10, pp. 319-327.